S. M. THESIS

SEPT. 1986

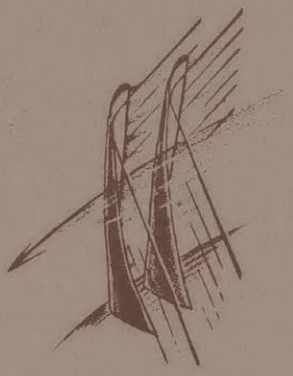

GAS TURBINE LABORATORY
MASSACHUSETTS INSTITUTE OF TECHNOLOGY
CAMBRIDGE, MASSACHUSETTS

COMPUTATIONAL SIMULATION OF UNSTEADY FLOW IN A TRANSONIC COMPRESSOR ROTOR

by

Philip Ray Owen

GTL Report No. 189 October 1986

This work was sponsored by the Allison Gas Turbine Division of General Motors, and by the Air Force Office of Scientific Research, Multi-Investigator Contract #F49620-85-C-0018, Dr. James D. Wilson Program Manager.

COMPUTATIONAL SIMULATION OF UNSTEADY FLOW

IN A TRANSONIC COMPRESSOR ROTOR

by

PHILIP RAY OWEN

ABSTRACT

The unsteady flow about a section of a modern first stage transonic compressor rotor was simulated using a finite difference approximation to the two-dimensional, Reynolds averaged, unsteady, compressible, viscous Navier-Stokes equations. The computation was performed in both steady state and time-accurate modes, and the results compared. The time-accurate results were analyzed in some detail.

Two frequency regimes were observed. High frequency unsteadiness due to vortex shedding was found at frequencies varying between 11 KHz and 19 KHz. A low frequency cycle was also observed at 365 Hz. The low frequency cycle produced significant variations in blade force and moment. It also modulated the strength and frequency of the vortex shedding.

Arguments were advanced to explain the mechanics of the vortex street formation in terms of a single free shear layer instability. The variations in shedding strength and frequency were related to movement of the separation point. A wholly satisfactory normalization of the frequencies was not found.

The low frequency cycle was analyzed as a quasi-steady sequence of events stemming from movement of a shock wave spanning the blade passage. The possibility was entertained that the cycle was due to purely numerical sources, but no likely mechanism was found.

TABLE OF CONTENTS

LIST OF TABLES

LIST OF FIGURES

Chapter 6

Chapter 7

CHAPTER 1 INTRODUCTION

The flow through the compressor stage of a gas turbine engine is inherently unsteady in the laboratory frame of reference. For the purpose of designing and analyzing these machines, it is traditional (and a tremendous simplification) to assume that the unsteadiness is purely due to the rotation of the compressor rotor, i.e. that the flow relative to the compressor blades themselves is steady. It has become apparent, however, that even in the blade-relative frame there is considerable unsteadiness in the flow. This has been documented especially by Ng in [1.1] and [1.2], and by Gertz in [1.3] by use of high frequency response instrumentation. As the nature of this unsteadiness becomes better understood, it is expected that the time-averaged performance and reliability of gas turbine compressors may potentially be improved by accounting in the design process for the unsteadiness.

The measurements taken to date, however, have given only a limited view of the actual blade-relative flow field. Indeed, it is impossible to fully construct many flow details from information sampled at a single location (or small number of locations) behind a rotating compressor rotor. Ng hypothesized a high frequency vibration of the rotor shock wave as a cause of much of the unsteadiness he observed. Gertz hypothesized the presence of a vortex street in the blade wakes and constructed a model of such a flow which agrees qualitatively (and in several quantitative respects) with his data. Additional information about the validity of these hypotheses and about other flow details is needed in order for a better understanding of blade-relative unsteadiness to be gained and effectively used.

It is hoped that experimental techniques will be developed to allow the

direct measurement of additional unsteady flow phenomena in the turbomachinery environment. For the present, however, resort has been made to computational simulation of the flow fields in question. Time-accurate computational results have been published by Scott in [1.4] and by Scott and Hankey in [1.5]. These efforts have focused on the effects of upstream unsteadiness such as are created by the wakes of stationary guide vanes entering the rotor flow field. The results obtained by Ng and Gertz, however, show blade-relative unsteadiness behind fan rotors the flow upstream of which is steady. The interest in blade-relative unsteadiness for cases in which the upstream flow is steady has led to the present study.

The objective of this work is to numerically simulate the two-dimensional unsteady blade-relative flow field of a modern transonic compressor fan rotor and examine in some detail the nature of the unsteadiness observed. Chapter 2 surveys the computational algorithm used and the general method of investigation. Chapter 3 discusses details relating to the specific case studied. Chapter 4 presents the steady state results for this case. Chapter 5 is an overview of the unsteady results obtained which introduces the two frequency regimes observed. Chapters 6 and 7 discuss in more detail the high and low frequency cycles respectively. The final chapter summarizes the conclusions drawn from this work together with some suggestions for further study.

CHAPTER 2 METHOD AND COMPUTATIONAL PROGRAM

2.1 Computational Method

Chapters 4 and following present results and analysis of results from a numerical simulation of a compressor flowfield. The program used for this simulation is called ANSI2D. It is a discrete iterative approximation to the Reynolds averaged, unsteady, compressible, viscous Navier-Stokes equations in two-dimensions. It is capable of seeking either steady-state or time-accurate solutions. ANSI2D is an explicit algorithm derived from an earlier implicit scheme discussed in [2.1].

Like its implicit predecessor, ANSI2D regards state vectors to be stored at cell centers rather than at grid nodes. This allows for a variety of grid topologies (including sheared grids with imbedded C-grids and/or O-grids) to be conveniently handled by the algorithm. The program calculates discrete differences along lines connecting cell centers, called inversion lines, two of which pass through each grid cell. Cross-passage inversion lines are called eta-inversion lines; the others (which run in a generally streamwise direction) are called xsi-inversion lines. Values at cell faces are obtained by interpolation between the appropriate cell-centered state vectors.

ANSI2D is also like the implicit scheme discussed in [2.1] in its treatment of boundary conditions. A dummy cell is created on the opposite side of the boundary from each interior boundary cell. The flow properties at the boundary are obtained by interpolation between the interior boundary cell and its dummy cell just like values at any interior cell face are obtained. A subroutine for the appropriate boundary type (inflow, outflow, or solid wall) assigns a value to the state vector for each dummy cell such that the properties interpolated

for the boundary satisfy the appropriate boundary conditions.

ANSI2D is fully documented in [2.2]. The following sections provide a brief summary of its main features. Where program options are available, emphasis is placed on those options chosen for the present work.

2.1.1 Normalized Equations

The unsteady Navier-Stokes equations are normalized as follows:

$$x'=x/L \qquad y'=y/L \qquad t'=tc_{T0}/L$$

$$u'=u/c_{T0} \qquad v'=v/c_{T0} \qquad \mu'=\mu/\mu_{T0}$$

$$\rho'=\rho/\rho_{T0} \qquad p'=p/\gamma p_{T0} \qquad T'=T/T_{T0}$$

where L is the blade axial chord, c_{T0} is the upstream stagnation speed of sound, and γ is the ratio of specific heats. The subscripting $()_{T0}$ denotes an upstream stagnation quantity. All quantities are in the blade relative frame.

The bulk viscosity in the Navier-Stokes equations is defined using Stokes' hypothesis that $\lambda=-2\mu/3$

The resulting equations, expressed in conservation form with primes dropped, are as follows:

$$\frac{\partial U}{\partial t} + \frac{\partial F}{\partial x} + \frac{\partial G}{\partial y} = 0$$

where,

$$U = \begin{bmatrix} \rho \\ \rho u \\ \rho v \\ \rho E \end{bmatrix} \qquad F = \begin{bmatrix} \rho u \\ \rho u^2+p+\sigma_x \\ \rho uv+\tau_{xy} \\ \rho uH+u\sigma_x+v\tau_{xy}+q_x \end{bmatrix} \qquad G = \begin{bmatrix} \rho v \\ \rho uv+\tau_{yx} \\ \rho v^2+p+\sigma_y \\ \rho uH+u\tau_{yx}+v\sigma_y+q_y \end{bmatrix}$$

and,

$$\sigma_x = \frac{2\mu}{3Re}\left(\frac{\partial u}{\partial x}+\frac{\partial v}{\partial y}\right) - \frac{2\mu}{Re}\frac{\partial u}{\partial x} \qquad \sigma_y = \frac{2\mu}{3Re}\left(\frac{\partial u}{\partial x}+\frac{\partial v}{\partial y}\right) - \frac{2\mu}{Re}\frac{\partial v}{\partial y}$$

$$\tau_{xy} = \tau_{yx} = \frac{-\mu}{Re}\left(\frac{\partial u}{\partial y}+\frac{\partial v}{\partial x}\right) \qquad q_x = \frac{-\mu}{PrRe(\gamma-1)}\frac{\partial T}{\partial x} \qquad q_y = \frac{-\mu}{PrRe(\gamma-1)}\frac{\partial T}{\partial y}$$

$$E = \frac{1}{\gamma-1}\frac{p}{\rho} + \frac{1}{2}(u^2+v^2) \qquad H = E + \frac{p}{\rho} = \frac{\gamma}{\gamma-1}\frac{p}{\rho} + \frac{1}{2}(u^2+v^2)$$

Re is the upstream "stagnation Reynolds number" defined as

$$Re = \rho_{T0}c_{T0}L/\mu_{T0}$$

Pr is the Prandtl number whose value for laminar and turbulent flow is specified by the user. In this work the laminar Pr is taken as 0.72; the turbulent Pr as 0.90.

The equation of state is the perfect gas law which, with the above normalization, reduces to $p = \rho T/\gamma$

Viscosity is calculated using Sutherland's law which normalizes to

$$\mu = T^{3/2}\left(\frac{1+S}{T+S}\right)$$

where S is the normalized Sutherland reference temperature which is specified by

the user. In this work it is taken to be $199^{\circ} R/T_{T0}$.

2.1.2 Spatial Discretization and Smoothing

The equations of motion given above are integrated over a closed region R producing the following:

$$\frac{\partial}{\partial t} \iint_R U \, dA + \iint_R (Fn_x + Gn_y) \, ds = 0$$

where n_x and n_y are unit vector components facing outward from the boundary of R. Each grid cell is then regarded as an integration region R.

Discretization is performed by regarding each cell as small enough so that the flux quantities, F and G, may be taken as uniform over the cell face, and the state vector properties at the cell centers taken as uniform throughout the cell. This is known as the finite volume approach. Details are given in [2.2].

The discretization is such that all flux properties at a given cell's faces are determined only from state vector properties at that cell and its immediate neighbors. This results in the basic algorithm being unable to detect or damp non-physical "sawtooth" oscillations of flow properties in the solution. Consequently, numerical smoothing must be added to the algorithm to damp these oscillations. Three types of smoothing are available: fourth-order, second-order, and implicit.

Fourth-order smoothing makes use of information from cells two removed from a given cell and hence is very effective in eliminating sawtooth oscillations. It has been observed by various researchers, however, that in the neighborhood of strong gradients, such as shocks, fourth-order smoothing is undesirable.

Second-order smoothing makes use of information only from a cell's nearest neighbors and is preferable to fourth-order smoothing in the neighborhood of strong gradients.

The smoothing formulation in ANSI2D allows use of both fourth- and second-order smoothing in varying proportions for different spacial locations. In the vicinity of strong pressure gradients such as would be produced by a shock the program automatically decreases the amount of fourth-order smoothing while increasing the amount of second-order smoothing. Again, details are given in [2.2].

For time accurate running, it has been found suitable to eliminate use of second-order smoothing entirely for the present work. Since the flow field does include a shock, this means there is very little smoothing at all applied near the shock. The shock is thus made as clearly defined as possible. No undesirable oscillations have been observed in the solution. Fourth-order smoothing was, by trial and error, set to a value believed to be near the minimum required for stability of the algorithm.

Implicit smoothing is applied to the discrete time integration step to inhibit the formation sawtooth oscillations. It is suitable only for steady-state running. It requires the solution of a tri-diagonal system of equations twice for each cell (once for the xsi-inversion line passing through the cell and again for the eta-inversion line). It requires approximately 15 percent more CPU time per iteration, but allows the discrete time step to be increased significantly — by a factor of 5 in the present work. Thus, implicit smoothing was used to advantage (along with minimal fourth-order smoothing) in obtaining steady-state results.

2.1.3 Time Integration and Stability

The spatial discretization outlined above produces a system of ordinary differential equations in time. These may be symbolically written as

$$\frac{d}{dt}(A_k U_k) + R_k(U) = 0$$

where the subscript O_k indicates cell k, A_K is its area, U is the vector defined in section 2.2.1, and R_K is a non-linear function of U at cell k and its neighbors corresponding to the spatial flux balance, second-, and fourth-order smoothing.

Two methods are offered in ANSI2D for the discrete integration of these equations. The first, dubbed "second-order Runga-Kutta", is a two-step predictor/corrector. This is the method used for the present work. The second method, a modified "fourth-order Runga-Kutta" is discussed in [2.2].

With either method, as for all explicit schemes, there is a limitation on the size of the time step to preserve stability of the algorithm. The physical interpretation of this limitation for the present scheme is as follows. The spatial discretization approximates the flux balance for a given cell only from information at that cell and its nearest neighbors. This flux balance determines the flow properties at the cell at the next time level. Consequently, information can only be transmitted over the spatial distance of a few cells from one time step to the next. In real flows information is transmitted at a maximum rate of c+u, the local speed of sound plus the local flow velocity. Thus, the discrete time step must be less than $\Delta L/(c+u)$, where ΔL is the maximum linear dimension of the cell.

As indicated by the title of [2.2], ANSI2D was originally developed to solve the steady-state Navier-Stokes equations. This was to be done by

integrating only approximately in time. Since the stability requirement is tied to the local cell size, a variable time step was to be used: large time steps for the large cells in the inviscid part of the flow, small time steps for the small cells in the boundary layer. This is, in fact, the steady-state mode of operation, and it was employed to obtain the steady-state results to be presented later.

For time-accurate running, however, it is necessary to use a constant time step throughout the flow field. This limits the size of the time step to that associated with the smallest cell in the grid, a very small value. Consequently, a great number of iterations and a large amount of CPU time have been necessary to obtain the unsteady results to be presented. Approximately 150,000 iterations requiring roughly 1,364 hours (57 days) of CPU time on a Perkin-Elmer 3240 minicomputer have been necessary to simulate about 8 milliseconds of real flow time. The Perkin-Elmer 3240 is roughly equivalent in speed to a VAX 11/780.

2.1.4 Boundary Conditions

Four types of boundary conditions exist in the present work: those associated with the inflow grid boundary, the outflow grid boundary, the blade surface, and the interblade passage boundaries. These will be discussed separately in the following paragraphs.

The program normalizes most flow properties to values associated with blade-relative stagnation quantities at the inflow boundary (see section 2.2.1) which are taken as uniform along the boundary and constant in time. The user specifies the "stagnation Reynolds number" at the inflow boundary. The flow angle (also uniform and constant in time) is specified as well. The "unique

incidence principle" for supersonic cascades (see [2.3]) precludes the specification of flow angle for supersonic inflow conditions. Thus, in its present form, ANSI2D can be used to simulate subsonic inflow conditions only. This proved to be a significant limitation in the present work, and will be discussed further in Chapter 3. Regions of supersonic flow in the interior of the computational domain pose no problems, and do in fact exist in the results to be presented.

The outflow boundary condition is uniform and time constant static pressure. This value of static pressure is specified by the user. This boundary condition is not physically realistic for individual stages of multistage turbomachines, although a better alternative is difficult to construct. In the present work, the outflow boundary has been placed far enough downstream of the blade trailing edge (about 1 chord) so that it is hoped the uniform static pressure condition does not obscure physical characteristics of the real flow in a turbomachinery environment. As will be discussed later, it is believed that this goal has been achieved.

The boundary condition at the blade surface is the usual no-slip, no-throughflow condition. ANSI2D allows the user to specify the blade surface to be either adiabatic, or to have a specified constant temperature. In the present work the adiabatic condition has been chosen.

ANSI2D models the flow in a cascade of blades though only calculating the flow in a single blade passage. It does so by imposing periodic boundary conditions on the interblade passage boundaries. This affects the applicability of calculated results to real turbomachinery flows because it eliminates all unsteady flows in which there is a blade to blade phase difference in unsteady events. That is, ANSI2D can only predict flows in which time varying events occur exactly in phase for all blades in the cascade. This problem is

unimportant for flows in which blade to blade interactions are small.

2.1.5 Handling of Turbulence

ANSI2D assumes turbulence to be limited to the boundary layers and simulates it by an increase in the coefficient of viscosity. In effect, then, ANSI2D approximates the unsteady Navier-Stokes equations after they have been Reynolds averaged only over the short time scales associated with turbulence.

The turbulent viscosity is approximated by a "zero equation" (algebraic) model discussed briefly in [2.4]. Specific parameter values are given in [2.2].

The user must specify fixed locations on the blade surface where transition to turbulence is taken to occur. The estimated turbulent viscosity is added to the molecular viscosity at and after these specified locations (one for the pressure surface, one for the suction surface). The present code does not allow for user-specified re-laminarization. To avoid non-physical gross separation from separating laminar boundary layers near the leading edge, the transition locations have both been placed very near the leading edge in the present work (less than 1 leading edge diameter downstream of the axial leading edge).

2.1.6 Additional Remarks

Shocks are handled by smearing the change in flow properties over several grid cells. No automated grid adaptation or shock capturing features are present in the scheme. The Rankine-Hugoniot relations are satisfied sufficiently well for most applications. As mentioned in section 2.2.2, a minimum of smoothing was used in the vicinity of the shock allowing it to be as

sharply defined as possible. In the present work, it appears that flow changes corresponding to the shock are smeared over about 5 grid points. This is discussed somewhat further in section 4.2.1.

The presence of numerical smoothing tends to diffuse calculated propagating structures more quickly than would occur in real flows. The smoothing formulation allows roughly stationary regions of strong gradients, such as shocks, to remain undiminished. Other structures involving significant gradients of flow properties, such as shed vortices, are also allowed to form, and are a prominent part of the results to be presented. However, these structures become unrecognizably diffuse within about a 1/4 chord downstream of the blade trailing edge. In real turbomachinery flows, experimental results suggest that such vortices may persist for several chord lengths.

2.2 Method of Investigation

After selecting a compressor airfoil geometry and generating a suitable computational grid (see Chapter 3), ANSI2D was run in steady-state mode until reasonable convergence was obtained (see Chapter 4). The program was then run in time-accurate mode using the steady-state solution as a starting point.

ANSI2D produces two outputs: (1) a new flow field file (solution file) available after each time step (i.e. after each iteration), and (2) a convergence history file (updated after each iteration). The convergence history file contains five pieces of information for each iteration: (1) the iteration number, (2) the root-mean-square (RMS) change in flow properties over the entire spatial domain from the preceding solution to the current one, (3) the largest change in flow properties at any computational cell from the preceding solution to the current one, (4) the location of this largest change,

and (5) the quantity (ρ, ρu, ρv, or ρE) in which this largest change occurred. In steady-state mode it is expected that the changes in flow properties from one iteration to the next will eventually approach zero. Hence the convergence history file gives the level of error present in the computational simulation after each iteration. In time-accurate mode the program is capable of simulating unsteady flow fields. Hence in this case the convergence history file does not necessarily indicate the error level, but only the level of unsteadiness in the flow simulation. As will be shown later, the time-accurate convergence history is useful in determining the frequency of periodic flow field changes.

It was unnecessary to examine the solution file after every iteration in order to adequately analyze the time-accurate results. Further, saving solution files for every iteration would require prohibitively large storage space. Therefore, solution files were saved after every 250 iterations. This provided adequate time resolution for the analysis.

Time-accurate running of ANSI2D was generally done in segments of 2500 iterations. Each segment required approximately 23 hours of CPU time to complete on a Perkin-Elmer 3240 minicomputer, and saved 10 solution files on disk.

Certain information was extracted from each solution file and appended to other files which remained on disk. Analysis of these files yielded complete time histories of certain flow field properties. The information extracted was the following:

1. Pressures over the entire surface of the airfoil. From these the force and moment on the blade (neglecting skin friction) could be calculated at each time level.

2. All basic flow properties along specified inflow and outflow boundaries. From this information many things could be calculated including mass averaged and "stream-thrust averaged" quantities at each time level, time averaged quantities along each boundary, and simulated readings from a stationary probe. These calculated quantities could be presented in either the relative frame or in a hypothetical absolute frame of reference.

3. Boundary layer separation point locations, and vorticity flux at selected locations along the blade.

4. Maximum Mach numbers along selected streamwise lines. Since the flow field included a cross-passage shock, this information gave an indication of the time varying shock strength and location.

5. Skin friction, temperature, and temperature gradient normal to the wall over the entire surface of the airfoil.

After this information was extracted from the solution files on disk, the solution files were copied onto magnetic tape for permanent storage. The convergence history file was also copied onto tape. To conserve disk space these files were then deleted from disk storage and another segment of 2500 iterations initiated.

CHAPTER 3
AIRFOIL GEOMETRY, HYPOTHETICAL OPERATING CONDITIONS, AND COMPUTATIONAL GRID

3.1 Airfoil Geometry

The airfoil modeled in the present study is a section of the NASA Low-Aspect-Ratio first stage fan rotor reported on in [3.1]. This rotor will be referred to as NASA Rotor 67. The rotor has a hub-to-tip radius ratio of 0.375 at its inlet and 0.478 at its exit. Its aspect ratio is 1.56. Its design speed is 16042.8 RPM. It has been tested in NASA Lewis's steady-state test rig at 103 percent corrected speed with a mass flow of 34.03 kg/sec (75.0 lbm/sec) and developed a total pressure ratio of 1.686 with an adiabatic efficiency of 0.906. These conditions correspond to a tip relative Mach number of 1.31.

This rotor was chosen because extensive unsteady experimental data have been taken on it by Gertz [3.2]. Most of this data is at a location 60 percent of the blade span from the hub. This location corresponds approximately to blade section 5 in [3.1]. A location such as this, near mid-span, is also the flow region most likely to approximate two-dimensional flow.

Blade section 5 is defined in [3.1] on a shallow cone of inclination -2.073 degrees from horizontal. This approximates a streamline location obtained from a streamline curvature calculation. A cone cannot be exactly unwrapped into two dimensions. This section has been unwrapped in such a way as to preserve the most important geometric parameters. The section is defined by a double circular arc meanline and a thickness distribution. The two-dimensional meanline was constructed by preserving the given inlet angle, outlet angle (hence total geometric turning), axial chord, the ratio of the two radii

describing the meanline, and the fraction of the axial chord at which these radii meet. Since the cone is shallow, all other geometric parameters, including setting angle and total chord, are closely approximated. Table 3.1 summarizes the resulting two-dimensional meanline geometry.

The only thickness information given in [3.1] is the leading edge thickness (diameter of leading edge arc), trailing edge thickness, the difference between the meanline angle and the suction surface angle at the leading edge, the maximum thickness, and the axial location of the maximum thickness. A polynomial fit consistent with these data was used to complete the thickness distribution. The maximum thickness to total chord ratio is 4.55 percent. Figure 3.1 shows the final blade shape.

3.2 Hypothetical Operating Conditions

As implied above, an original goal of this research was to compare computational results with experimental data for similar operating conditions. The inlet relative Mach number at 60 percent span for the conditions reported in [3.2] is approximately 1.17. However, as mentioned in section 2.2.4, ANSI2D is not capable of handling a supersonic inflow condition. To remedy this would have involved formulating a new inflow boundary treatment, writing a new subroutine for ANSI2D, and testing the resulting code on cases in which the physical flows are known. Instead, a direct comparison against the data of [3.2] was forfeited in favor of running ANSI2D unmodified with a high subsonic inflow Mach number.

At a variety of off-design conditions, NASA rotor 67 does operate with subsonic relative Mach numbers at 60 percent span. One such case (at 100 percent speed) was modeled early in the research program. However, the

resulting calculated flow field was complicated by large scale separation from the leading edge. This is probably due to one or both of the following considerations: (1) this flow had a high leading edge incidence angle of about 6 degrees, and (2) the turbulence transition locations for this case were set away from the leading edge at roughly mid-chord. It was decided that a simpler flow field was desirable as a baseline case. The leading edge separation was eliminated by specifying an inlet flow angle giving zero incidence at the leading edge, and by moving the turbulence transition locations very near the leading edge (see section 2.2.5).

ANSI2D normalizes calculated flow quantities to inflow relative stagnation quantities. A particular real flow can be contemplated by assigning values to these reference quantities. Further, the rotor can be imagined to be rotating at a certain speed. Hypothetical absolute conditions can then be found which correspond to the imagined relative stagnation conditions.

This has been done for the calculated results to be presented. The complete hypothetical operating conditions are given in Table 3.2. The inlet quantities are the most significant values in the table, especially the inlet relative total quantities (PT, TT, MUT). It is to these values that quantities calculated by ANSI2D are taken to be normalized to in the chapters that follow. For example, all frequencies to be reported are based on these hypothetical conditions. (When values such as velocities or pressures are reported later with no units given, however, they are normalized values as defined in section 2.1.1.) Notice that the rotor is taken to be running at an atmospheric pressure slightly above sea-level standard (15.056 psi) on a cool day (510.00 - 459.67 = 50.33 degrees F) at 100 percent corrected speed. Prewhirl vanes are imagined to be in front of the rotor which turn the incoming flow through 24.399 degrees so that the relative flow angle is 56.810 degrees. Since the leading edge meanline blade angle is 56.810 degrees, this gives a zero incidence condition. The

relative Mach number is about 0.92. The relative Reynold's number is 1.17×10^6 based on the axial chord. Based on the true chord it is 1.83×10^6.

The exit conditions shown in Table 3.2 correspond only approximately to those produced by ANSI2D. They were obtained by satisfying continuity of mass flow from inlet to exit given a value for the loss of relative total pressure (0.97 in this case which is near the value predicted by ANSI2D). If these conditions were actually observed, the rotor section would be operating with a total pressure ratio of 1.29 at an adiabatic efficiency of 88.9 percent.

3.3 Computational Grid

The grid used in this work is a sheared grid with a C-grid imbedded to better resolve the blade boundary layers and wake. It is shown in Figure 3.2. Enlargements of the leading edge and trailing edge regions are shown in Figures 3.3 and 3.4. These figures show the grid cells; the inversion lines pass through the centers of these cells.

The outermost line in the C-grid was defined by a crude estimation of the boundary layer growth based on expected operating conditions. Fifteen grid lines (giving 14 xsi-inversion lines) were placed in the C-grid. They are exponentially spaced giving greatest resolution near the blade surface.

The location of the grid boundary layer edge is only significant in the turbulence modeling. The molecular viscosity is augmented by the estimated turbulent viscosity only within the grid boundary layer. The equations of motion solved by ANSI2D are always the Reynolds averaged Navier-Stokes equations; the boundary layer approximation is not employed. In the present work the boundary layer thickness for both surfaces near the trailing edge was

underestimated. In this region the velocity parallel to the blade surface reaches its "free stream" value approximately twice as far from the blade surface as the last inversion line in the C-grid.

The sheared grid fills in the upstream space and the core flow region between the blades and wake. It has 28 streamwise lines (giving 29 xsi-inversion lines) which are also exponentially spaced so as to give the greatest resolution near the boundary layer edges. Care was taken to avoid a large change in cell size at the junction between the sheared grid and the C-grid.

The cross-passage grid lines (defining the eta-inversion lines) were spaced so as to adequately resolve the leading and trailing edges and yet keep the overall number of grid cells reasonable. Exponential spacing was used where needed to provide smooth transitions in cell size.

The final grid (dubbed the "Pass 45 Grid") has 7108 interior cells and 226 boundary cells for a total of 7334 cells. There are a total of 57 xsi-inversion lines running in the streamwise direction within the bladed region: 14 in each boundary layer, 29 in the core. There are a total of 136 eta-inversion lines (running cross-passage), 70 of which are in the bladed region.

CHAPTER 4 STEADY STATE RESULTS

4.1 Convergence Behavior

ANSI2D must always start its iterations toward a solution from a file which approximates the flow field. Usually this is a solution file generated previously by ANSI2D. However, to start the program on a new grid it is necessary to generate the "initial solution" file artificially. The steady state iterations were started from such a file in which the flow conditions were only crudely approximated. The flow direction was made constant throughout the region outside the grid boundary layers. The inlet Mach number and exit Mach number were specified, and interior Mach numbers linearly interpolated from these. An approximate boundary layer velocity profile was generated within the grid boundary layers.

ANSI2D was started in steady state mode (variable time step) from this solution. The local CFL number was specified as 4.0, the second-order smoothing coefficient set at 0.0, the fourth-order smoothing coefficient set at 0.075, and the implicit smoothing coefficient set at 4.0. The use of implicit smoothing allows the large (greater than 1) local CFL number.

Figure 4.1 shows the convergence history for the first 2500 iterations. It is observed that the error reaches a minimum after about 1700 iterations and then fails to converge further. In fact, the error tends to increase after 1700 iterations. Experience has shown that the level of convergence never improves significantly beyond this no matter how many iterations are performed.

Figure 4.2 shows the locations of the maximum errors for the first 2500 iterations. The figure is understood as follows. After each iteration ANSI2D

identifies the cell at which the maximum change in flow properties occurred from the previous iteration. A square symbol is plotted in Figure 4.2 at this cell. The same cell may be the location of the maximum change for other iterations as well. This is indicated in Figure 4.2 by the size of the square symbol. A large square indicates that the cell in question was often the site of maximum error; a small square indicates that the maximum error occurred at the marked cell only a few times. Figure 4.2 is thus a sort of two-dimensional histogram of the steady state error.

There are small symbols scattered throughout the flow field in Figure 4.2, most of them in or near the boundary layer region, which indicate adjustments made to the starting "solution." It is evident, however, that the trailing edge is the site of the vast majority of the error. This is typical of flow fields in which vortex shedding is present. The physical presence of vortex shedding means that the flow is inherently unsteady: the Navier-Stokes equations have no steady state solution for such a flow (or if a mathematical steady state solution exists, it is unstable). Consequently, a steady state approximation to the Navier-Stokes equations will never fully converge, the error locations being predominantly near the shedding location (the blade trailing edge in this case).

The failure of the algorithm to converge in steady state is demonstrated by the variation in mass flow rate through the passage, shown in Figure 4.3. The total variation upstream of the trailing edge is slightly less than two percent. The variation near and downstream of the trailing edge is over three percent. This variation does not decrease to satisfactory levels with more iterations.

4.2 Basic Flow Field Characteristics

Despite the lack of full convergence, the steady state solution

nevertheless displays the same basic flow phenomena as are found in the time-accurate solutions. The most important of these are the passage shock and its effect on the suction surface boundary layer.

4.2.1 Passage Shock

Figure 4.4 is a contour plot of Mach number for iteration 2500. As indicated by the sonic line, a shock extends across the entire passage approximately from the 1/4 chord point on the pressure surface to the 3/4 chord point on the suction surface. The shock may be considered normal to the flow. Its strength varies across the passage being strongest near the suction surface. The maximum pre-shock Mach number there is 1.286 and decreases to 1.207 at mid-passage, and 1.169 near the pressure surface. The complicated nature of the contour lines downstream of the trailing edge is evidence of the lack of full steady state convergence.

The shock arises from the passage area becoming critical (probably due to growth of the boundary layers). Figure 4.4 shows that the flow is sonic or nearly so across the passage at the inlet throat and shocks about 1/4 chord further downstream. It is emphasized that the far upstream flow conditions are subsonic, and thus that the shock is not a bow shock or a swallowed shock as are found in supersonic compressors.

Determining the actual strength of the shock is complicated by its being smeared over several grid cells. The problem will be illustrated by considering the shock at mid-passage. Table 4.1 lists the local Mach numbers at each cell along a segment of xsi-inversion line 15 (the mid-passage streamwise line through cell centers). Suppose the shock is considered to begin at cell 53. Using the normal shock relations, the post-shock flow conditions can be found

based on the Mach number, pressure, and temperature at cell 53. Flow conditions at the cells downstream of cell 53 can then be compared against the expected values until the best match is found. At each cell there will be an error in the Mach number, pressure, and temperature compared to the expected values. The root-mean-square (RMS) of these errors gives an indication of the overall error. The downstream cell at which the RMS error is minimized is considered to be the termination of the shock. This process can be repeated considering cells other than 53 to be the beginning of the shock. The results are shown in Table 4.2.

The normal shock relations are best satisfied by considering the shock to be smeared over five cells from cell 55 to cell 60. This corresponds to a physical normal shock with pre-shock Mach number of 1.164. The shock is smeared over a linear distance of approximately 0.085 blade chords. The difference in flow angle between cells 55 and 60 is 1.4 degrees. This turning would be produced by an oblique shock at an angle of 84.8 degrees. The normal shock approximation is thus considered to be justified.

4.2.2 Suction Surface Boundary Layer Separation

Whereas the pressure surface boundary layer remains attached until the blade trailing edge, the suction surface boundary layer separates. Figure 4.5 shows the location of this separation (as indicated by zero surface shear stress) together with the approximate smeared shock location. The separation occurs slightly downstream of the shock and is thus not properly termed "shock-induced." This is more evident in the time-accurate results in which the movement of the separation point does not follow the movement of the shock. There is little doubt, however, that the shock hastens the boundary layer separation.

4.3 Blade Performance

Average values on which to base statements of overall blade performance have been obtained using two methods. The first is the familiar process of mass averaging. The second will be referred to as "stream-thrust averaging." The fluxes of mass, momentum, and energy are obtained by integrating the non-uniform flow conditions at a given location. A uniform flow is then solved for which has these same fluxes, with pressure differences accounted for in the momentum equations. The average flow thus calculated is what would result if the actual non-uniform flow were to mix out in a constant area duct.

Table 4.3 presents the overall blade performance obtained by both averaging methods applied at an axial location 1.6 trailing edge diameters downstream of the trailing edge. Absolute quantities are based on the hypothetical operating conditions discussed in section 3.2. Depending on the averaging method employed, the blade section produces a total pressure ratio of 1.292 or 1.280. The meanline blade exit angle is 43.24 degrees. Therefore the relative exit flow angle of either 48.59 or 51.84 degrees reflects a deviation angle of 5.4 or 8.6 degrees respectively. The stream thrust averaged efficiency is 90.1 percent, more than two points lower than the mass averaged value of 92.8 percent. This is typical of stream thrust averaging, and tends to more accurately indicate the true performance in an engine environment. The non-averaged variation in relative total pressure at this station is shown in Figure 4.6.

Blade forces and moments (from integration of surface pressures) are also known for the steady state solution. The presentation of these will be delayed, however, because they are more insightful when viewed in comparison with the time-accurate results.

CHAPTER 5 OVERVIEW OF UNSTEADY RESULTS

Time accurate running was initiated from a steady state solution. ANSI2D was allowed to run for a number of iterations corresponding to about two computational domain through-flow times before the time-accurate solutions began to be saved for analysis. The unsteady results to be presented are thus thought to be due to more than merely computational transients from the unconverged steady state starting solution. The starting solution did, however, provide a large perturbation to excite instabilities or natural frequencies in the time-accurate flow.

5.1 General Nature of the Unsteadiness

A segment of the time-accurate "convergence" history is shown in Figure 5.1. Unlike the steady state convergence plot, this is not a plot of error level. Figure 5.1 shows the maximum and RMS changes from one iteration to the next. In time-accurate running this is simply an indication of the unsteadiness of the flow. Note that periodicity is evident. The primary usefulness of these plots is in determining from this periodicity the frequencies of the vortex shedding (discussed in Chapter 6). The locations of maximum changes are shown in Figure 5.2. As expected, the greatest unsteadiness is near the blade trailing edge.

The most significant aspect of the time-accurate results to be presented is the presence of two distinct frequency regimes. The high frequency variations are due to vortex shedding. This phenomenon (discussed in detail in Chapter 6) was expected from the experimental data reported in [3.2] and serves to confirm

many of the conclusions drawn in that work. The frequency of the shedding computed by ANSI2D is 11 KHz and higher. The low frequency variation was unexpected, and occurs at approximately 365 Hz. It will be discussed in detail in Chapter 7.

Figures 5.3 through 5.5 present time histories of the blade lift, drag, and moment normalized to the upstream dynamic pressure and the blade axial chord. Lift and drag are calculated in analogy with isolated airfoil theory, lift being defined as the component of force normal to the upstream flow direction, drag parallel to the upstream flow. Figure 5.6 shows the moment center on which Figure 5.5 is based. Several observations may be drawn from these figures, and are discussed in the following paragraphs.

The two frequency regimes are easy to see. The small ripples in these curves are due to the vortex shedding, which is superimposed upon a variation of much lower frequency.

The frequency and character of the vortex shedding are modulated by the low frequency variation. The shedding is strong during part of the low frequency cycle, i.e. its presence is easily seen in the overall blade force and moment. During the other part of the low frequency cycle, the shedding is weak being at times virtually undetectable in the overall force and moment. The strong shedding occurs at lower frequencies than the weak shedding. The total frequency range is approximately 11 KHz to 19 KHz.

The variation in vortex shedding strength is also evident in the convergence history plots. Figure 5.1 is a segment of the convergence history during which the shedding was strong. The periodicity is easy to see and measure. Figure 5.7 is a segment during which the shedding was weak. Periodicity is not obvious. The exact frequency of the weak shedding could not

always be determined.

The frequencies of the vortex shedding observed in the computation are in the range expected from Gertz's data presented in [3.2]. The shedding measured by Gertz was estimated to have a frequency f of approximately 15 KHz. The inlet relative Mach number at 60 percent span in his tests was about 1.17. The inlet relative Mach number in the computation is about 0.92. Assume that the shedding frequency is normalized by a length L and a velocity V. Assume also that the normalized shedding frequency fL/V is approximately the same for both experiment and computation, and that the length L is approximately the same in both cases. The expected shedding frequency for the computation would then be about 11.8 KHz. The average shedding frequency (total number of cycles divided by total time) observed in the computation is 13.8 KHz (17 percent greater than 11.8 KHz). This is considered to be good agreement given the approximate nature of the assumptions made above.

The lift, drag, and moment all vary significantly over the low frequency cycle. The total variation is defined as (maximum value - minimum value) / mean value. The total variation of lift is 5.21 percent, the total variation of drag is 13.13 percent, and the total variation of moment is 31.53 percent.

The flow variations due to the low frequency cycle are much greater than those due to the vortex shedding. Consider the blade moment for example. The largest variation in moment over one vortex shedding cycle is only about 1 percent of the time averaged moment. However, the largest variation due to the low frequency cycle is over 30 percent of the time averaged moment, as mentioned above. As will be discussed later, other gross flow field changes such as shock and separation point movement also occur at the low frequency; they are not seen to vary at the vortex shedding frequencies.

The large variations in blade forces due to the low frequency cycle are potentially important structural concerns. It happens that the frequency of these variations in the present computation (365 Hz) is near the real rotor's first bending frequency.

The low frequency variations of drag and moment appear to be in phase with one another, both lagging the lift by about 90 degrees.

The low frequency variations seem to be damping out. The decrease in the AC components is approximately exponential, the amplitude being multiplied by 1/e about every 4.7 milliseconds. This feature especially raises the question of whether these variations are mere numerical artifacts. The present investigation cannot answer this question conclusively. However, the nature of the low frequency cycle is worth studying seriously for several reasons.

(1) A mechanism whereby these fluctuations might be created by the numerical approximation is not evident at present. Several possibilities are considered in Chapter 7.

(2) A mechanism by which a real fluid dynamical cycle might be artificially damped by the numerical approximation is evident. The damping could be due to the effects of numerical smoothing over a large number of iterations. (Each low frequency cycle requires about 41000 iterations to complete.)

(3) The low frequency cycle is physically realistic. It is similar in many respects to cycles observed in transonic diffusers.

(4) The magnitude of these fluctuations is large enough to make them a significant factor in the design of transonic compressors if in fact they do represent a physical phenomenon.

Figure 5.8 presents instantaneous surface temperature distributions along

the blade for two different times in the low frequency cycle. The "surface length" is defined as negative along the pressure surface (with the most negative value being the trailing edge), zero at the leading edge, and positive along the suction surface (ending again at the trailing edge). Recall that the blade surface is given an adiabatic (zero heat transfer) boundary condition in the work presented here. It is clear from Figure 5.8 that the temperature distributions necessary to support the adiabatic boundary condition would lead to significant heat transfer along the surface of the blade itself. In the shock regions, heat fluxes of 13 to 43 KW/m^2 would exist along the blade surface (taking the blade to be titanium with a thermal conductivity of 9 BTU/hr/ft/$^{\circ}$F). The temperature distribution continually adjusts itself to maintain zero heat flux between the blade and the fluid. Such an adiabatic condition is very unlikely in a real unsteady flow. Perhaps a better approximate boundary condition is one in which the blade is assumed to have a high enough thermal inertia to maintain a constant temperature distribution. In this case, heat will be transferred from the flow to the blade and vice versa over the course of a time-varying flow cycle.

5.2 Comparison with Steady State Results

Table 5.1 presents the maximum range of unsteady values, the time averaged values, and values obtained from steady state iteration 2500 for a number of quantities of interest.

Table 5.2 is a further analysis of the information presented in Table 5.1. The total variations are calculated by dividing the difference between the maximum value and the minimum value by the time averaged value. For flow angles and efficiencies only the difference between the maximum and minimum values are tabulated (indicated by the symbol $\triangle$). The last column is calculated by

subtracting the time averaged value from the steady state value and dividing by the time averaged value. Again, the symbol Δ is used to indicate when only the difference appears.

It may be observed that the steady state solution significantly underpredicts the lift on the airfoil leading to a mild underprediction of the absolute total pressure ratio. It is also noteworthy that regardless of the averaging technique used, the steady state solution significantly overpredicts the adiabatic efficiency.

In this connection, it should be noted that the time-averaged efficiencies presented in Tables 5.1 and 5.2 have been obtained by using the time-averaged total pressure and total temperature ratios in the standard formula; they are not the result of time averaging all the instantaneous efficiencies. As Gertz has shown in [3.2], the instantaneous efficiency is not a good indication of the local instantaneous loss in an unsteady flow. The large difference between the time-averaged and steady state efficiencies is therefore the result of the seemingly small differences in the total temperature and total pressure ratios. The efficiency (and entropy change as well) is quite sensitive to small changes in these ratios, especially in the total temperature ratio, as demonstrated by the sample calculations presented in Table 5.3.

These comparisons have been made against steady state iteration 2500. Because of the lack of convergence, the steady state "solution" changes with the number of iterations. Somewhat different quantitative results would be obtained by examining different steady state solutions, but the qualitative character of the solution and its general relation to the time-accurate solutions is thought to be well represented by iteration 2500 discussed above.

CHAPTER 6 HIGH FREQUENCY UNSTEADINESS: VORTEX SHEDDING

As mentioned in Chapter 5, the strength and frequency of the vortex shedding is modulated by the low frequency cycle. Vortex shedding is described as "strong" or "weak" in this context based on the magnitude of the effect it has on the blade force and moment. The details of the strong shedding will be discussed first followed by a briefer discussion of the weak shedding. Finally the normalization of the frequencies and the mechanics of the strength variation will be discussed.

6.1 Strong Shedding

That the high frequency unsteadiness near the blade trailing edge is in fact due to the shedding of vortical structures into the wake can be seen by examining a plot of velocity vectors. Figure 6.1 is such a plot. A vector is plotted at every state vector location (each cell center) and also at cell faces (interpolated between cell centers). The length of each arrow is proportional to the magnitude of the instantaneous velocity at the origin of the arrow, and it points in the direction of the velocity. Figure 6.1 clearly shows the presence of vortical structures in the wake.

Figure 6.1 is misleading, however, as to the number and location of the vortices. This is because the vortices themselves are moving with a velocity that cannot be neglected. The zero velocity points in Figure 6.1 are not vortex centers since the vortex centers do not have zero velocity in this frame of reference. To reveal the true location and structure of each vortex, one must view velocity vectors in the instantaneous frame of reference of that moving vortex. In such a frame of reference the vortex center will be a point of zero

velocity.

A convenient method of locating the vortices is thus desired. Ideally, a scalar quantity which is independent of the frame of reference and which reveals the vortex locations is desired. Static pressure is such a quantity. The vortex centers must be local minima in the instantaneous static pressure field.

Figures 6.2 through 6.4 each show a small number of pressure contours from the same instantaneous solution as shown in Figure 6.1. The three figures reveal the locations of three vortices. As will be shown momentarily, two are of counterclockwise rotation and were shed from the pressure surface boundary layer, and one is of clockwise rotation shed from the suction surface.

Two methods may be used to determine the instantaneous propagation velocity of vortices whose locations have been determined. First, the location of the same vortex may be found at different times and its velocity estimated by a finite difference formula. Second, the velocity in the blade relative frame at the location of the vortex center may simply be read off the velocity vector plot for the same instant of time. The latter method is, of course, more expedient, but it has been verified that the two techniques do give the same result within reasonable bounds.

Velocity vector plots in the instantaneous frame of reference of each vortex identified in Figures 6.2 through 6.4 are presented in Figures 6.5 through 6.7. In these figures a circle has been drawn at the center of the vortex into whose frame of reference the velocities have been translated. The normalized velocity of the vortex (which has been subtracted from the blade-relative velocities to produce the figure) is also indicated. It can be seen that the sign of rotation is as was indicated in the earlier figures. It is noteworthy that the second pressure surface vortex is greatly weakened and

diffuse at a downstream distance from the trailing edge of only about 0.1 blade chords. Vortices could not be positively identified at distances greater than 0.2 blade chords downstream. This rapid diffusion is due to the numerical smoothing in the algorithm (see section 2.1.2).

Figure 6.8 is a master plot of the locations of all vortex cores found in solutions stored between and including iterations 42000 and 43500. Since solutions were stored every 250 iterations, this comprises iterations 42000, 42250, 42500, 42750, 43000, 43250, and 43500. These solutions are like snapshots of the flow at seven equally spaced instants of time. Pressure surface vortices may be seen at nearly identical positions near the trailing edge for iterations 42250 and 43500. This sequence thus corresponds to slightly more than one shedding cycle. The figure approximates a locus of vortex core locations showing the paths followed by the vortices as they propagate downstream. Notice that the distance between the locations of the same vortex at consecutive times increases as the vortex moves further from the trailing edge. This means that the vortex propagation speed increases downstream of the trailing edge region.

The vortex street spacing ratios can be found by examining the locations of vortices at a given time level. Figure 6.9 shows the vortex centers for iteration 42250. As shown in the figure, the normal distance between vortex rows is called h whereas the streamwise distance between vortices in a row is called b. The spacing ratio b/h at this instant in time is 2.82 (h/b = 0.35). Figure 6.10 shows the same vortex centers at the next time level (iteration 42500). Here b/h is 3.53 (h/b = 0.28) which is very near the Karman value of 3.56. Figure 6.11 shows the spacing at iteration 42750 where b/h is 4.36 (h/b = 0.23). It is observed that the vortex street tends to "stretch" (b/h increases) with increasing distance from the trailing edge. This contrasts with experimental measurements of vortex streets behind bluff bodies at low Reynolds

numbers (see for example [6.1]). The experiments in [6.1] show the street tending to "broaden" (b/h decreasing). A possible reason for this difference as well as others between classical vortex streets and the one encountered in the present computation will be discussed in the following paragraphs.

The classical Karman vortex street is the result of the instability of two initially parallel free shear layers. These layers are usually the two separated boundary layers which emerge behind a bluff body. As shown by Roshko in [6.2], the resulting normalized frequency (Strouhal number) based on the initial separation between the free shear layers and the free stream velocity at their separation locations is of order 0.2 over a broad range of Reynolds number.

In most cases these layers can be well approximated as infinitely thin vortex sheets, and can be further approximated numerically as rows of discrete vortices (as in [6.3] and elsewhere). As demonstrated in [6.3], initially parallel vortex sheets are unstable to general perturbations (both in local vortex strength and in shape of the sheet). When perturbed, the two sheets interact with each other so as to form regions of concentrated vorticity in the configuration of a vortex street. As shown in [6.3], the details of this interaction explain both why the vortex street tends to broaden with downstream distance and why each region of concentrated vorticity contains only about 60 percent of the vorticity found in the originating boundary layers. Flow visualizations of flow around circular cylinders in the "subcritical" Reynolds number range (i.e. before turbulent reattachment occurs) show that the first vortex arising from the twin layer instability forms no closer than about one cylinder diameter downstream of the cylinder (e.g. figures 94, 96, and 47 in [6.4]; also 32 for shedding from an ellipse).

Single shear layers are also unstable to perturbations and tend to roll up

into regions of concentrated vorticity (see [6.3] and [6.5]). This is a distinct phenomenon from the twin layer instability and, in fact, the two can occur side by side in the same flow (see [6.5]).

An examination of Figure 6.8 reveals that the vortex shedding observed in the present computational results is not likely to be due primarily to the twin shear layer instability. The pressure surface vortices are seen to originate very close to the trailing edge: too close for significant interaction with the suction surface boundary layer to likely have occurred. The suction surface vortex forms at a location such that the pressure surface boundary layer is almost hidden by the blade itself making interaction between the two free shear layers unlikely.

The formation of the intense pressure surface vortex very near the trailing edge appears to be a single shear layer rollup which is accelerated by an instantaneous pressure gradient across the (blunt) trailing edge (which is timed to the passing of the suction surface vortices). It bears resemblence to starting vortices (see, for example, Figures 5.10.5 number 1, 6.7.2, and 6.7.5 in [6.6]).

The suction surface shear layer exists as a free shear layer for a distance of several boundary layer thicknesses as shown by the typical suction surface separation location indicated in Figure 6.12. It thus has the opportunity to roll up due to the single layer instability as well. There is no evidence that the suction surface vortex actually forms, however, until the proximity of the trailing edge as shown in Figure 6.8. Although the vortex is thought to be formed from the suction surface shear layer alone, its formation is prompted by the proximity of the strong pressure surface vortex. Notice that the suction surface vortex forms at a normal distance from the suction surface of several trailing edge thicknesses.

The suction surface vortex falls into line with the previously formed vortices at roughly the Karman spacing ratio (which has a certain degree of stability associated with it). The twin layer interactions discussed in [6.3] which cause street broadening are not present, or at least do not appear to be dominant. Since the vortices gain speed as they leave the trailing edge region the street tends instead to stretch.

When vortex shedding was first identified in compressors, it was natural to view the thin but locally blunt trailing edge as the rear face of a classical bluff body. However, the shedding frequencies observed in compressors do not typically yield a Strouhal number of order 0.2 based on the trailing edge thickness. For example, the shedding frequency in the present case would have to be 83 KHz (over four times the observed values) in order to yield a trailing edge thickness Strouhal number of 0.2. Part of the reason for this is no doubt to be found in the fact that the boundary layers in compressors are usually thick compared to the trailing edge thickness, and are not well approximated as infinitely thin vortex sheets (see the discussion of this approximation in [6.3]). The mechanics of the street formation suggested above, however, may further explain the situation. A Strouhal number of about 0.2 is expected only for a vortex street arising from a twin shear layer instability which does not seem to be dominant here. An alternate length and velocity scale with which to normalize the shedding frequencies will be discussed in section 6.3.

6.2 Weak Shedding

The mechanics of the weak shedding appear to be the same as for the strong shedding. The shedding is "weak" in that it does not have as noticeable an effect on the blade forces and other flow parameters as the strong shedding does. This is because the vortices which form the vortex street are themselves weaker than in the strong shedding case.

An indication of vortex strength is the approximate pressure at the vortex core (a local minimum). A sample of approximate vortex core pressures for both the strong shedding and the weak shedding cases is presented in Table 6.1. As indicated by the sketch below the table, each column follows the same vortex, each identified by its relative position in the street and by whether it formed from the pressure surface boundary layer (PS) or the suction surface boundary layer (SS). The table entries in the first two columns are blank when the vortex has not yet formed; question marks appear in the table where the vortex is believed to exist, but its core pressure is uncertain; dashes appear where the vortex could no longer be found. Two observations may be made. First, in the strong shedding case, the core pressure of a given vortex is sometimes seen to decrease as it propagates downstream. This is because the vortex is still forming: its strength is increasing as it continues to be fed by vorticity from the appropriate boundary layer. Eventually all vortices are seen to decay as they propagate away from the trailing edge. Second, the minimum core pressure of vortices in the weak shedding case is always greater than vortices in the strong shedding case. That is, the static pressure "well" is not as deep for the vortices formed in the weak shedding phase. This indicates that these vortices are, in fact, weaker. Reasons for the decrease in vortex strength will be discussed in section 6.3.

These weaker vortices are more difficult to identify from the static pressure contour plots and become unrecognizably diffuse at a distance closer to the trailing edge than in the strong shedding case. Figure 6.13 shows all the vortex core locations that were identified for a typical weak shedding cycle. The locations of formation and general propagation paths are seen to be similar to those in the strong shedding case presented in Figure 6.8.

Figure 6.14 shows the vortex core locations at iteration 61250. The spacing ratio b/h is 2.64. This, again, is similar to the value found for

vortices in the strong shedding case (compare with Figure 6.9).

6.3 Frequency Normalization

As discussed above, the mechanism of shedding in this case is suggested to be somewhat different than in classical vortex shedding from bluff bodies at moderate Reynolds numbers. Consequently, a Strouhal number of about 0.2 based on some transverse length scale is not necessarily to be expected. A value of order 0.2 can, in fact, be obtained by using an average value for the vortex street width h as the normalizing length scale. However, since this value is not known a priori, it is of little use in predicting the approximate shedding frequency of new designs.

As has been discussed, the suction surface vortex is hypothesized to form near the trailing edge, due primarily to the single shear layer instability, from vorticity in the suction surface boundary layer which has convected downstream as a free shear layer from the suction surface separation point. This hypothesis is schematically represented in Figure 6.15. It is applicable to compressor sections in which the flow is approximately two-dimensional and in which the suction surface boundary layer separates upstream of the trailing edge while the pressure surface boundary layer remains attached until the trailing edge. If this hypothesis is correct, a likely characteristic time scale seems to be the propagation time in the separated shear layer from the suction surface separation point to the blade trailing edge. The shedding frequency normalized to this time scale should be of order 1.

The propagation speed within the shear layer will be approximately proportional to the boundary layer edge velocity at the separation point (Ue). This velocity together with the distance from the separation point to the trailing edge (L) has been used in the normalizations which follow.

As discussed earlier, the most accurate way to determine the time interval between consecutive vortices (Tp) is by observing the interval between spikes on the time-accurate convergence history plot. This is not always possible, however, for the weak shedding phase. The normalizations which follow are therefore only for shedding cycles in which the exact frequency could be determined from the convergence history.

Since the location of the separation point and the magnitude of the edge velocity at the separation point are both continuously changing in time, there is a question as to which values should be used to normalize a given shedding cycle. Consequently, two normalized frequencies have been calculated for each shedding cycle, one based on conditions at the approximate start of the shedding cycle, the other based on conditions at the approximate end of the cycle. The two values are connected by a straight line in the plots which follow. There is generally only a small difference between them.

Figure 6.16 shows the normalized frequencies calculated together with the actual frequencies observed. The normalized values are of order 1 as expected, having an average value of 1.113. However, the normalized frequency parameter is not as constant as desired. The actual frequencies have a total range of variation, defined as (maximum frequency - minimum frequency) / mean frequency, of about 53 percent. The normalized frequency parameter has a total range of variation of about 33 percent.

As an effort to improve the correlation, the boundary layer displacement thickness at the separation point (δ^*) may be included. The displacement thickness is greater when the separation point is near the trailing edge. Dimensional arguments lead to the hypothesis that $L/(Ue\ Tp) = fnct(L/\delta^*)$. The frequency parameter $L/(Ue\ Tp)$ is plotted against L/δ^* in Figure 6.17. Each rectangular region is obtained from the two values of the frequency parameter

and the two values of the displacement thickness found at the beginning and end of each shedding cycle. Unfortunately, no useful relation between the frequency parameter and L/δ^* is apparent.

It is concluded, then, that factors other than variations in the separation point location and boundary layer displacement thickness at separation are involved in the variation of the shedding frequency over the course of a low frequency cycle. These factors have not been identified, and a completely satisfactory frequency normalization has not been found. It is tentatively suggested, however, that the average shedding frequency may be of the same order as the average convection time from separation point to trailing edge in other compressors in which the flow is approximately two-dimensional and in which only the suction surface boundary layer separates. When the average separation location and separation edge velocity are known, this suggestion may be useful in predicting the general neighborhood of the shedding frequencies.

6.4 Mechanics of Vortex Strength Variation

A mechanism by which the shedding strength is varied by the low frequency cycle is suggested by again examining the movement of the separation point. Three factors may be mentioned.

First, the discussion in section 6.2 mentioned that the vortex strength continues to increase as long as the vortex is fed by vorticity from the appropriate boundary layer. If the hypothesis advanced above concerning the formation of the suction surface vortex is correct, then there is more vorticity available in the free shear layer to form a strong vortex when the separation point is far from the trailing edge. This is illustrated schematically in Figure 6.18.

Second, the average vorticity in the boundary layer at any location is determined by the edge velocity and the boundary layer thickness as illustrated in Figure 6.19. A compressor boundary layer over the last quarter chord of the blade is expected to be in a region of adverse pressure gradient and decreasing edge velocity. Thus, when the boundary layer separates far from the trailing edge (where the edge velocity is higher and the boundary layer thinner) the resulting free shear layer is expected to have more average vorticity at any location than when the boundary layer separates near the trailing edge. This also should lead to the formation of stronger vortices when the separation point is further from the trailing edge.

Third, it is observed that lower frequencies result when the separation point is far from the trailing edge. This allows more time for the pressure surface vortex to be fed by the pressure surface boundary layer thus forming a stronger vortex.

For these reasons, then, strong shedding is expected when the separation point is far from the trailing edge; weak shedding when it is near. That this is in fact the case is shown in Figure 6.20. Here the separation point location is shown together with the time varying static pressure on the blade surface at the tip of the trailing edge (for a bluff body this would be the "base pressure"). This pressure clearly shows the presence of vortex shedding, and the amplitude of its fluctuations give an indication of the shedding strength. As can be seen, phases of weaker shedding correspond to times in which the separation point is nearer the trailing edge.

CHAPTER 7 LOW FREQUENCY UNSTEADINESS

As mentioned in Chapter 5, the vortex shedding is superimposed upon a low frequency cycle of relatively large amplitude. It is important to explore whether this low frequency cycle is merely induced by the numerical scheme, or whether it is likely to be found in real transonic compressors. This is a difficult problem to solve short of attempting to measure the phenomenon in a real machine, and no truly conclusive answer can be provided here. The possibility, however, that the low frequency cycle could be due to wave reflection off the downstream computational boundary is examined in the first section of this chapter and shown to be unlikely. The second section briefly compares the present computational results with experimental data taken on the same rotor. The remainder of the chapter discusses the details of the low frequency cycle as though it represents a phenomenon observable in a real turbomachine.

7.1 Possible Frequencies from Wave Reflection Off Downstream Boundary

As discussed in Chapter 2, the flow condition imposed at the downstream boundary is spacially uniform and time-constant static pressure. This is a reflective boundary condition which does not have a physical counterpart in the real turbomachinery the program is designed to simulate. Consequently, an oscillation whose existence is due purely to wave reflection off this boundary will probably not be observed in real turbomachines.

A test which would show with a high degree of certainty whether the low frequency fluctuation is due to reflection off the downstream boundary would be

to rerun the entire calculation with a new grid identical to the present one, but extended in the downstream direction so as to locate the downstream boundary further downstream. If the frequency of the fluctuation changed significantly, then reflection from the downstream boundary would be identified as an important factor in creating the fluctuation. Unfortunately, due to the excessive computer time required, it has not been possible to perform this experiment.

What has been done is to examine the frequencies of oscillation which would be expected in the present calculation from various forms of downstream boundary wave reflection. Five basic mechanisms have been considered as possible sources of the low frequency unsteadiness. These five are various combinations of three possible disturbance transport vehicles: (1) convection through the boundary layers, (2) convection through the free stream (core flow), and (3) acoustic propagation. They are as follows (and will be referred to occasionally by the following numbers):

1. Disturbance convection from the shock to the trailing edge through the pressure surface boundary layer, free stream convection to the downstream boundary, reflection and acoustic propagation back to the shock.

2. Disturbance convection from the shock to the trailing edge through the suction surface boundary layer, free stream convection to the downstream boundary, reflection and acoustic propagation back to the shock.

3. Disturbance convection from the shock to the trailing edge through the pressure surface boundary layer, acoustic propagation to the downstream boundary, reflection and acoustic propagation back to the shock.

4. Disturbance convection from the shock to the trailing edge through the suction surface boundary layer, acoustic propagation to the downstream boundary, reflection and acoustic propagation back to the shock.

5. Acoustic propagation from the shock to the downstream boundary, reflection

and acoustic propagation back to the shock.

For each of these mechanisms an effort has been made to identify the broadest realistic range of frequencies possible. The total signal travel times depend on the following distances: (1) the distance from the shock to the trailing edge along the pressure surface, (2) the distance from the shock to the trailing edge along the suction surface, (3) the axial distance from the shock to the downstream boundary, and (4) the axial distance from the trailing edge to the downstream boundary. Minimum and maximum values for each of these distances (except the fourth which remains constant) were identified as illustrated in Figure 7.1. The sonic lines from Mach number contour plots at various times were used to determine the extreme shock locations.

The various signal speeds depend on the following quantities: (1) the boundary layer edge velocity between the shock and the trailing edge for pressure surface and suction surface boundary layers, (2) the free stream axial velocity between the shock and the trailing edge, and between the trailing edge and the downstream boundary, and (3) the static temperature (for determining the acoustic speed) between the shock and the trailing edge, and between the trailing edge and the downstream boundary. These were determined by examining flow properties along three xsi-inversion lines (numbers 5, 15, and 25) shown in Figure 7.2. Recall from section 2.1 that xsi-inversion lines are lines through grid cell centers running in the streamwise direction. For each line, the termination of the shock region was estimated, and the minimum and maximum values for the axial velocity u, the downstream acoustic speed c+u, and the upstream acoustic speed c-u were determined for the regions between the shock and the trailing edge, and between the trailing edge and the downstream boundary. For lines 5 and 25, which approximate the boundary layer edges, the extremes in the total streamwise velocity $\sqrt{u^2+v^2}$ were also found for the region between the shock and the trailing edge.

This process identified the spacial extremes in relevant velocities at a given time. The process was repeated for several times selected at various points in the largest low frequency cycle. The times selected are indicated in Figure 7.3 with the plot of airfoil moment included for reference.

The extreme values in the relevant quantities are summarized in Table 7.1. They were used to estimate the extreme frequencies possible from each of the five mechanisms listed above. The minimum boundary layer convection speed was taken to be 0.3 times the appropriate minimum edge velocity; the maximum was taken as equal to the maximum edge velocity. The minimum free stream convection speed was taken to be 0.9 times the minimum axial velocity for any of the inversion lines; the maximum was taken as equal to the maximum axial velocity.

Notice that in calculating minimum and maximum frequencies, the extreme distances and extreme transport velocities found at isolated locations and at specific times are used in the calculations as though they were constant throughout the region of the flow field of interest, and constant in time. Therefore, the minimum and maximum frequencies calculated are almost certain to be exaggerations of the actual frequency range possible. A sample calculation is presented in Table 7.2.

Figure 7.4 presents all the known frequencies of interest for the present computation. Included are the range of frequencies for the observed vortex shedding, the observed low frequency unsteadiness, frequencies corresponding to exaggerated extremes for the blade and computational domain through-flow times, and the frequency ranges described above corresponding to wave reflection off the downstream boundary.

It is observed that only for one mechanism does the maximum estimated frequency range include the frequency of interest (that of the low frequency

cycle). This is the mechanism labeled (1) corresponding to disturbance convection through the pressure surface boundary layer, free stream convection to the downstream boundary, and acoustic propagation back to the shock. All other mechanisms considered yield frequencies too high to produce the low frequency unsteadiness observed at 365 Hz. Even the mechanism just mentioned barely includes 365 Hz within its frequency range, its lowest frequency being 355 Hz. As mentioned earlier, this lower bound is likely to be unrealistically low. For example, consider Table 7.2 again which gives the details for the calculation of the bounding frequencies for this mechanism. The low frequency of 355 Hz is found by assuming that the convection velocity downstream of the trailing edge is equal to the very low value of 0.9 x 0.183. Figure 7.5 shows the velocity distribution along the entire xsi-inversion line on which this minimum was found. Clearly the minimum value is not a good average value along this inversion line. If, instead of 0.183, a minimum velocity only about ten percent larger was used (e.g. 0.200), then the lowest estimated frequency for this mechanism would be greater than the observed frequency of 365 Hz. In the judgement of the author, therefore, this mechanism is not a likely cause of the low frequency unsteadiness.

The fifth mechanism considered, that of acoustic propagation from the shock to the downstream boundary and back, deserves an additional note. This is a purely acoustic resonance, such as occurs in organ pipes, and the resonant frequency depends on the reflection conditions at both ends of the region. At the downstream boundary, the reflection is off a uniform and constant static pressure boundary and corresponds to a classical open-ended pipe. The reflection condition at a normal shock in a diverging passage has been worked out as a function of frequency and channel geometry by Culick and Rogers in [7.1] and given minor corrections by Sajben and Bogar in [7.2]. The normalized frequency on which these analyses are based involves the local speed of sound just downstream of the shock, the passage area, and the rate of change of area

at the mean shock location. For the present case, this parameter is estimated to be no greater than 0.252. For a frequency parameter in this range, [7.2] indicates that the shock acts much like a closed end to an acoustic wave. In this limiting case (that of a pipe closed at one end but open at the other) the resonant frequency is half the value calculated by adding propagation times as done above (see, for example, [7.3]). The frequency range resulting from halving the bounding frequencies calculated above for mechanism 5 are also presented in Figure 7.4. Even in this case, the lowest bounding frequency is 474 Hz, considerably greater than the observed 365 Hz.

The theory just cited (from [7.1] and [7.2]) strictly applies only to shock displacements which are linearizably small, which is not the case in the present computation. Large wave amplitudes will propagate at speeds greater than the speed of sound tending to raise the frequency range even higher. Whether any of the mechanisms considered above could exist at significantly lower frequencies due to non-linear interactions with the shock cannot be answered here.

Based on the above considerations, therefore, it is concluded that a mechanism by which the large amplitude low frequency oscillation could be produced purely by wave reflection off the downstream computational boundary is not immediately apparent. It is noteworthy, however, that the frequencies estimated for the mechanisms mentioned above are too high. Information travels fast enough to produce a frequency of 365 Hz. The specifics of how this frequency would be produced might involve complex non-linear interactions with the shock, however, and will not be speculated upon here. In absence of further analytical, computational, or experimental results, therefore, the computed unsteadiness will be treated in the remainder of this chapter as a phenomenon which might be present in real turbomachines.

7.2 Brief Comparison with Experimental Results

For reasons described in section 3.2, the hypothetical operating conditions for the present computation do not directly correspond to any available data for this compressor rotor. In particular, the extensive high frequency response data taken by Gertz in [3.2] corresponds to a higher blade relative Mach number than for the present computation. In fact, for the operating conditions Gertz measured, a bow shock should be present at the blade section simulated in the present work (see section 3.2). Nevertheless, there is qualitative agreement between the present computational results and the data reported in [3.2] as Figure 7.6 shows. The upper curve has been obtained by translating into the blade relative frame measurements taken by Gertz using a stationary probe downstream of the rotor. The lower curve is a simulation of what such a stationary probe would see if sampling the flow computed by ANSI2D. The significant variations in the total pressure defect blade to blade are due to the probe passing through the shed vortex street as discussed in [3.2]. Note that in either curve the presence of the low frequency oscillation is not obvious to the eye. The period of the computed low frequency cycle has been indicated on the figure.

Spectral analyses of Gertz's data show some frequency content below 1 KHz, but this is inadequate to either prove or disprove the existence of the type of low frequency oscillation observed in the computational results.

7.3 Nature of the Oscillation

The various events observed over one cycle of the low frequency unsteadiness will be presented in this section as stemming from the movement of the shock wave. It should be remembered, however, that when observing a

sequence of interrelated events, the separation of cause from effect is usually difficult and sometimes ambiguous. For example, when a shock is observed to move in a diverging channel, a change of pressure downstream of the shock is also observed to occur. Since the two events always occur together, it is pointless to debate over whether the shock's movement is to be thought of as causing the pressure change, or vice versa. Similarly, in the discussion which follows, the shock's movement will be taken as a convenient starting point in describing the other related events in the low frequency cycle. This does not necessarily imply, however, that the shock movement is best viewed as the cause of the other events.

The reduced frequency of the low frequency cycle (normalized by the blade through-flow time) is about 0.1. Even using the exaggerated bounds for blade through-flow time presented in Figure 7.4, the reduced frequency is no greater than 0.18. A reduced frequency of 0.1 means that one low frequency cycle takes place over about ten through-flow times. Such a low reduced frequency means that a quasi-steady analysis may be employed to a good approximation. This is the type of analysis presented in the remainder of this chapter.

Figure 7.7 presents the time varying maximum Mach numbers along three xsi-inversion lines. These are the same lines drawn in Figure 7.2, line 5 being near the suction surface, line 15 at mid-passage, and line 25 near the pressure surface. These maximum Mach numbers are not necessarily equal to the actual pre-shock Mach numbers (see section 4.2.1) but are, nevertheless, an indication of relative shock strength. It is observed that, except for a single brief period of time, the shock monotonically decreases in strength from the suction surface to the pressure surface. The shock strength also varies with time at all three cross-passage locations. The variation in shock strength is relatively large near the suction surface and at mid-passage, and the variations at these two locations are in phase with each other. The variation near the

pressure surface is relatively small and more complex, appearing at later times to be nearly 180 degrees out of phase with the variations at the other locations.

The variations in maximum Mach number with time indicate movement of the shock. Since the shock exists in a diverging channel, an increase in maximum Mach number indicates a downstream displacement of the shock. Figure 7.8 shows the extremes in the sonic line location. The total displacement of the shock shown in Figure 7.8 is a distance of about 0.05 blade chords, and 0.15 passage widths.

It is to be observed at this point that movement of the shock is evident only at the low frequency and not at the high frequencies of the vortex shedding. This does not, however, necessarily preclude the possibility of high frequency shock movement the presence of which has been suggested by Ng in [1.2]. The shock displacements hypothesized by Ng are of the same order or smaller than the grid spacing used in the present computation and may therefore be expected to be obliterated by the computation. More information on the existence and character of high frequency shock motion must await another investigation.

Figure 7.8 also shows the extremes in suction surface separation point location. The total displacement is about 0.12 blade chords. Figure 7.9 shows the time varying separation point location relative to the maximum Mach number variation near the suction surface. It is observed that the separation point moves upstream when the shock foot near the suction surface moves downstream (though the shock movement and separation point movement are not exactly 180 degrees out of phase). This substantiates the assertion made in section 4.2.2 that the separation is not properly termed "shock induced," i.e. it does not always occur at the shock location. (The separation occurs approximately at the

shock location only when the separation point is in its most extreme excursion upstream during the first cycle of the low frequency fluctuation.) The shock, however, definitely has a strong effect on the separation location. When the shock is displaced downstream its strength is greater meaning that there is a greater pressure rise across the shock. This provides a greater adverse effect on the boundary layer promoting earlier separation (movement of the separation location upstream).

The movement of the separation point affects the amount of vorticity shed into the wake. The flux of vorticity leaving the airfoil and entering the wake is found by examining the boundary layer at the separation point. This is discussed by Sears in [7.4] and is illustrated in Figure 7.10 where u_e is the boundary layer edge velocity and u_{sep} is the velocity of the separation location, both measured in the blade's frame of reference.

Figure 7.11 shows the time varying vorticity flux from each surface (both plotted as positive values). The pressure surface boundary layer remains attached until the trailing edge; consequently the flux has been calculated at an arbitrary fixed point about one boundary layer thickness upstream of the trailing edge (a location where the boundary layer approximation on which the formula for vorticity flux is based is still good). The time averages of the vorticity fluxes from the suction and pressure surfaces are found to be unequal using this method. Therefore a constant has been added to the pressure surface flux to make the time average of the difference between the suction surface flux and the pressure surface flux equal to zero.

Figure 7.12 shows the suction surface separation point velocity u_{sep} together with the total suction surface vorticity flux. The movement of the suction surface separation point is the primary cause of the significant variations in suction surface vorticity flux. The pressure surface vorticity

flux is evaluated at a fixed point ($u_{sep} = 0$) and the variations in pressure surface vorticity flux are much smaller than for the suction surface.

As described in [7.4], the vorticity flux from each surface can be subtracted from each other to yield the net vorticity shed into the wake. By Kelvin's theorem this must be the opposite of the instantaneous rate of change of circulation about the airfoil. The airfoil circulation calculated in this way (defined as positive clockwise and arbitrarily having value zero at time zero) is plotted in Figure 7.13 together with the airfoil lift found by integrating surface pressures. In analogy with isolated airfoils, an increasing clockwise circulation should produce increasing lift. Although the airfoil here is not isolated (there are cascade effects, wake effects, and the recirculation region beneath the separated suction surface boundary layer to consider) the lift nevertheless follows the general trend expected. The lift is not exactly proportional to the circulation, however, and seems to lead it in phase slightly.

7.4 Summary

In summary, the low frequency cycle may be viewed as a quasi-steady sequence of events stemming from movement of the shock. When the shock displaces downstream it becomes stronger promoting earlier boundary layer separation. The upstream movement of the separation point gives rise to strong shedding and lower shedding frequencies (as described in Chapter 6). The upstream movement of the separation point also produces a larger flux of suction surface vorticity into the wake. By Kelvin's theorem this must mean a change in the airfoil circulation such as to tend to decrease the airfoil lift thus decreasing the instantaneous work done by the blade. When the system limit is reached and the shock moves upstream again, the above sequence of events

reverses to complete the cycle.

The factors determining the frequency of the cycle are unknown to the author at present. They are similar in many respects to phenomena observed in transonic diffusers (see [7.5] and papers referenced there). The frequencies observed in transonic diffusers are thought to be determined by wave reflection off a uniform static pressure boundary (which exists physically in diffuser experiments) or off the merging point of the sidewall boundary layers (see [7.5]). A computational simulation of transonic inlet flows using an algorithm similar in many respects to ANSI2D has predicted oscillations closely resembling those observed experimentally, but with the frequency depending on the placement of the downstream boundary (see [7.6]). Nevertheless, no mechanism of wave reflection has been identified by the present author which readily accounts for the frequency observed in the compressor simulation presented above.

Finally, the damping of the low frequency cycle is hypothesized to be due primarily to the numerical smoothing used to stabilize the numerical algorithm. The testing of this hypothesis must await other time-accurate codes using different smoothing strategies, or the documentation of similar oscillations in real transonic rotors.

CHAPTER 8 CONCLUSIONS AND SUGGESTIONS FOR FURTHER STUDY

8.1 Conclusions

A summary of the principal conclusions drawn from the work presented above is as follows:

A numerical simulation of the flow about a two-dimensional section from a transonic compressor rotor (the flow upstream of which is steady) does predict significant blade-relative flow unsteadiness.

The simulation predicts vortex shedding to exist at frequencies ranging from 11 KHz to 19 KHz.

These frequencies are in the range expected from experiments performed on the actual compressor rotor simulated here.

The geometry of the vortex street bears similarity to the classical Karman vortex street.

It is suggested, nevertheless, that the physics giving rise to the formation of the vortex street are somewhat different than those giving rise to classical Karman vortex streets. Specifically, it is suggested that the street arises primarily due to the single shear layer instability rather than the twin shear layer instability.

The average time interval between adjacent vortices (average period) is of the same order as the average convection time in the free shear layer from separation point to trailing edge. It is suggested that this may be true in general for compressor sections in which the flow is approximately two-dimensional and only the suction surface boundary layer separates.

A low frequency cycle was also observed in the computation. It occurs at a

frequency of about 365 Hz.

The low frequency cycle produces variations in blade force and moment large enough to be important structurally.

The low frequency cycle is described as a quasi-steady sequence of events related to movement of the shock and involving movement of the suction surface separation point and changes in vorticity flux from the blade boundary layers.

The frequency and strength of the vortex shedding are modulated by the low frequency cycle.

It is suggested that the variations in both shedding frequency and strength are related to movements of the suction surface separation point. This factor alone, however, fails to fully account for the frequency variation observed.

Several mechanisms involving wave reflection off the downstream boundary were considered as possible numerical causes of the low frequency cycle, but none of them appear to be likely causes. The low frequency cycle is thus regarded as corresponding to a real flow phenomenon observable in real turbomachinery.

8.2 Suggestions for Further Study

All of the results presented above were obtained with a single algorithm and a single computational grid. More refined grids should be used with the same algorithm to test the dependence of the results on grid resolution. It is hoped as well that the case studied here will again be studied with other (hopefully faster) time-accurate algorithms as they become available.

Cases should be studied in which the downstream boundary is located at different distances from the trailing edge. The frequency and character of the low frequency cycle should be observed to see the effects of boundary position.

In addition, since the upstream flow is not axially supersonic, any possible effects of the upstream boundary placement should be considered.

Tools to predict the frequency and amplitude of the low frequency cycle should be developed. In this regard, consideration should be given to ways in which the cycle could be driven or damped by factors in the turbomachinery environment such as rotor-stator interactions, duct resonant modes, upstream flow non-uniformities, three-dimensional effects, and aeroelasticity.

The implications of the low frequency cycle on the time-averaged performance and structural integrity of real turbomachinery should be studied. Designers of turbomachinery should be alerted to these implications and to ways in which the character and frequency of the low frequency cycle may be modified to best suit new designs.

Finally, further insight is needed to more accurately predict the frequency of vortex shedding in turbomachines.

REFERENCES

Chapter 1

1.1 Ng, W., "Detailed Time Resolved Measurements and Analysis of Unsteady Flow in a Transonic Compressor," Gas Turbine Plasma Dynamics Laboratory Report Number 150, Massachusetts Institute of Technology, Cambridge, Massachusetts, 1980.

1.2 Ng, W., "Time-Resolved Stagnation Temperature Measurement in a Transonic Compressor Stage," Gas Turbine Plasma Dynamics Laboratory Report Number 177, Massachusetts Institute of Technology, Cambridge, Massachusetts, 1983.

1.3 Gertz, J.B., "Unsteady Design-Point Flow Phenomena in Transonic Compressors," Ph.D. Thesis, Massachusetts Institute of Technology, Cambridge, Massachusetts, 1985.

1.4 Scott, J.N., "Numerical Simulation of Unsteady Flow in a Compressor Rotor Cascade," AIAA Paper Number 85-0133, 1985.

1.5 Scott, J.N., Hankey, W.L., Jr., "Boundary Conditions for Navier-Stokes Solutions of Unsteady Flow in a Compressor Rotor," in Three Dimensional Flow Phenomena in Fluid Machinery, presented at the Winter Annual Meeting of the American Society of Mechanical Engineers, Miami Beach, Florida, November 17-22, 1985.

Chapter 2

2.1 Norton, R.J.G., Thompkins, W.T. Jr., Haimes, R., "Implicit Finite Difference Schemes with Non-Simply Connected Grids—A Novel Approach," AIAA-84-0003, 1984.

2.2 Giles, M., "ANSI-2D; An Explicit Method for Solving the Steady-State Navier-Stokes Equations", internal report, Massachusetts Institute of Technology, Cambridge, Massachusetts, 1986.

2.3 Ferri, A., "Aerodynamic Properties of Supersonic Compressors", in High Speed Aerodynamics and Jet Propulsion, Volume X: Aerodynamics of Turbines and Compressors, Hawthorne, W.R., ed., Princeton, 1964.

2.4 Bradshaw, P., Cebeci, T., and Whitelaw, J.H., Engineering Calculation Methods for Turbulent Flow, pp. 43-44, Academic Press, 1981.

Chapter 3

3.1 Urasek, D.C., Gorrell, W.T., Cunnan, W.S., "Performance of Two-Stage Fan Having Low-Aspect-Ratio, First-Stage Rotor Blading," NASA Technical Paper 1493, 1979.

3.2 Gertz, J.B., "Unsteady Design-Point Flow Phenomena in Transonic Compressors," Ph.D. Thesis, Massachusetts Institute of Technology, Cambridge, Massachusetts, 1985.

Chapter 6

6.1 Fage, A., Johansen, F.C., "On the Flow of Air Behind an Inclined Flat Plate of Infinite Span," Procedings of the Royal Society, Series A, V. 116, 1927.

6.2 Roshko, A., "On the Drag and Shedding Frequency of Two-Dimensional Bluff Bodies," National Advisory Committee for Aeronautics (NACA) Technical Note 3169, 1953.

6.3 Abernathy, F.H., Kronauer, R.E., "The Formation of Vortex Streets," Journal of Fluid Mechanics, V. 13, 1962.

6.4 Van Dyke, M., An Album of Fluid Motion, Parabolic Press, Stanford, California, 1982.

6.5 Morkovin, M.V., "Flow Around Circular Cylinder—A Kaleidoscope of Challenging Fluid Phenonena," in ASME Fluids Engineering Division Conference: Symposium on Fully Separated Flows, Philadelphia, Pennsylvania, May 18-20, 1964.

6.6 Batchelor, G.K., An Introduction to Fluid Dynamics, Cambridge University Press, 1967.

Chapter 7

7.1 Culick, F.E.C., Rogers, T., "The Response of Normal Shocks in Diffusers," AIAA Journal, V. 21, no. 10, 1983.

7.2 Sajben, M., Bogar, T.J., "Unsteady Transonic Flow in a Two-Dimensional Diffuser: Interpretation of Experimental Results," Scientific Report for 1 April 1981 - 31 March 1982 for Air Force Office of Scientific Research contract F49620-77-C-0082, Report Number MDC Q0779.

7.3 Lamb, H., The Dynamical Theory of Sound, Second Edition, Dover Publications, New York, New York, 1925.

7.4 Sears, W.R., "Unsteady Motion of Airfoils with Boundary-Layer Separation," AIAA Journal, V. 14, No. 2, 1976.

7.5 Bogar, T.J., Sajben, M., Kroutil, J.C., "Characteristic Frequency and Length Scales in Transonic Diffuser Flow Oscillations," AIAA-81-1291, presented at AIAA 14th Fluid and Plasma Dynamics Conference, June 23-25, Palo Alto, California, 1981.

7.6 Liou, M.S., Coakley, T.J., "Numerical Simulations of Unsteady Transonic Flow in Diffusers," AIAA-82-1000, presented at AIAA/ASME 3rd Joint Thermophysics, Fluids, Plasma and Heat Transfer Conference, June 7-11, St. Louis, Missouri, 1982.

TABLES

TABLE 3.1
SUMMARY OF NASA ROTOR 67 SECTION 5
TWO-DIMENSIONAL MEANLINE GEOMETRY

All lengths are centimeters.
All angles are degrees.

MEANLINE GEOMETRY

Inlet Radius, R1 = 19.81
Exit Radius, RO = 19.59
Mean Radius, RM = 19.70

Cone Angle = -2.073

Inlet Point: XI = 0.0, YI = 0.0
Axial Leading Edge, XAXLE = -0.01133
Leading Edge Radius, RLE = 0.02504
Centered at XCI = 0.01371, YCI = 0.02095
Inlet Angle = 56.810

Upstream Meanline Arc Radius, R1 = 43.53
Centered at X1 = 36.43, Y1 = -23.83

Curvature Transition Point: XTC = 2.668, YTC = 3.650
TRANS = (XTC-XI)/(XO-XI) = 0.4498
Angle at Curvature Transition, THT = 50.858

Downstream Meanline Arc Radius, R2 = 36.05
Centered at X2 = 30.62, Y2 = -19.10

Meanline Arc Ratio, R1/R2 = 1.208

Exit Angle, THO = 43.240
Exit Point: XO = 5.931, YO = 7.155
Axial Trailing Edge, XAXTE = 5.938
Trailing Edge Radius, RTE = 0.02666
Centered at XCO = 5.911, YCO = 7.137

Setting Angle = 50.343
True Chord = 9.293
Axial Chord = 5.931

TABLE 3.1 (CONT.)

THICKNESS DISTRIBUTION

Inlet Thickness, TI = 0.05
at XRI = 0.01296, YT1 = 0.01981

Max Thickness, TM = 0.4234
AT XTM = 3.272, YTM = 4.373

THKX = (XTM-XI)/(XO-XI) = 0.5517

Exit Thickness, TO = 0.053
at XTO = 5.914, YTO = 7.139

$T(x) = C1 + C2\,x + C3\,x + C4\,x + C5\,x + C6\,x$
where C1 = 0.04741
C2 = 0.2002
C3 = -0.01764
C4 = -0.2448E-2
C5 = -0.4074E-4
C6 = -0.7545E-6

NUMBER OF BLADES = 22

TABLE 3.2 HYPOTHETICAL OPERATING CONDITIONS

NASA ROTOR 67, SECTION 5, ZERO INCIDENCE, PDS=0.51

GAM=1.4000 RGAS= 1716.58 L=0.194600

R1=0.646300 R2=0.646300

	INLET		EXIT	
	ABSOLUTE	RELATIVE	ABSOLUTE	RELATIVE
PT	15.056	21.192	19.447	20.556
TT	510.00	562.32	553.48	562.32
RHOT	2.4766E-03	3.1615E-03	2.9475E-03	3.0666E-03
MUT	3.6888E-07	3.9773E-07	3.9295E-07	3.9773E-07
"RET"	1.4464E+06	1.7982E+06	1.6835E+06	1.7442E+06
PS	12.213		15.131	
TS	480.40		515.19	
RHOS	2.1327E-03		2.4638E-03	
MUS	3.5193E-07		3.7180E-07	
RE	7.0333E+05	1.1701E+06	8.7477E+05	9.7050E+05
MZ	0.5055		0.4225	
MTH	0.2293	0.7728	0.4395	0.5281
M	0.5551	0.9234	0.6096	0.6764
ANGLE	24.399	56.810	46.126	51.340
VZ	5.4314E+02		4.7014E+02	
VTH	2.4636E+02	8.3030E+02	4.8900E+02	5.8767E+02
V	5.9640E+02	9.9217E+02	6.7835E+02	7.5259E+02
U	1.0767E+03		1.0767E+03	
RPM	1.5908E+04			
RPMC	1.6043E+04			
%SPEED	100.00			
MDOT/A	1.1584			

PTA2/PTA1 = 1.2916

PTR2/PTR1 = 0.9700

TTA2/TTA1 = 1.0853

PS2/PS1 = 1.2389

PS2/PTA1 = 1.0050

PS2/PTR1 = 0.7140

PDS = 0.5100

TABLE 4.1
MACH NUMBERS AT CELLS ALONG XSI-INVERSION LINE 15
STEADY STATE ITERATION 2500

Cell Number	Mach Number
53	1.207
54	1.204
55	1.164
56	1.093
57	1.008
58	0.935
59	0.886
60	0.860
61	0.849
62	0.842
63	0.833
64	0.823
65	0.816

Maximum Mach number along this inversion line

TABLE 4.2
EXTENT OF SHOCK SMEARING BASED ON
DIFFERENT SHOCK START LOCATIONS

Cell Number at Shock Start	Cell Number at Shock Termination	RMS Error
53	64	1.03%
54	63	1.04%
55	60	0.84%
56	58	8.35%

TABLE 4.3
OVERALL BLADE PERFORMANCE AVERAGED 1.6 TRAILING EDGE DIAMETERS DOWNSTREAM OF BLADE TRAILING EDGE
STEADY STATE ITERATION 2500

	Mass Averaged		Stream Thrust Averaged *	
	Abs	Rel	Abs	Rel
Total Pressure Ratio	1.292	0.977	1.280	0.970
Total Temperature Ratio	1.082	0.999	1.081	0.999
Static Pressure Ratio	0.978	0.695	1.000	0.711
Static Temperature Ratio	0.999	0.906	1.008	0.914
Flow Angle	42.86	48.59	45.84	51.84
Mach Number	0.644	0.714	0.604	0.681
Adiabatic Efficiency	92.8%		90.1%	

* Constant area duct

TABLE 5.1

		MIN	MAX	TIME AVE	STEADY STATE ITER 2500
Lift Coeff.		0.381	0.401	0.396	0.366
Drag Coeff.		0.0348	0.0397	0.0371	0.0364
Moment Coeff.		0.100	0.136	0.114	0.120
MASS AVERAGED VALUES					
Pt ratio,	abs	1.285	1.313	1.299	1.292
	rel	0.975	0.984	0.978	0.977
Tt ratio,	abs	1.083	1.091	1.086	1.082
Flow Angle,	abs	42.35	44.31	43.75	42.86
	rel	47.81	49.44	48.80	48.59
Mach Nr.,	abs	0.632	0.652	0.640	0.644
	rel	0.696	0.718	0.702	0.714
Adiabatic Eff.		89.1%	92.0%	90.6%	92.8%
STREAM THRUST AVERAGED VALUES					
Pt ratio,	abs	1.284	1.296	1.292	1.280
	rel	0.966	0.975	0.971	0.970
Tt ratio,	abs	1.076	1.090	1.086	1.081
Flow Angle,	abs	45.78	46.42	46.13	45.84
	rel	51.11	51.92	51.38	51.84
Mach Nr.,	abs	0.604	0.613	0.609	0.604
	rel	0.673	0.684	0.676	0.681
Adiabatic Eff.		85.2%	97.6%	88.6%	90.1%

TABLE 5.2

		TIME AVE	TOTAL VARIATION	DIFF. FROM TIME AVE STEADY STATE ITER 2500
Lift Coeff.		0.396	5.1%	-7.6%
Drag Coeff.		0.0371	13.2%	-1.9%
Moment Coeff.		0.114	31.6%	+5.3%
MASS AVERAGED VALUES				
Pt ratio,	abs	1.299	2.2%	-0.5%
	rel	0.978	0.9%	-0.1%
Tt ratio,	abs	1.086	0.7%	-0.4%
Flow Angle,	abs	43.75	Δ=1.96	Δ=-0.9
	rel	48.80	Δ=1.63	Δ=-0.2
Mach Nr.,	abs	0.640	3.1%	+0.6%
	rel	0.702	3.1%	+1.7%
Adiabatic Eff.		90.6%	Δ=2.9%	Δ=+2.2%
STREAM THRUST AVERAGED VALUES				
Pt ratio,	abs	1.292	0.9%	-0.9%
	rel	0.971	0.9%	-0.1%
Tt ratio,	abs	1.086	1.3%	-0.5%
Flow Angle,	abs	46.13	Δ=0.6	Δ=-0.3
	rel	51.38	Δ=0.8	Δ=+0.5
Mach Nr.,	abs	0.609	1.5%	-0.8%
	rel	0.676	1.6%	+0.7%
Adiabatic Eff.		88.6%	Δ=12.4%	Δ=+1.5%

TABLE 5.3
SENSITIVITY OF ADIABATIC EFFICIENCY TO SMALL CHANGES IN TOTAL PRESSURE AND TOTAL TEMPERATURE RATIOS

Let Pt be the total pressure ratio;
Tt the total temperature ratio;
η the adiabatic efficiency (based on $\gamma = 1.4$).

Baseline: Pt = 1.295
Tt = 1.085
η = 90.2%

Case 1: Increase Pt by one significant digit (0.08 percent)
Pt = 1.296
Tt = 1.085
η = 90.5% (Δ = 0.3)

Case 2: Decrease Tt by one significant digit (0.09 percent)
Pt = 1.295
Tt = 1.084
η = 91.3% (Δ = 1.1)

Case 3: Both changes in Pt and Tt together
Pt = 1.296
Tt = 1.084
η = 91.5% (Δ = 1.3)

TABLE 6.1
SAMPLE OF APPROXIMATE VORTEX CORE PRESSURES

STRONG SHEDDING

	Near TE				Far from TE	
Iter	PS	SS	PS	SS	PS	SS
42000			?	0.468	0.461	0.501
42250			0.456	0.444	0.481	0.505
42500			0.433	0.477	0.497	-
42750			0.431	0.484	0.505	
43000			0.439	0.492	0.510	
43250	?	0.470	0.457	0.500	-	
43500	?	0.472	0.478	0.504		

WEAK SHEDDING

	Near TE				Far from TE	
Iter	PS	SS	PS	SS	PS	SS
61000			?	0.499	0.498	?
61250			0.494	0.500	0.501	-
61500		0.498	0.494	0.501	-	
61750	?	0.499	0.496	0.503		
62000	0.494	0.500	0.499	-		

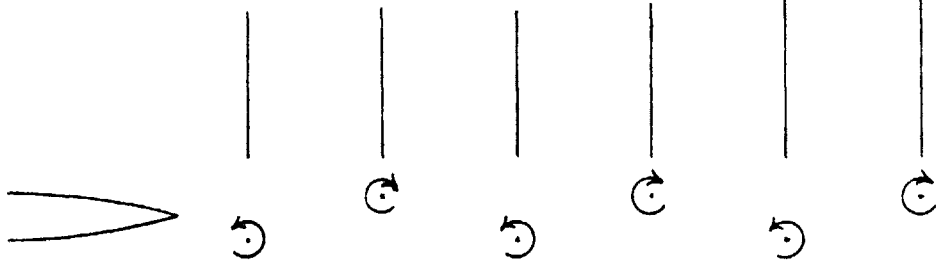

TABLE 7.1
DISTANCES AND VELOCITIES USED IN ESTIMATING
EXTREME FREQUENCIES DUE TO WAVE REFLECTION
OFF THE DOWNSTREAM COMPUTATIONAL BOUNDARY

DISTANCES (Normalized to Axial Chord)	MIN	MAX
Shock to Trailing Edge (S.S.)	0.424	0.493
Shock to Trailing Edge (P.S.)	1.15	1.23
Shock to Boundary (Axial Distance)	1.32	1.79

VELOCITIES (Normalized to Upstream Stag. Speed of Sound)	MIN	MAX
$\sqrt{u^2+v^2}$, Shock to T.E., xsi-inv 5	0.510	0.825
xsi-inv 25	0.684	0.733
u, Shock to Trailing Edge	0.337	0.558
Trailing Edge to Boundary	0.183	0.452
c+u, Shock to Trailing Edge	1.32	1.49
Trailing Edge to Boundary	1.18	1.40
c-u, Shock to Trailing Edge	0.374	0.644
Trailing Edge to Boundary	0.496	0.811

TABLE 7.2
SAMPLE CALCULATION OF EXTREME FREQUENCIES DUE TO WAVE REFLECTION OFF OF DOWNSTREAM BOUNDARY

	DISTANCE	VELOCITY
Boundary layer convection, shock to t.e. along p.s.	D1	V1
Free stream convection, shock to downstream boundary	D2	V2
Acoustic propagation, downstream boundary to shock	D3	V3

LONGEST PERIOD:

D1 = Max. p.s. value = 1.23
V1 = 0.3 x min. xsi-inv 25 value
= 0.3 x 0.684 = 0.205

D2 = 1.00
V2 = 0.9 x min. t.e. to boundary value
= 0.9 x 0.183 = 0.165

D3 = max. distance = 1.79
V3 = min. c-u = 0.374

D1/V1 + D2/V2 + D3/V3 = 6.00 + 6.06 + 4.79
= 16.85
=› 2.82 msec =› 355 Hz

SHORTEST PERIOD:

D1 = min p.s. value = 1.15
V1 = max xsi-inv 25 value = 0.733

D2 = 1.00
V2 = max t.e. to boundary value
= 0.452

D3 = min distance = 1.32
V3 = max c-u = 0.811

D1/V1 + D2/V2 + D3/V3 = 1.57 + 2.21 + 1.63
= 5.41
=› 9.06 msec =› 1100 Hz

FIGURES

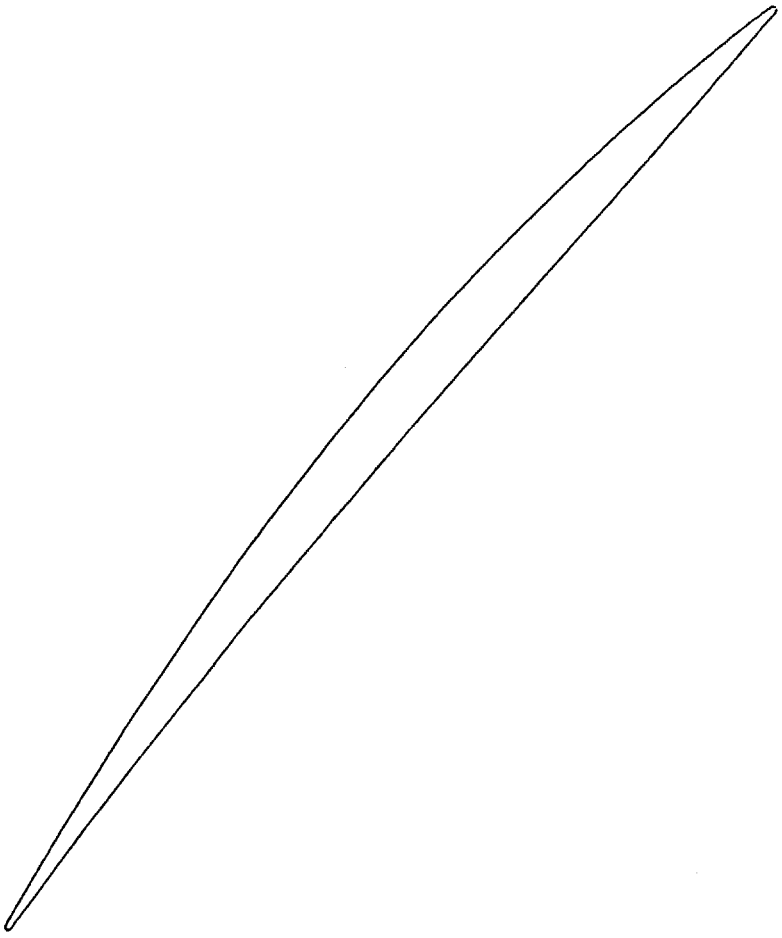

Figure 3.1 NASA Rotor 67 Section 5 Blade Shape

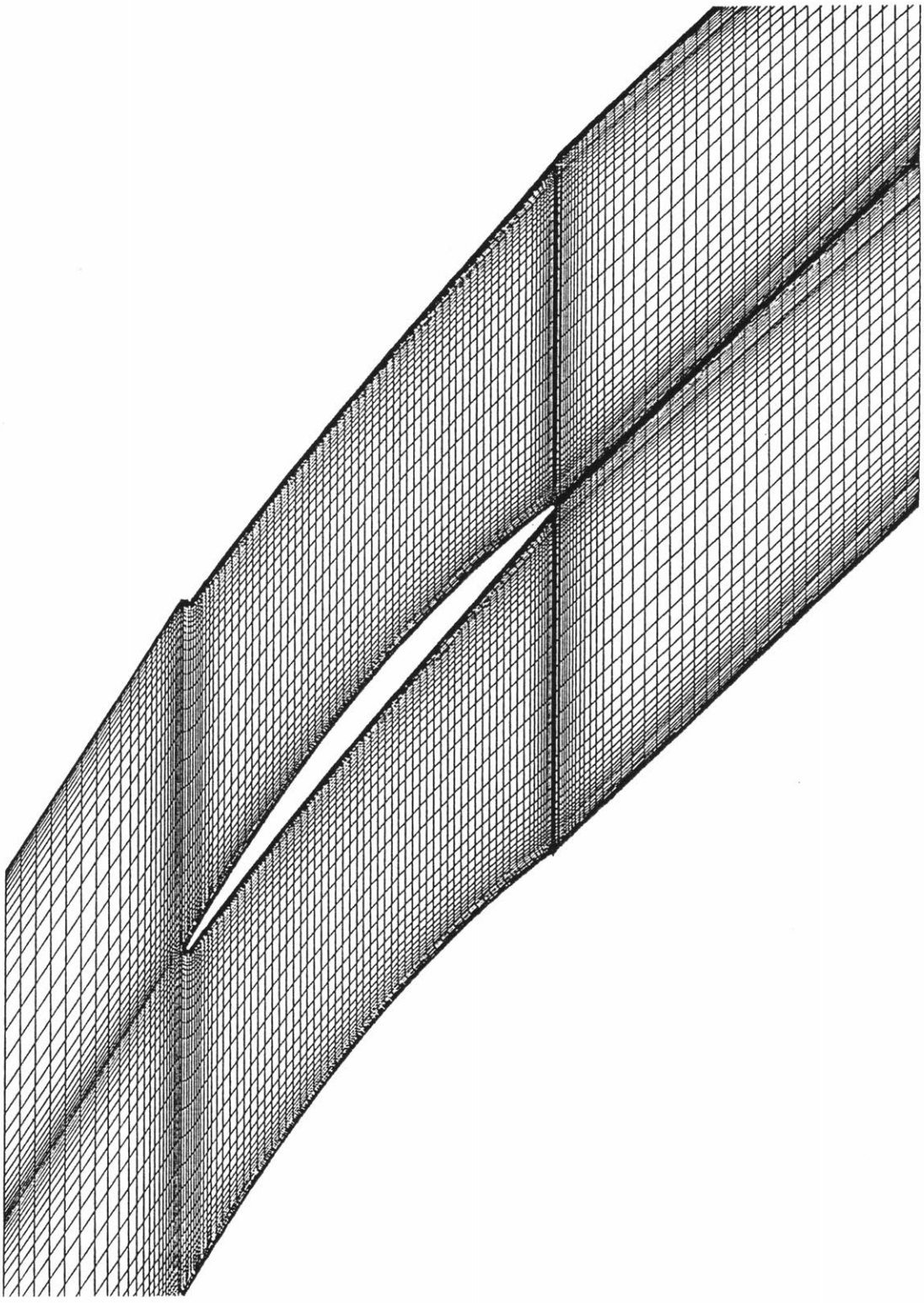

Figure 3.2 Pass 45 Grid

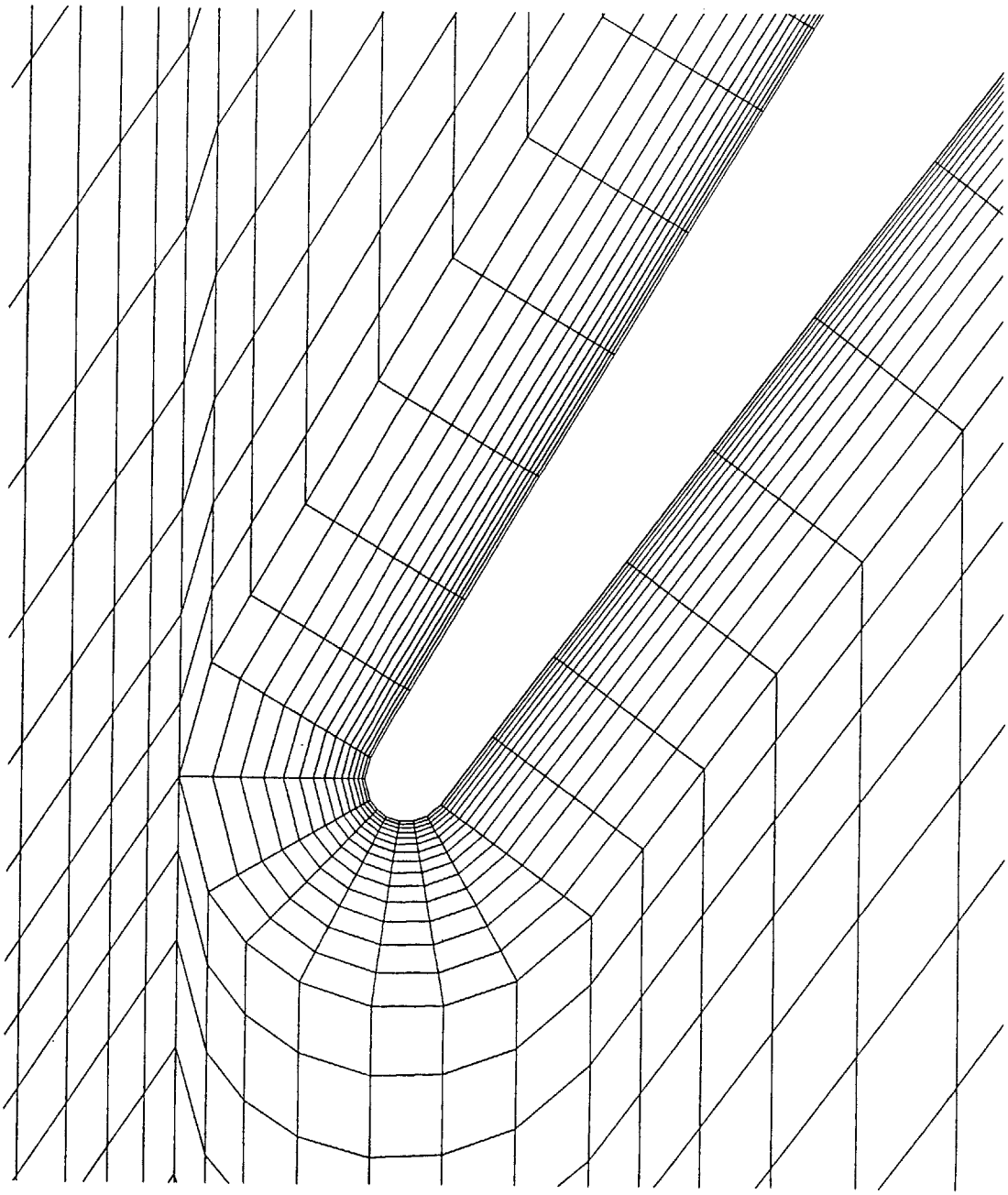

Figure 3.3 Pass 45 Grid, Leading Edge Detail

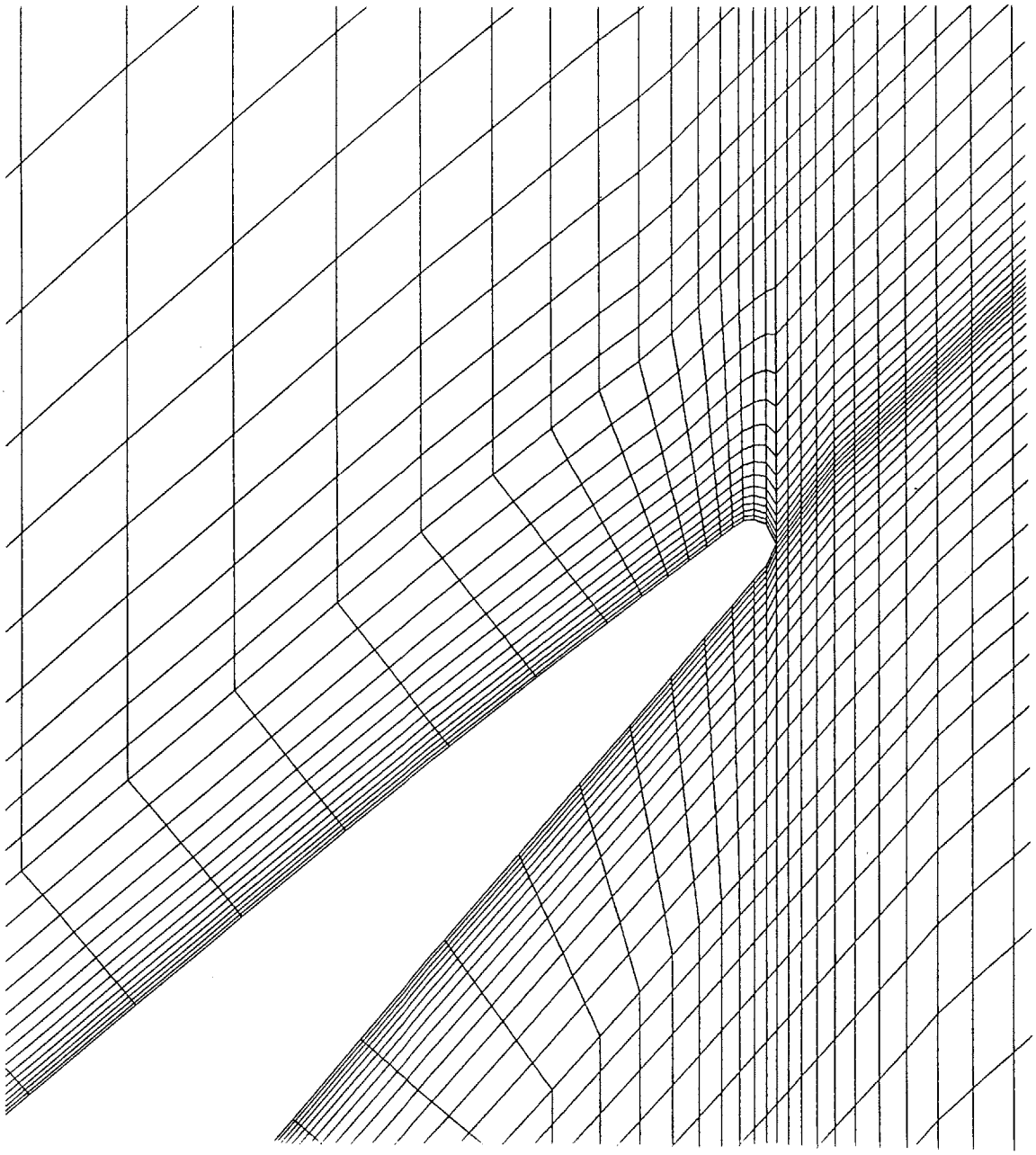

Figure 3.4 Pass 45 Grid, Trailing Edge Detail

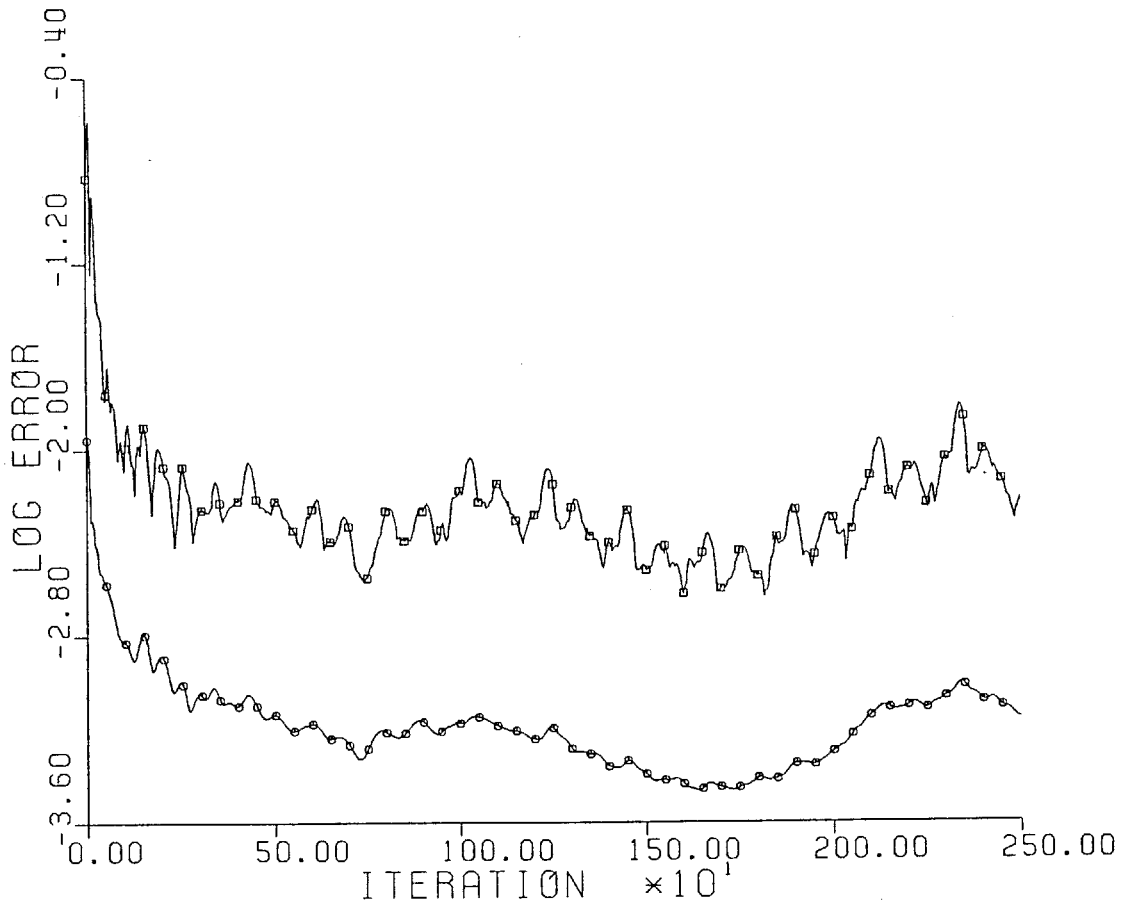

Figure 4.1 Steady State Convergence History

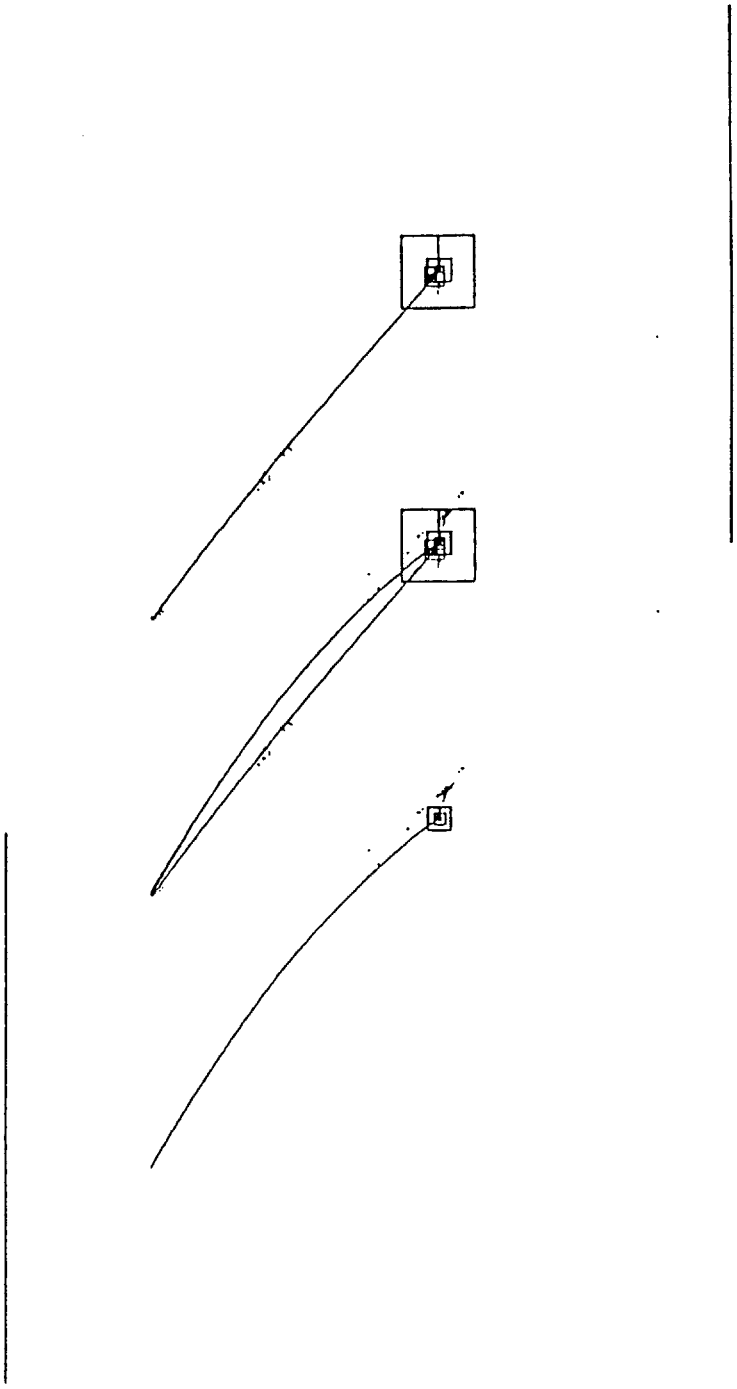

Figure 4.2 Steady State Error Locations

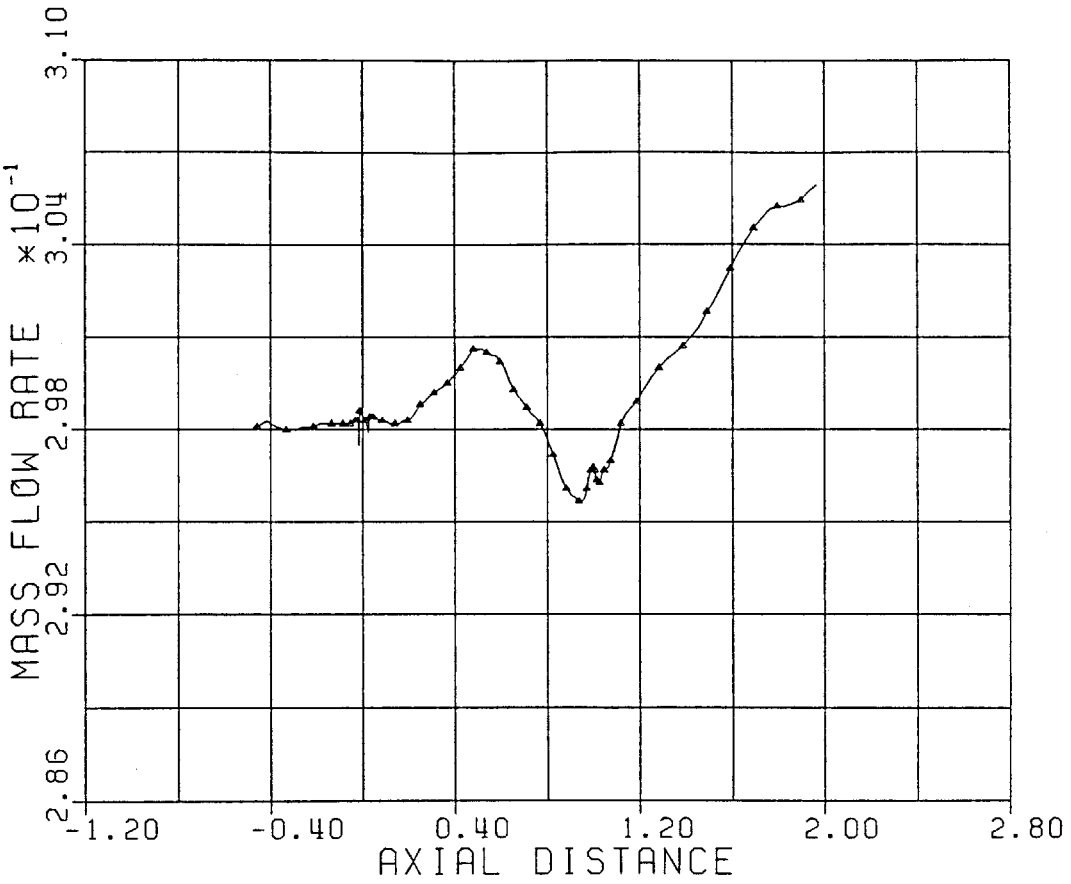

Figure 4.3 Mass Flow Variation, Steady State Iteration 2500

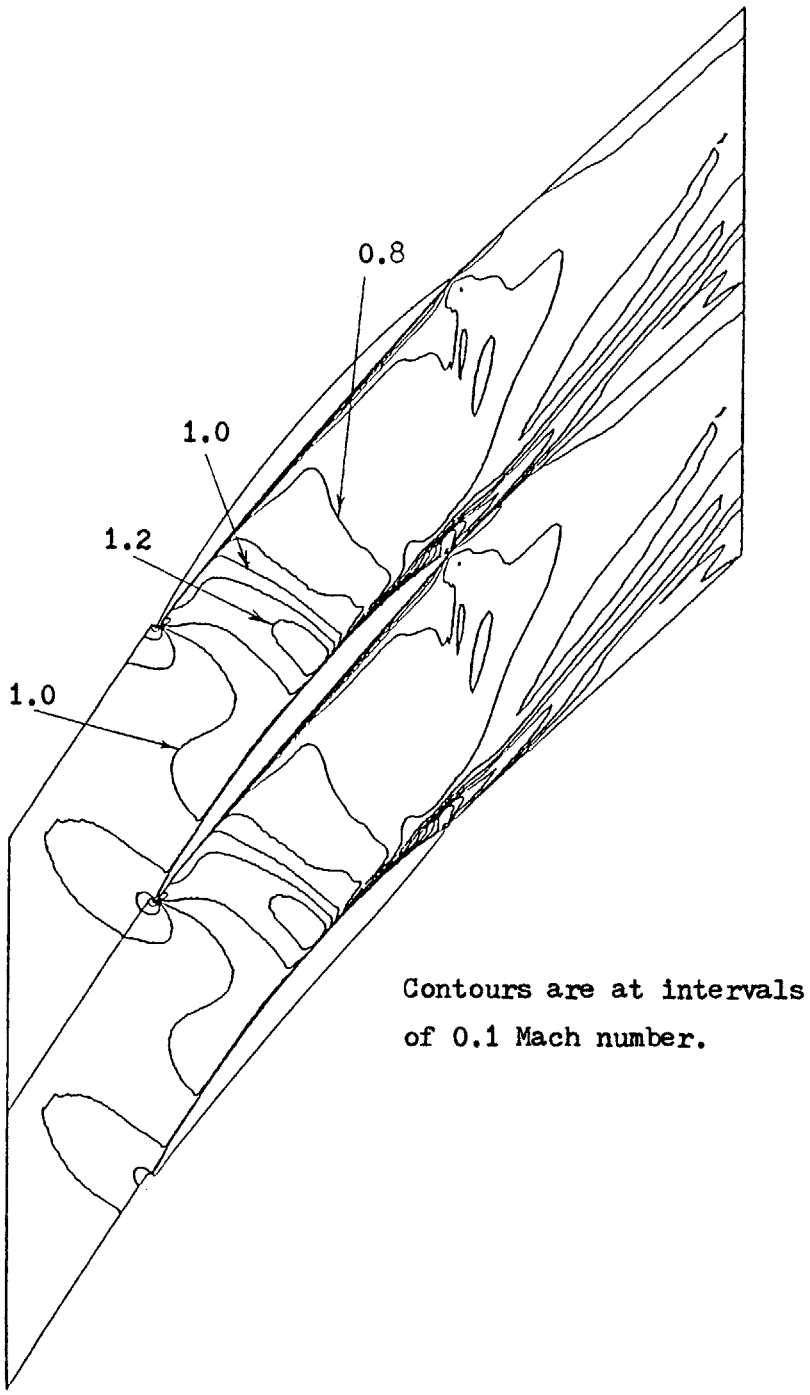

Figure 4.4 Mach Number Contours, Steady State Iteration 2500

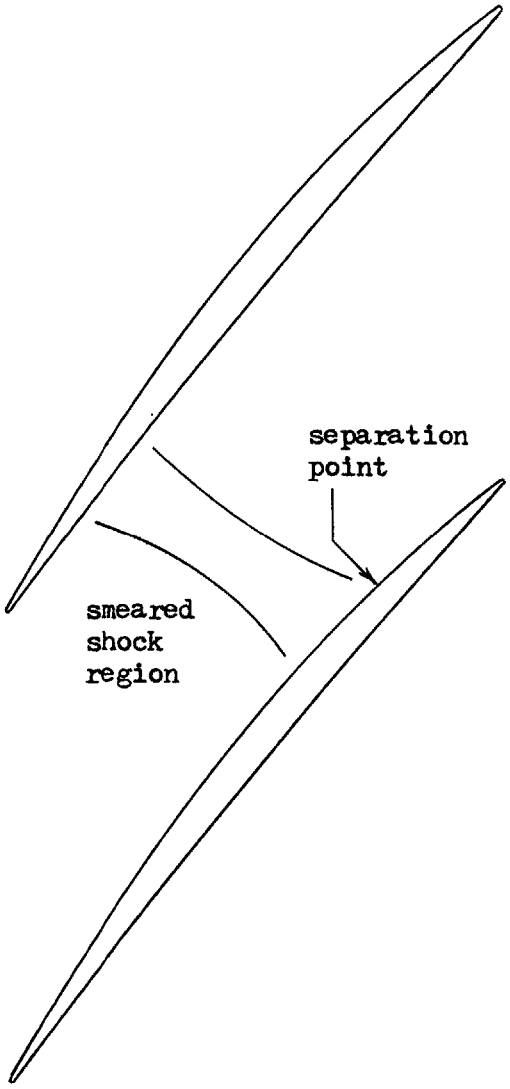

Figure 4.5 Steady State Shock and Boundary Layer Separation Locations

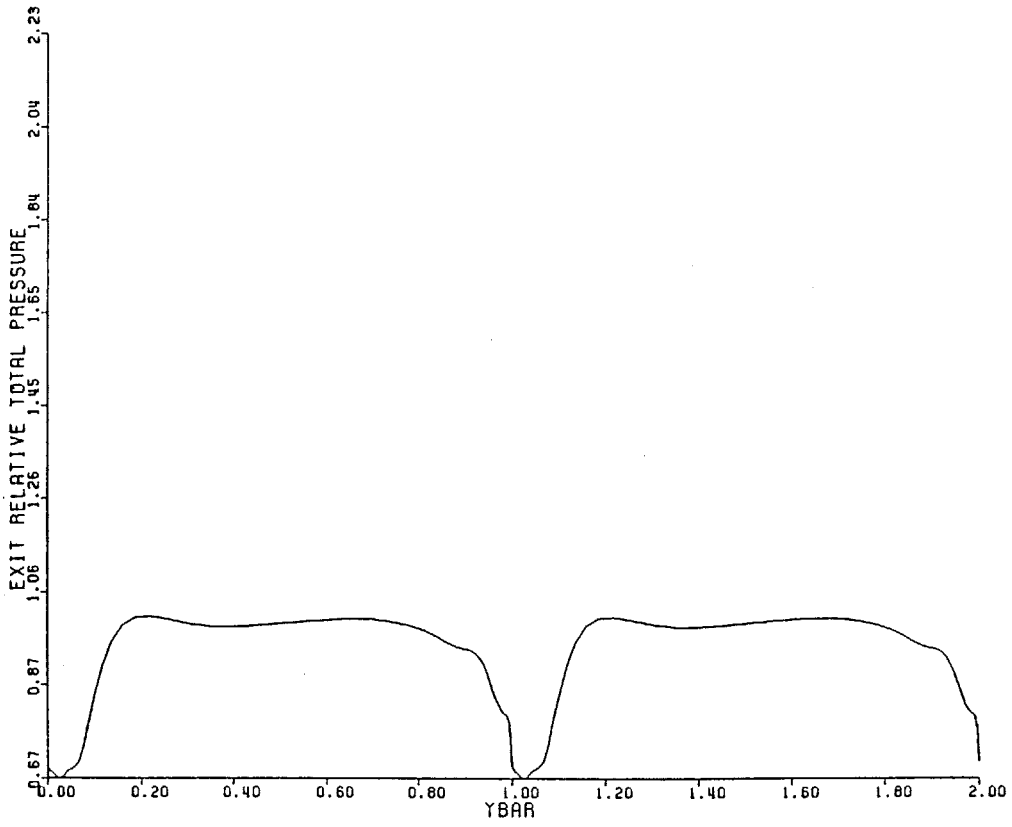

Figure 4.6 Relative Total Pressure vs. Fractional Blade Spacing 1.6 Trailing Edge Diameters Downstream of Trailing Edge Steady State Iteration 2500

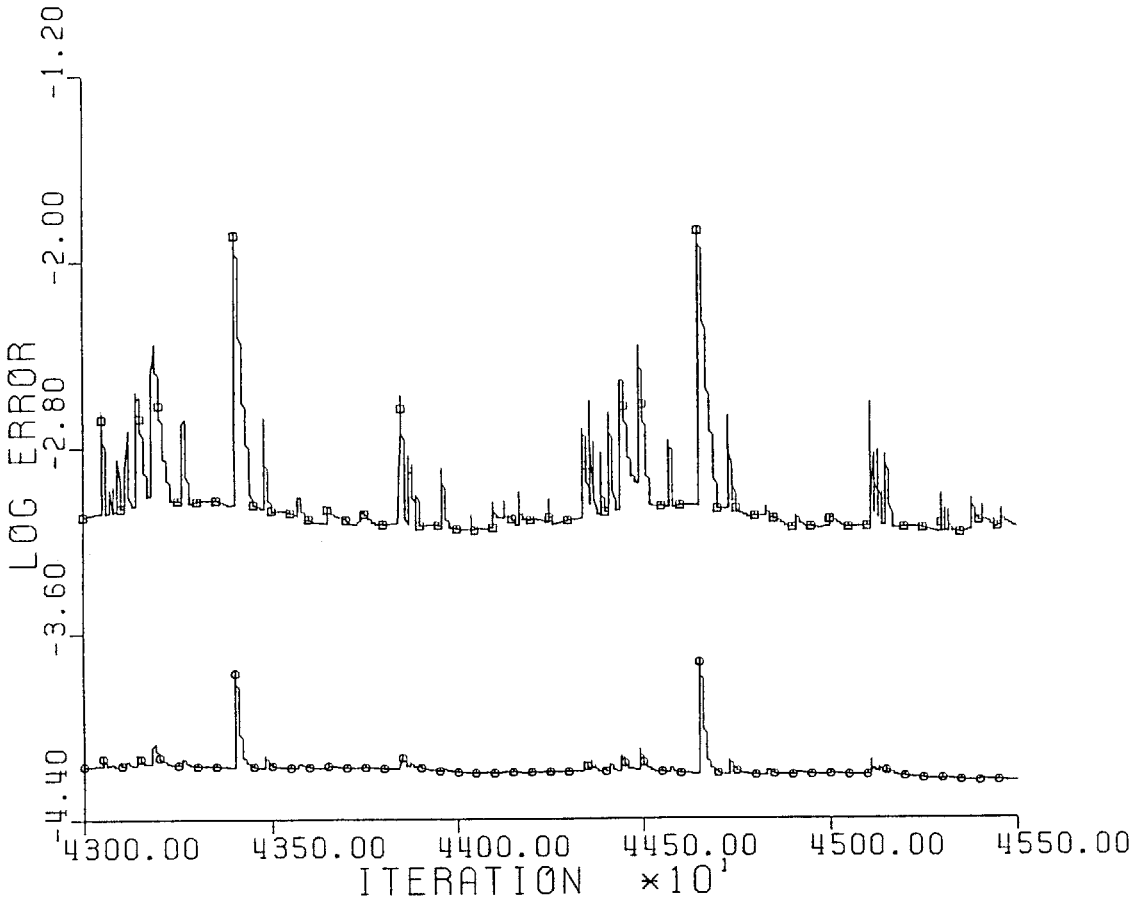

Figure 5.1 Segment of Time-Accurate "Convergence" History (Strong Shedding)

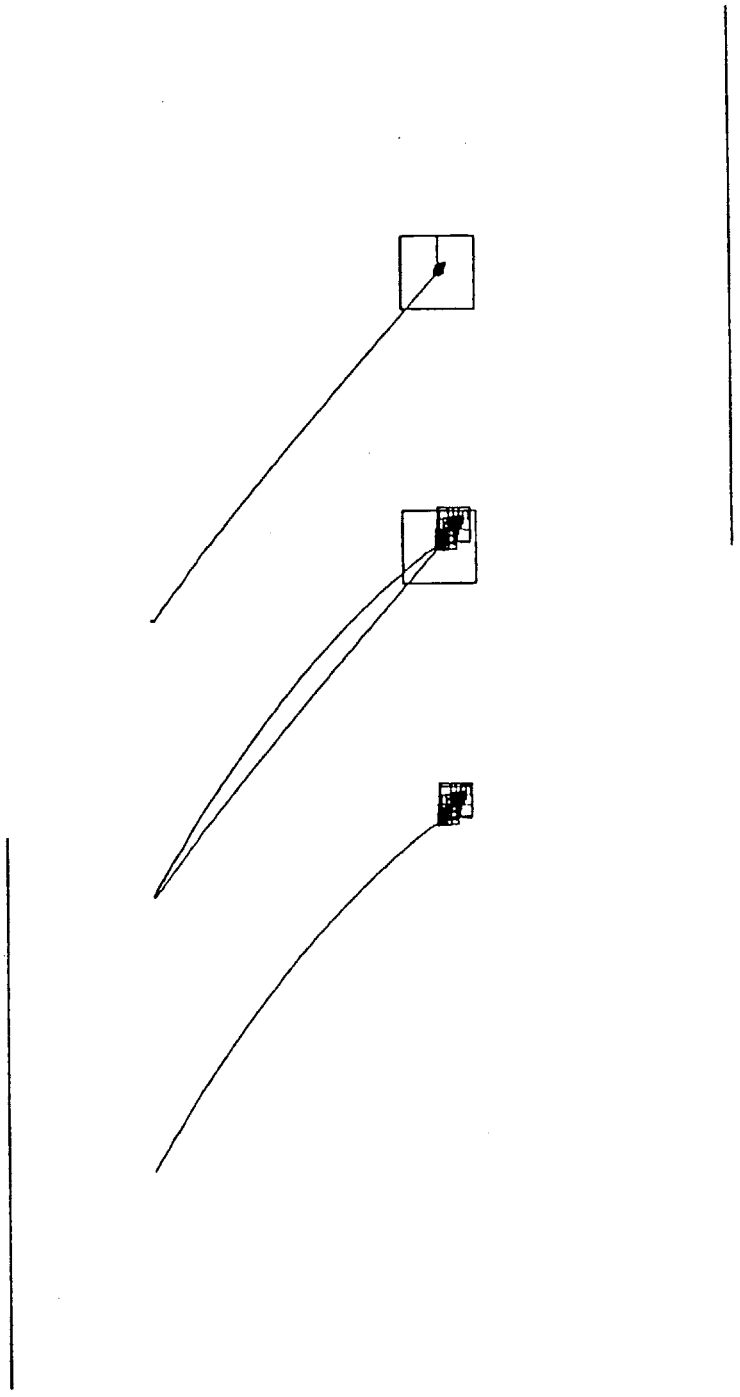

Figure 5.2 Maximum Change Locations for Convergence History Segment Presented in Figure 5.1

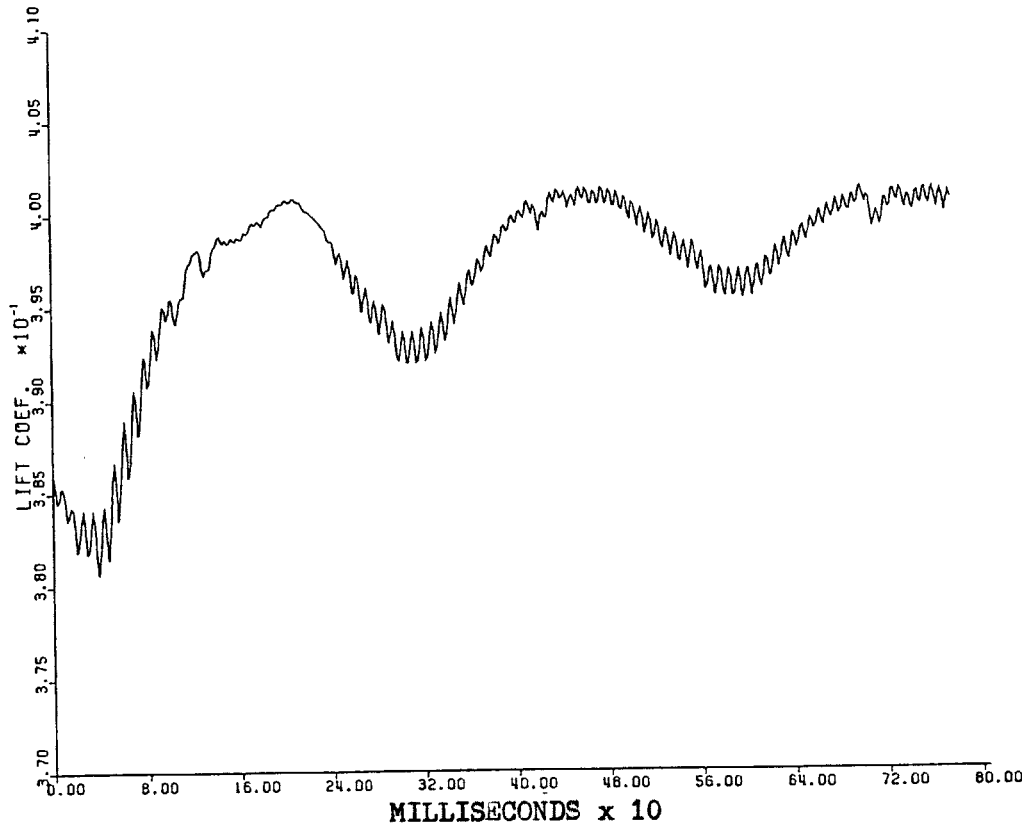

Figure 5.3 Coefficient of Lift vs. Time

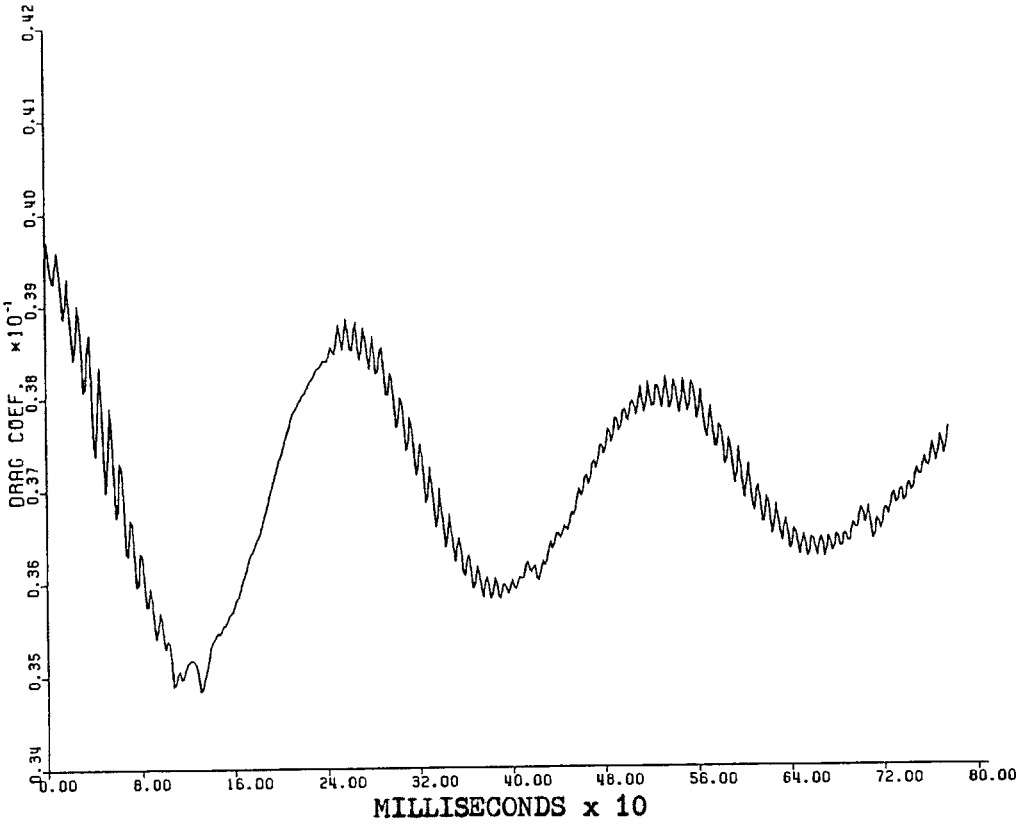

Figure 5.4 Coefficient of Drag vs. Time

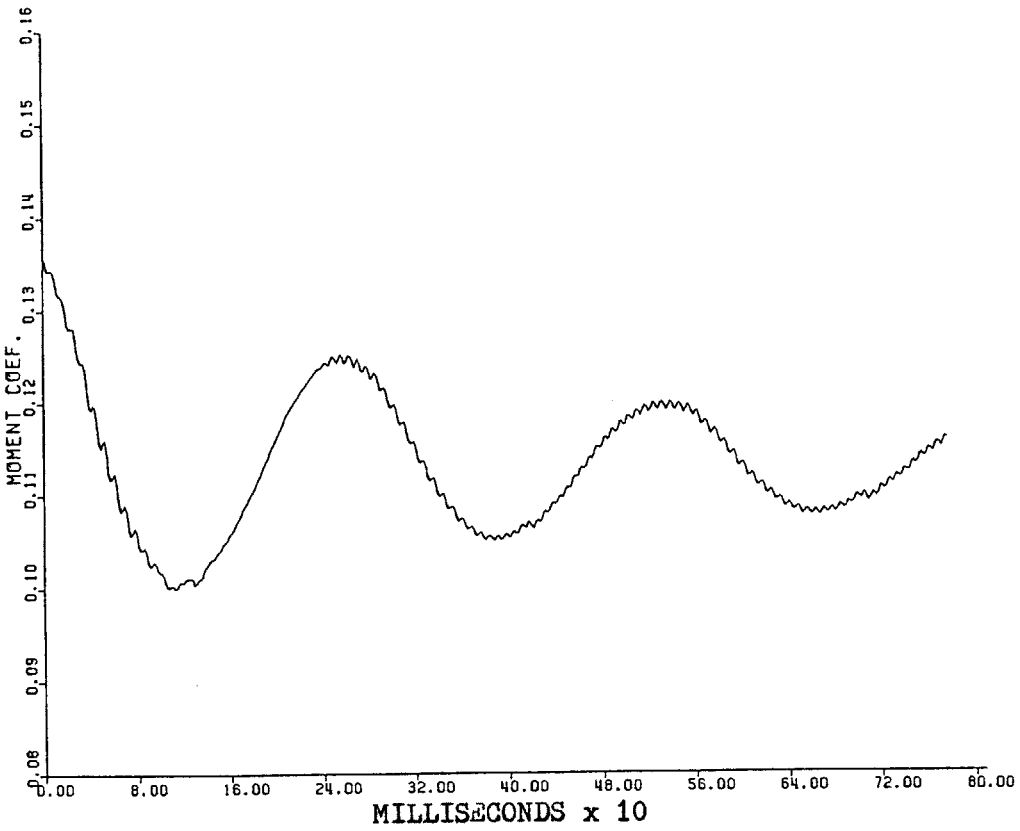

Figure 5.5 Coefficient of Moment vs. Time

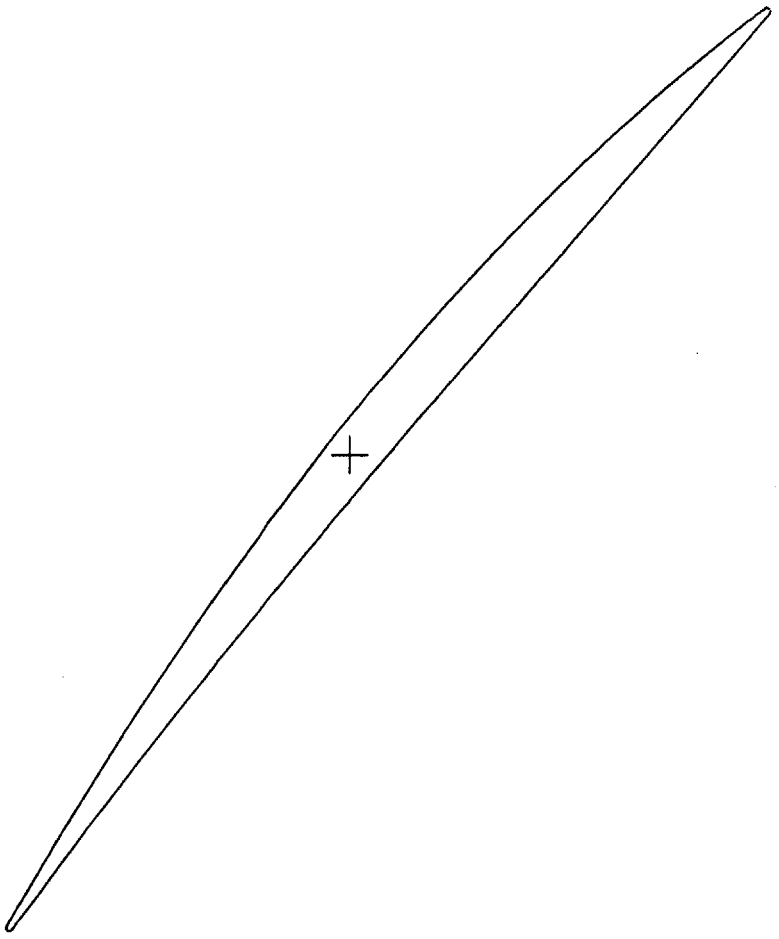

Figure 5.6 Location of Moment Center Used in Figure 5.5

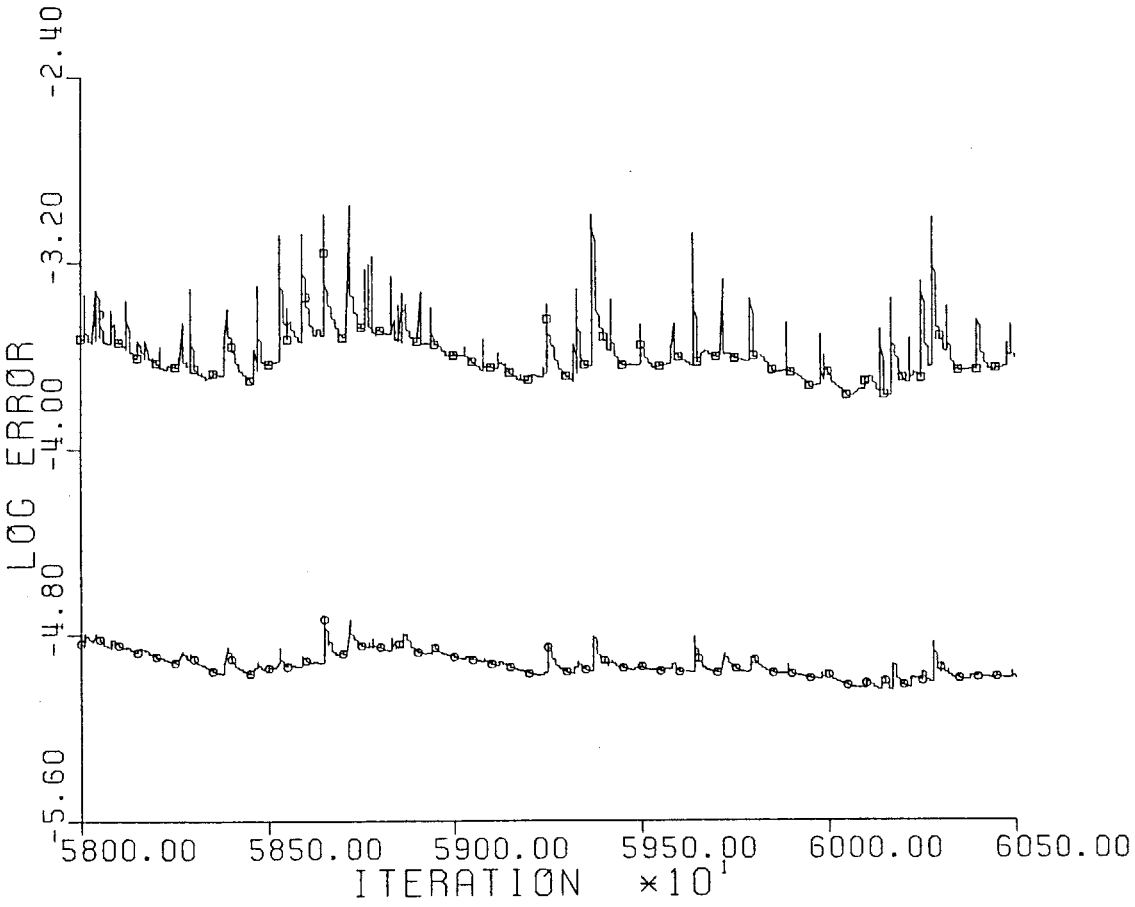

Figure 5.7 Segment of Time-Accurate "Convergence" History (Weak Shedding)

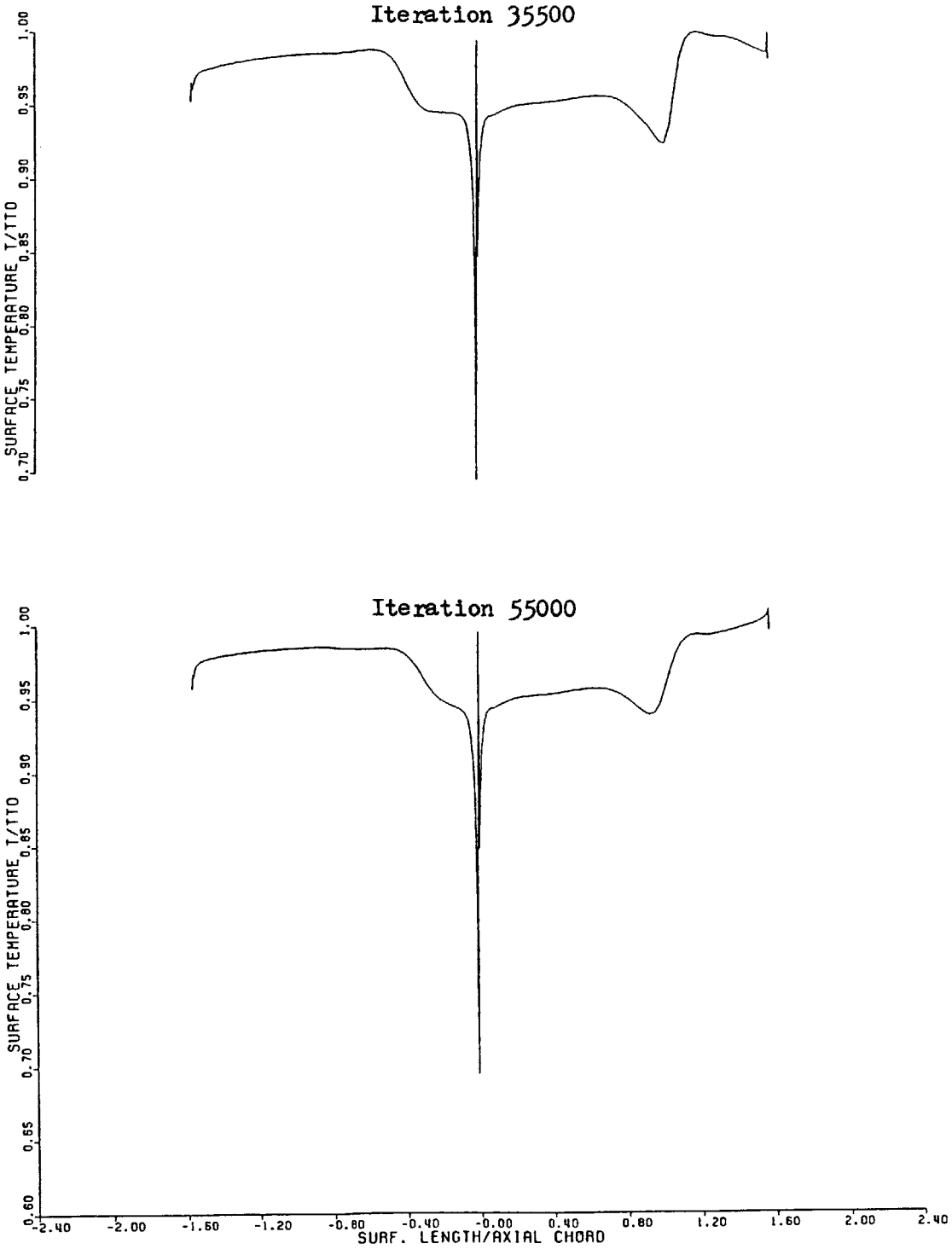

Figure 5.8 Surface Temperature Distributions at Two Different Times

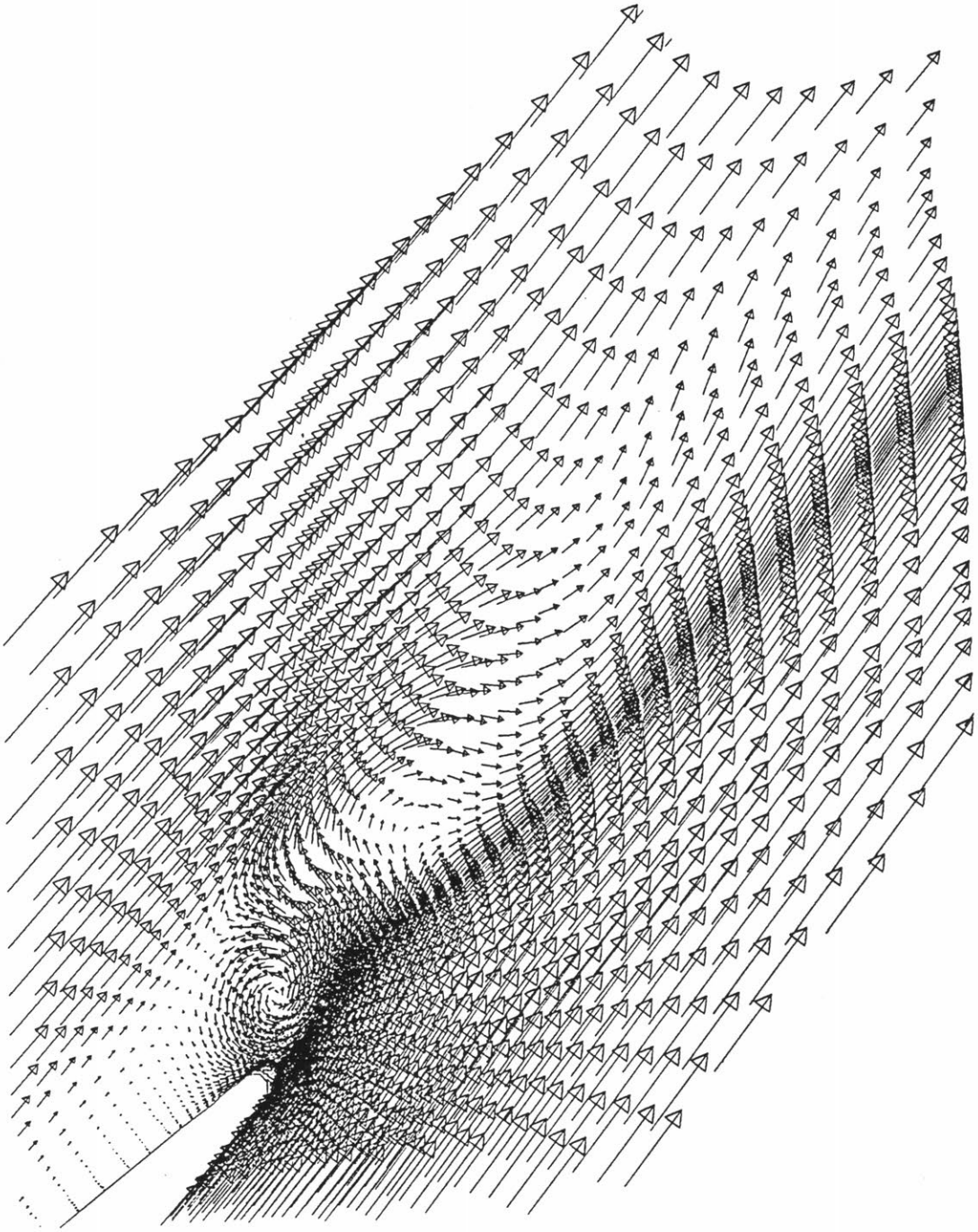

Figure 6.1 Velocity Vectors in the Blade Frame of Reference for Iteration 42500

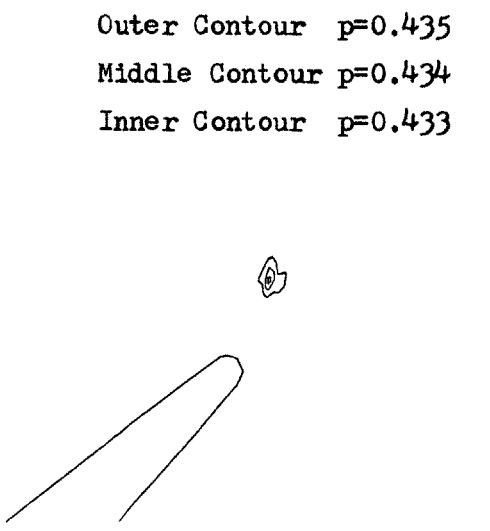

Figure 6.2 Static Pressure Contours from Iteration 42500 Showing First Pressure Surface Vortex Near Trailing Edge

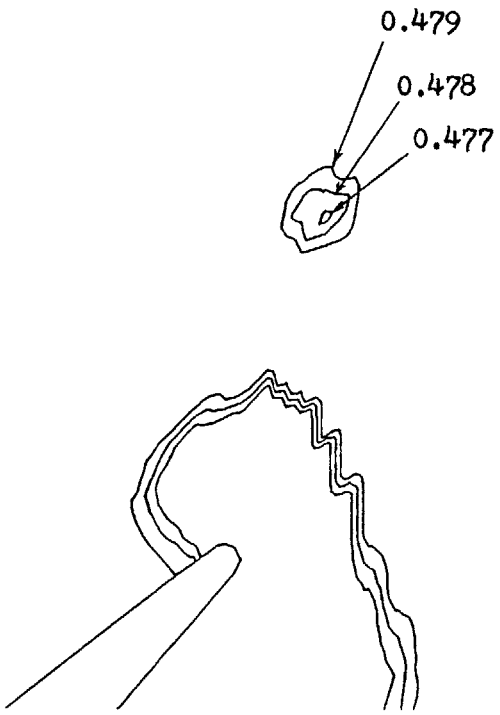

Figure 6.3 Static Pressure Contours from Iteration 42500 Showing Suction Surface Vortex

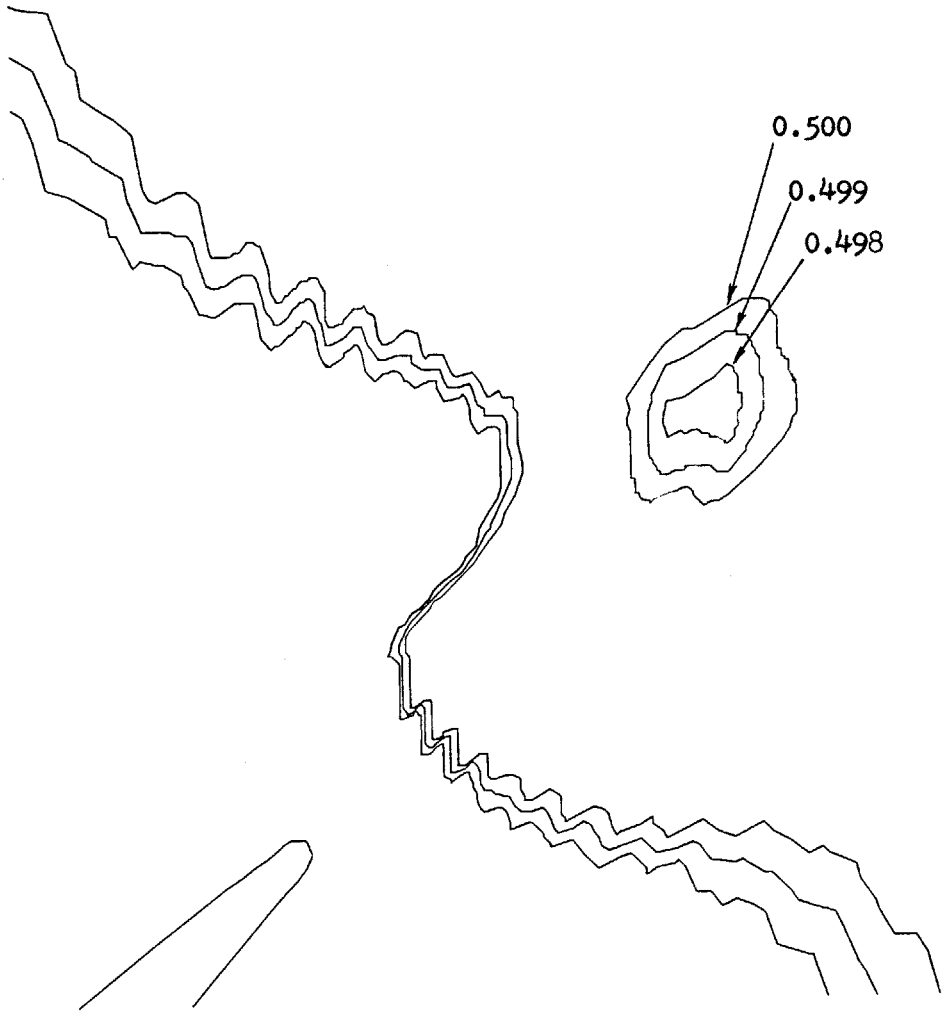

Figure 6.4 Static Pressure Contours from Iteration 42500 Showing Second Pressure Surface Vortex

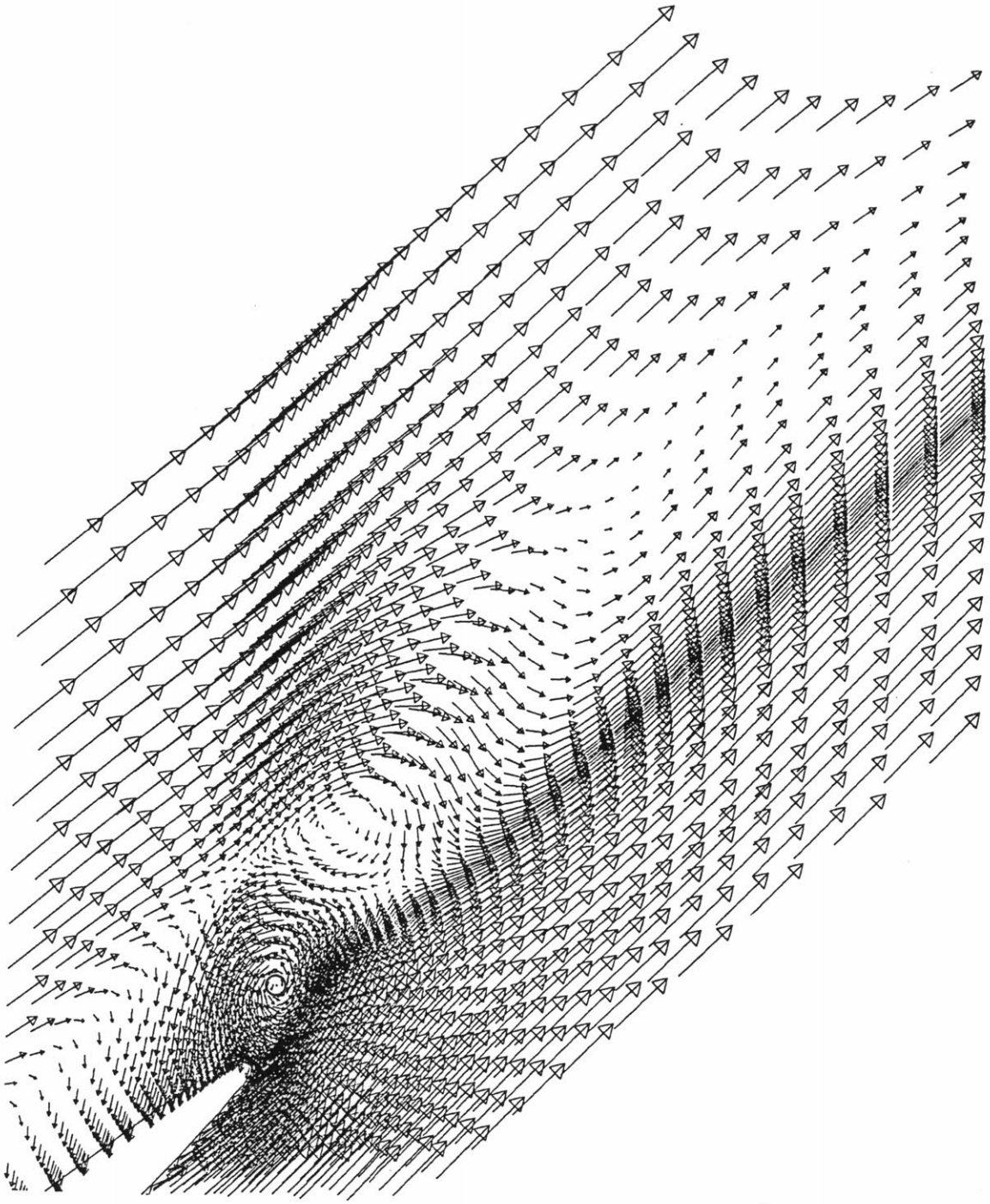

Figure 6.5 Velocity Vectors from Iteration 42500 in Frame of Reference of First Pressure Surface Vortex

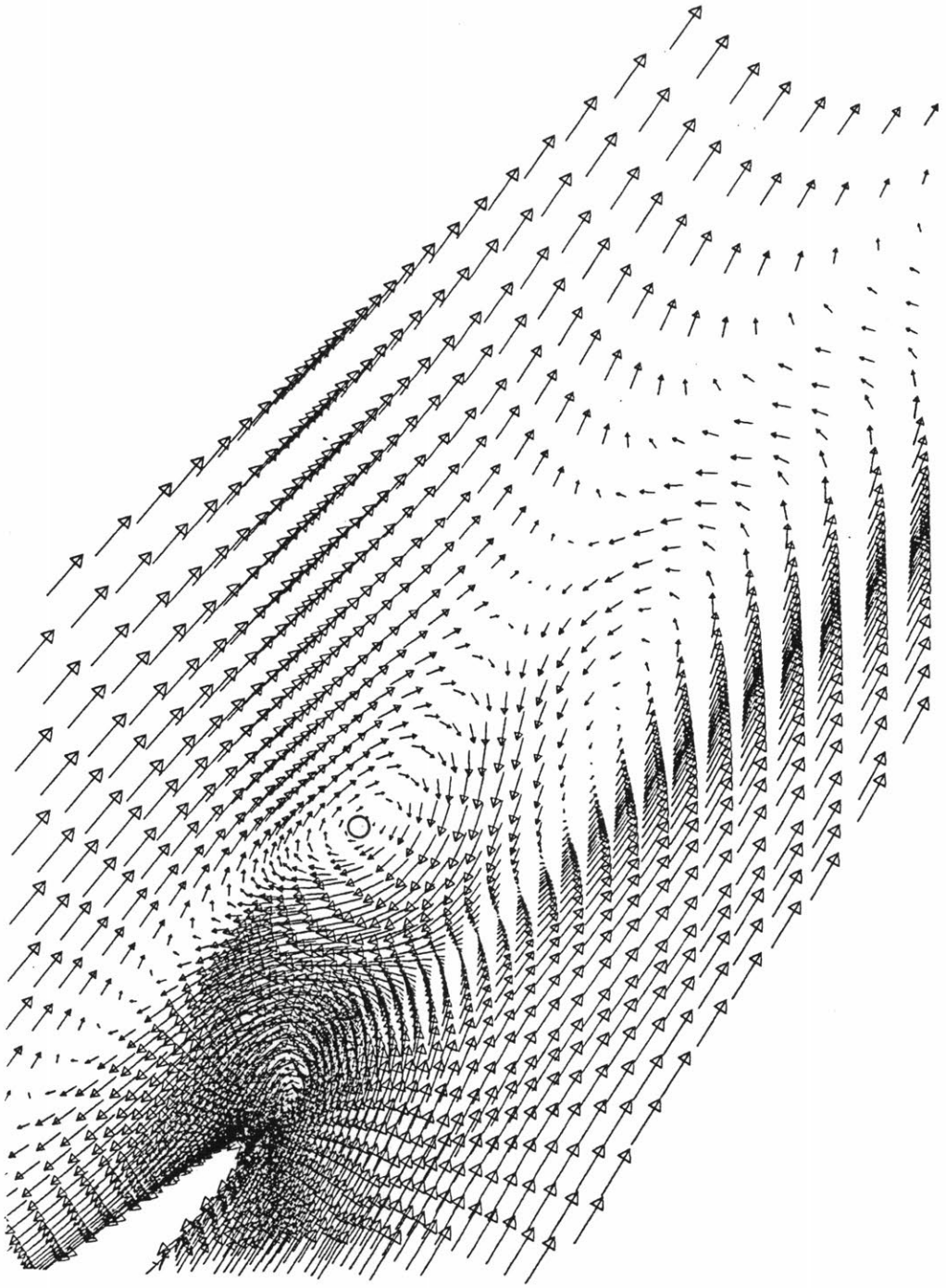

Figure 6.6 Velocity Vectors from Iteration 42500 in Frame of Reference of Suction Surface Vortex

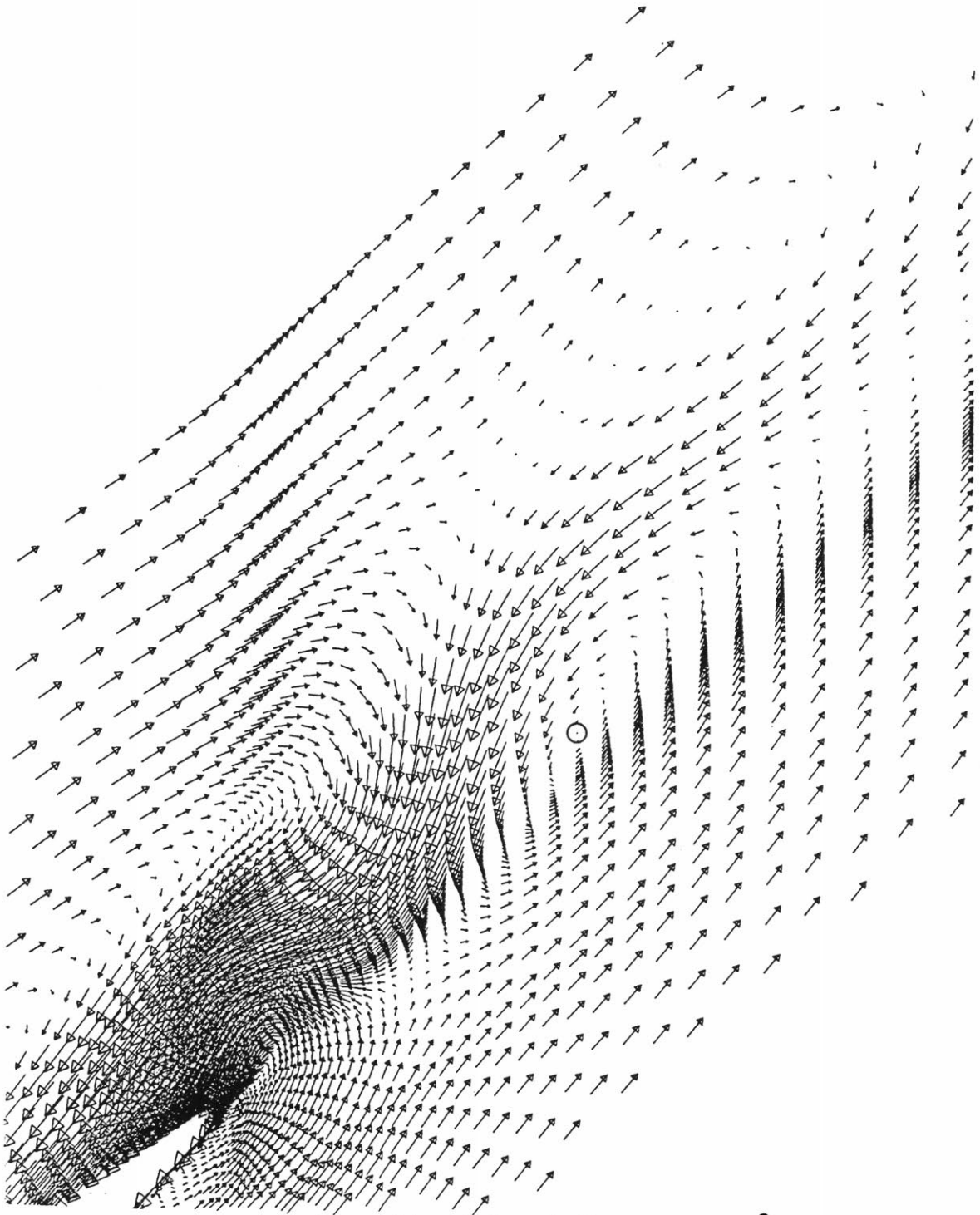

Figure 6.7 Velocity Vectors from Iteration 42500 in Frame of Reference of Second Pressure Surface Vortex

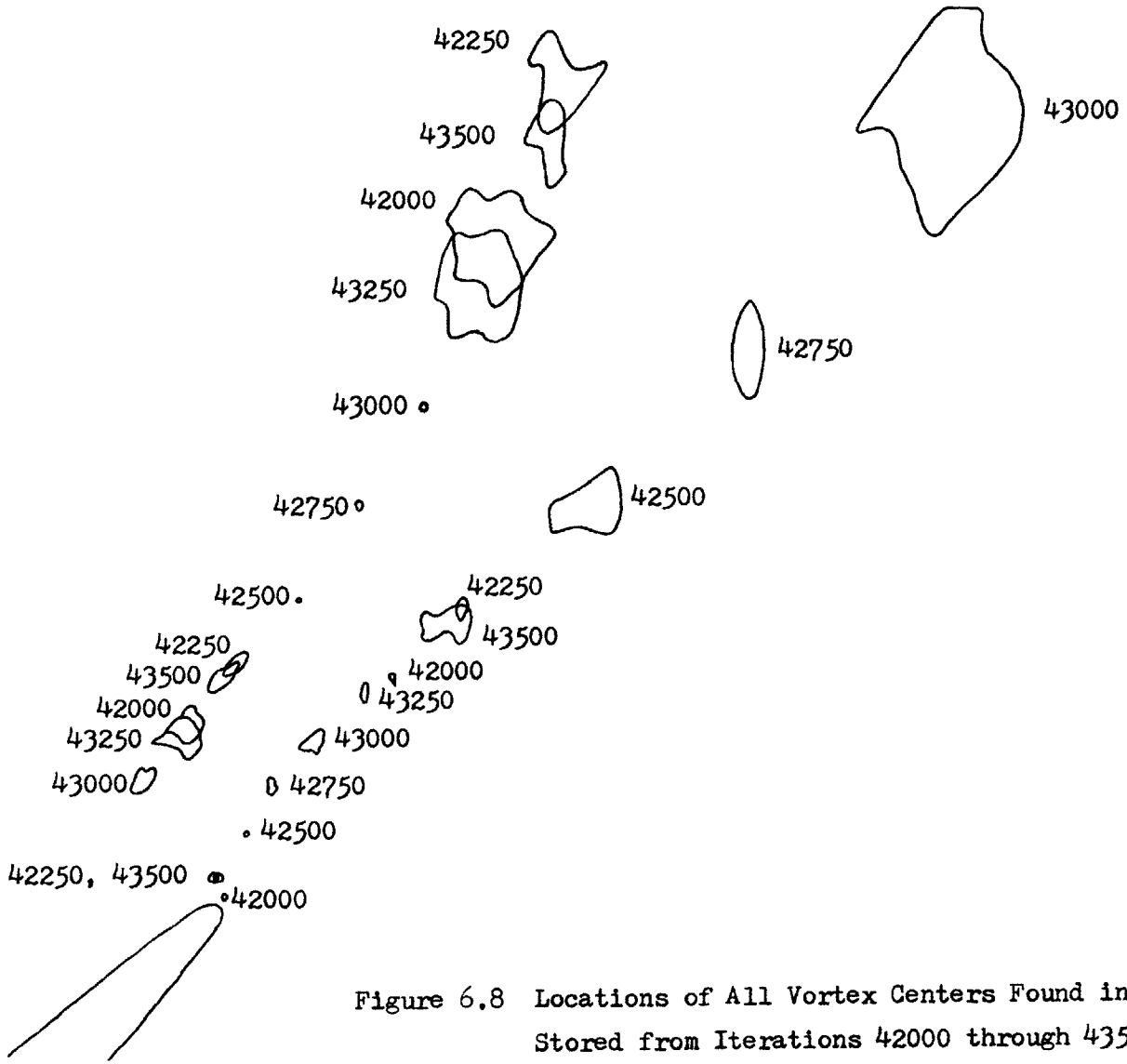

Figure 6.8 Locations of All Vortex Centers Found in Solutions Stored from Iterations 42000 through 43500

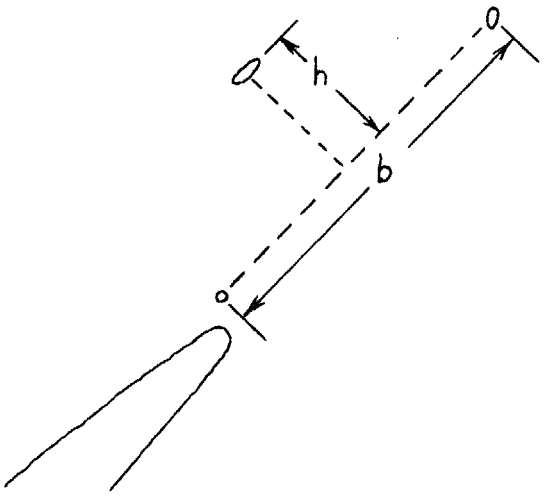

Figure 6.9 Vortex Core Locations at Iteration 42250

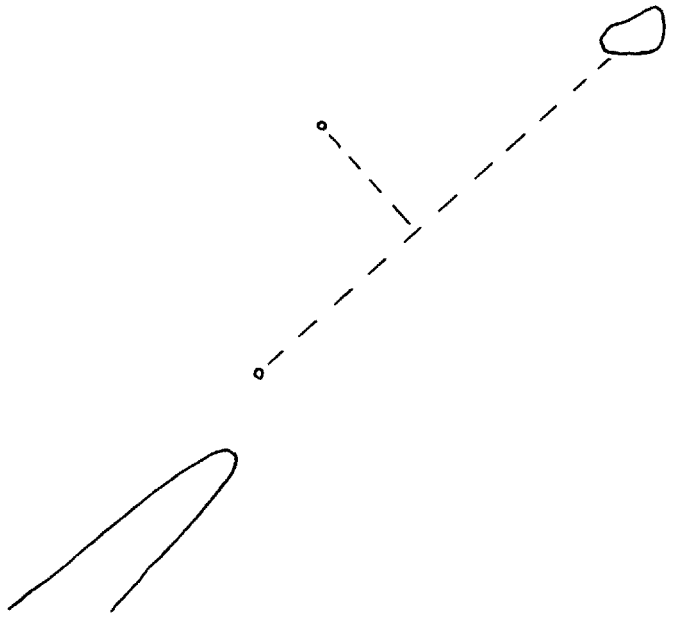

Figure 6.10 Vortex Core Locations at Iteration 42500

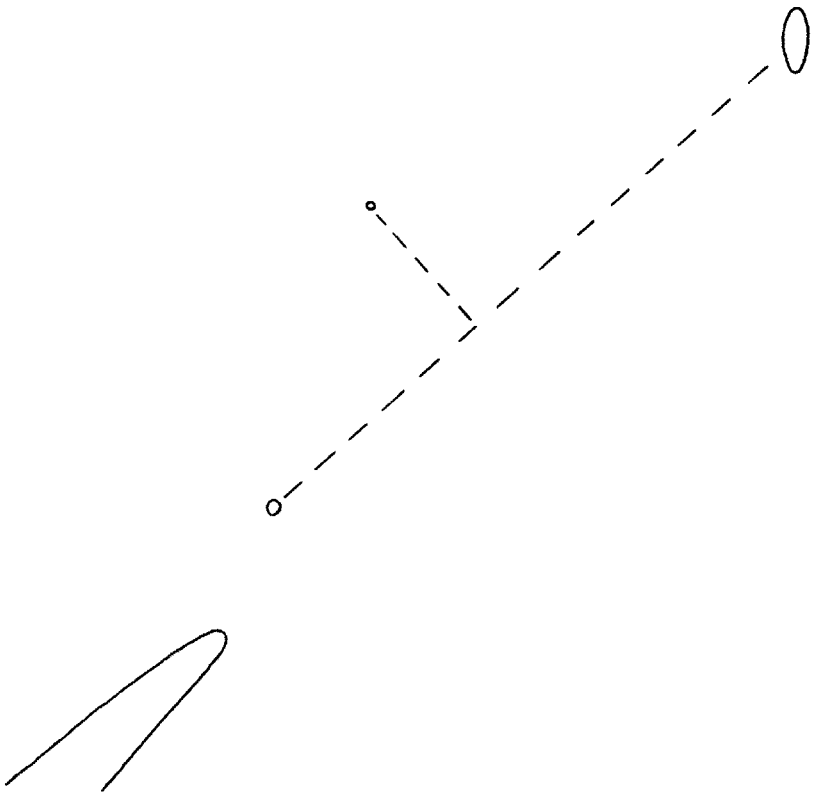

Figure 6.11 Vortex Core Locations at Iteration 42750

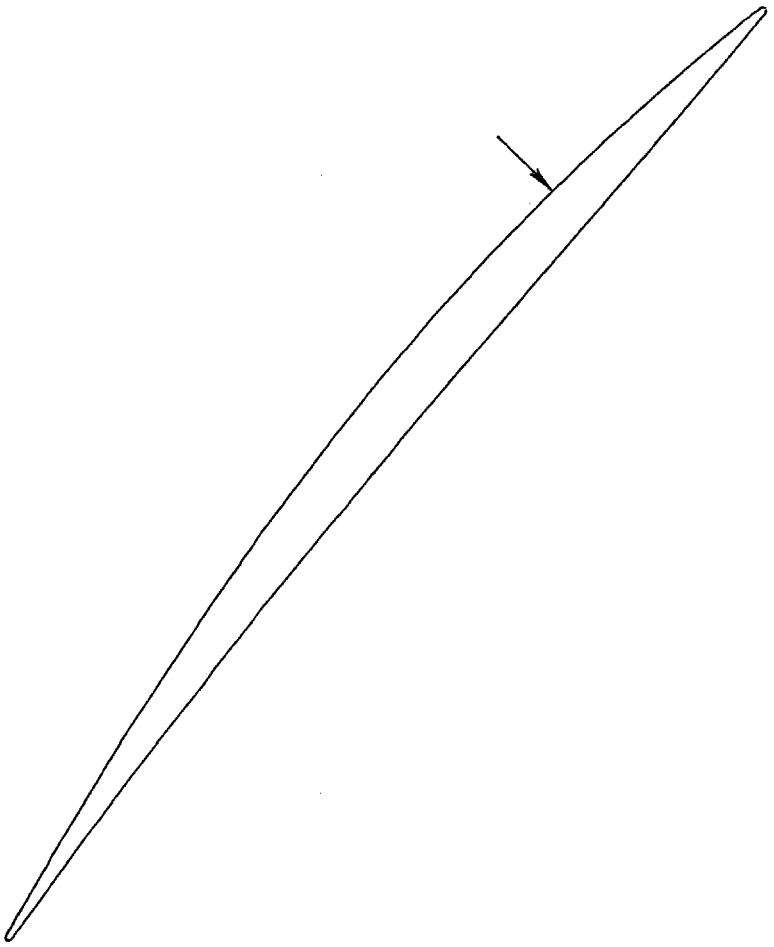

Figure 6.12 Typical Suction Surface Separation Location

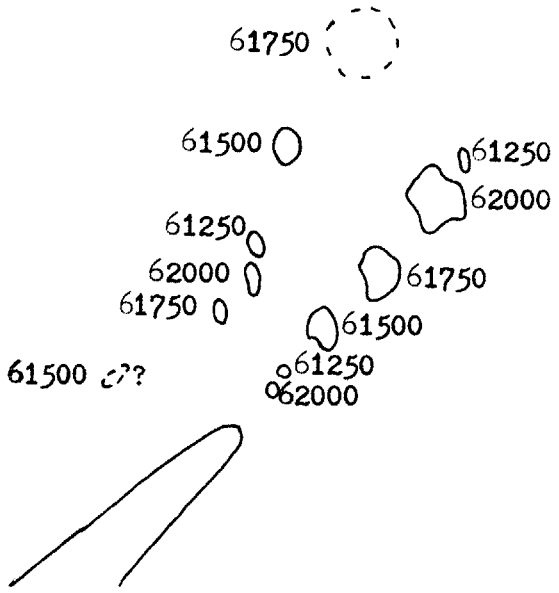

Figure 6.13 Locations of All Vortex Centers Found in Solutions Stored from Iterations 61250 through 62000

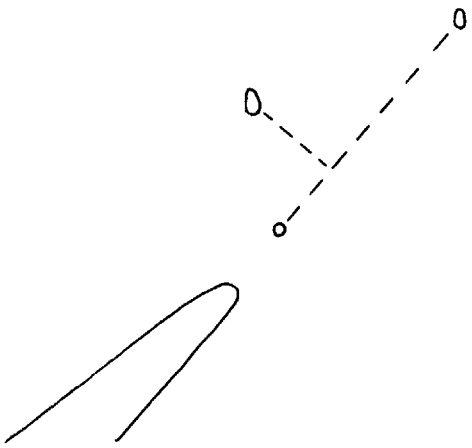

Figure 6.14 Vortex Core Locations at Iteration 61250

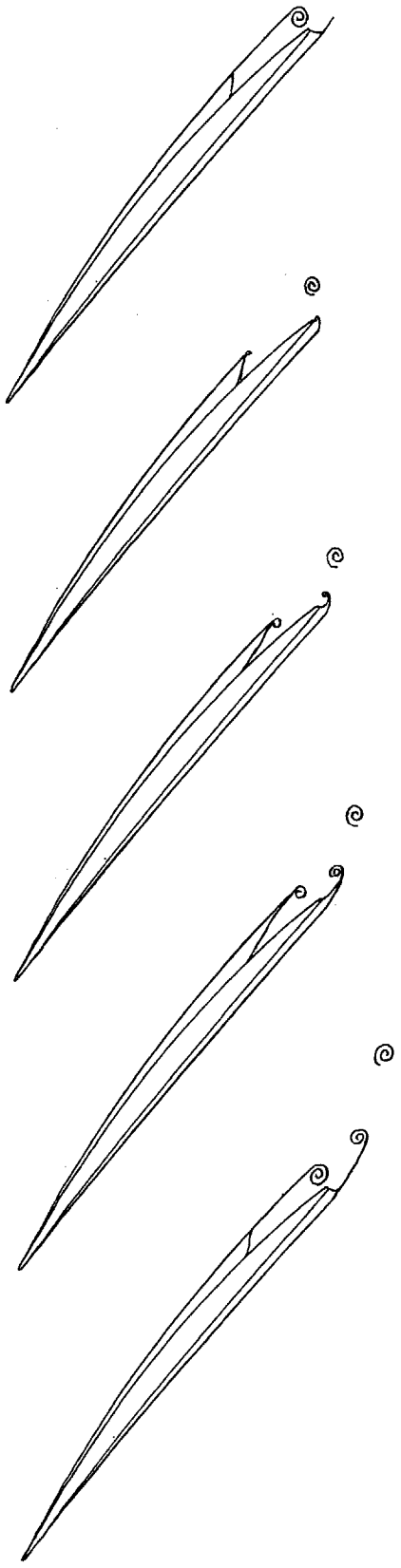

Figure 6.15 Schematic of Hypothesized Vortex Shedding Mechanics

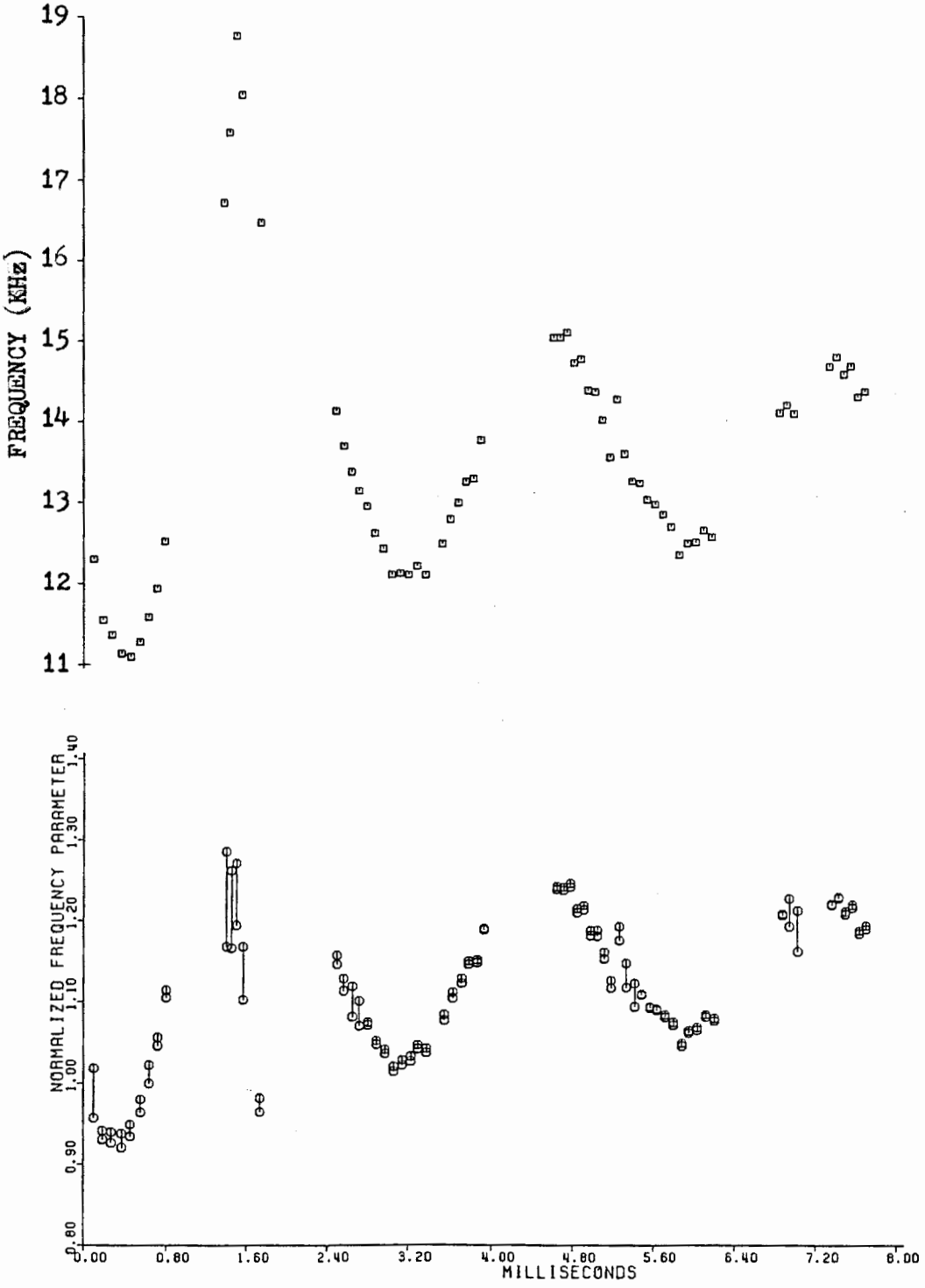

Figure 6.16 Normalized Frequency Parameter and Actual Shedding Frequencies

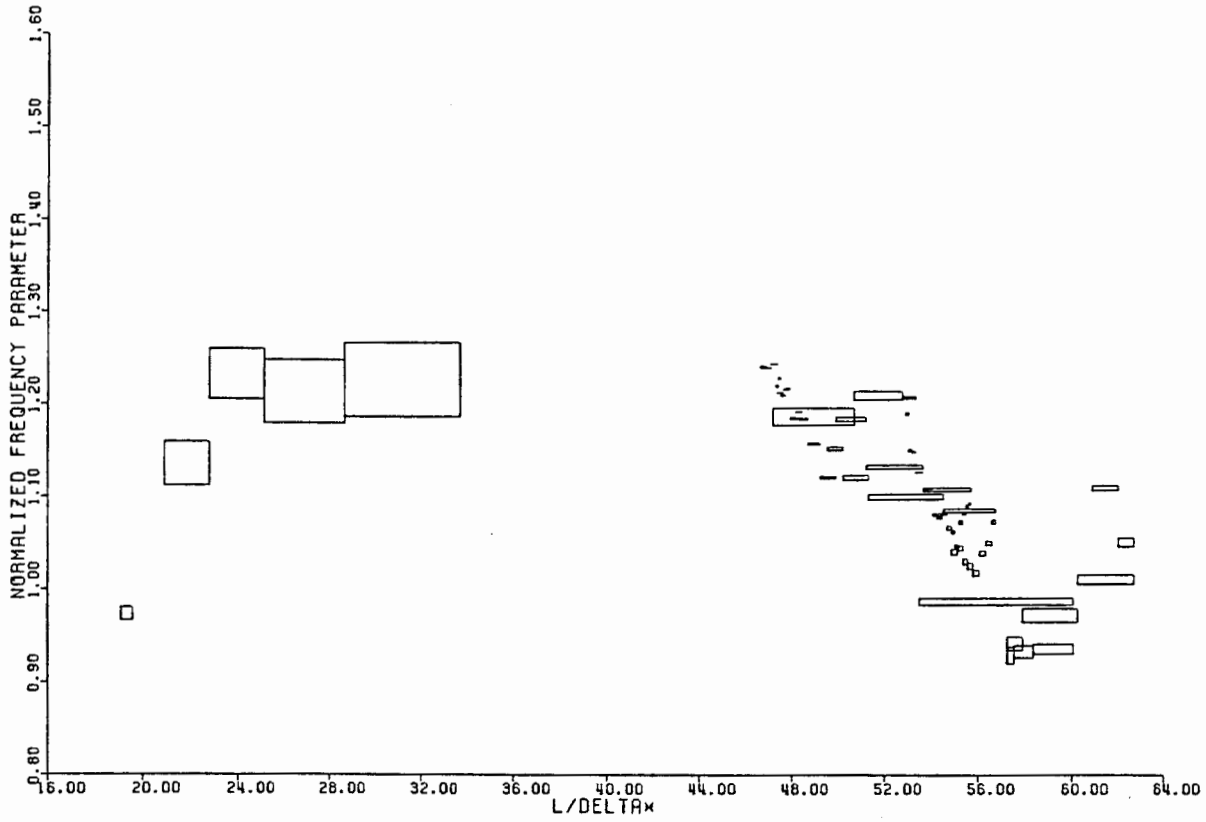

Figure 6.17 Normalized Frequency Parameter vs. L/δ^*

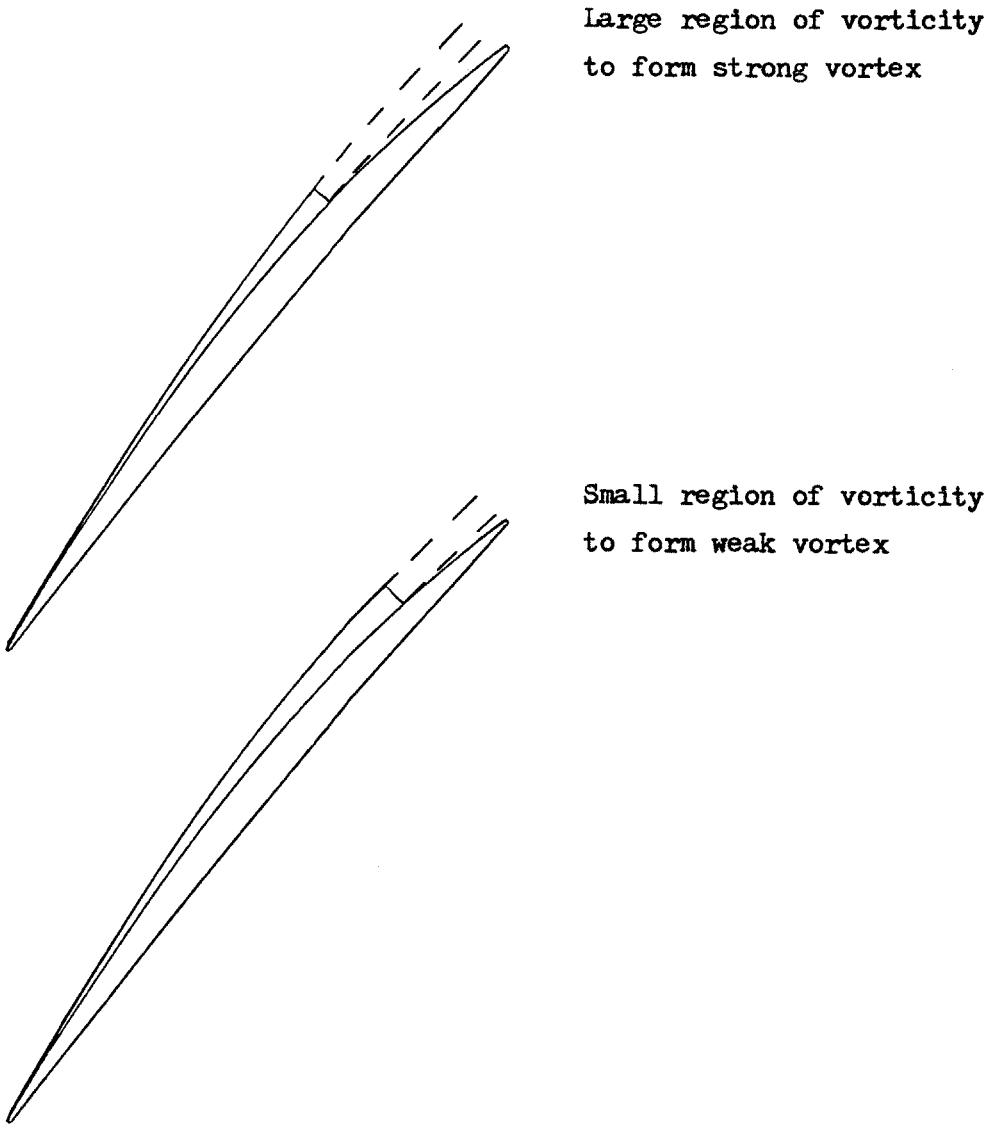

Figure 6.18 Schematic of Vortex Strength Variation with Separation Point Location

CONTOUR C FOR CALCULATING CIRCULATION $d\Gamma$

THE SIDES OF C ARE PERPENDICULAR TO THE FLOW.

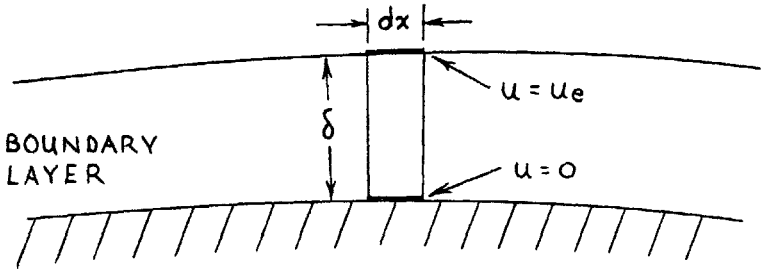

$$d\Gamma = u_e \, dx$$

BY STOKES, $d\Gamma = \zeta \, dA$

WHERE ζ IS THE AVERAGE VORTICITY WITHIN C.

$$dA = \delta \, dx$$

THEREFORE $$\zeta = \frac{u_e}{\delta}$$

Figure 6.19 Calculation of Average Local Boundary Layer Vorticity

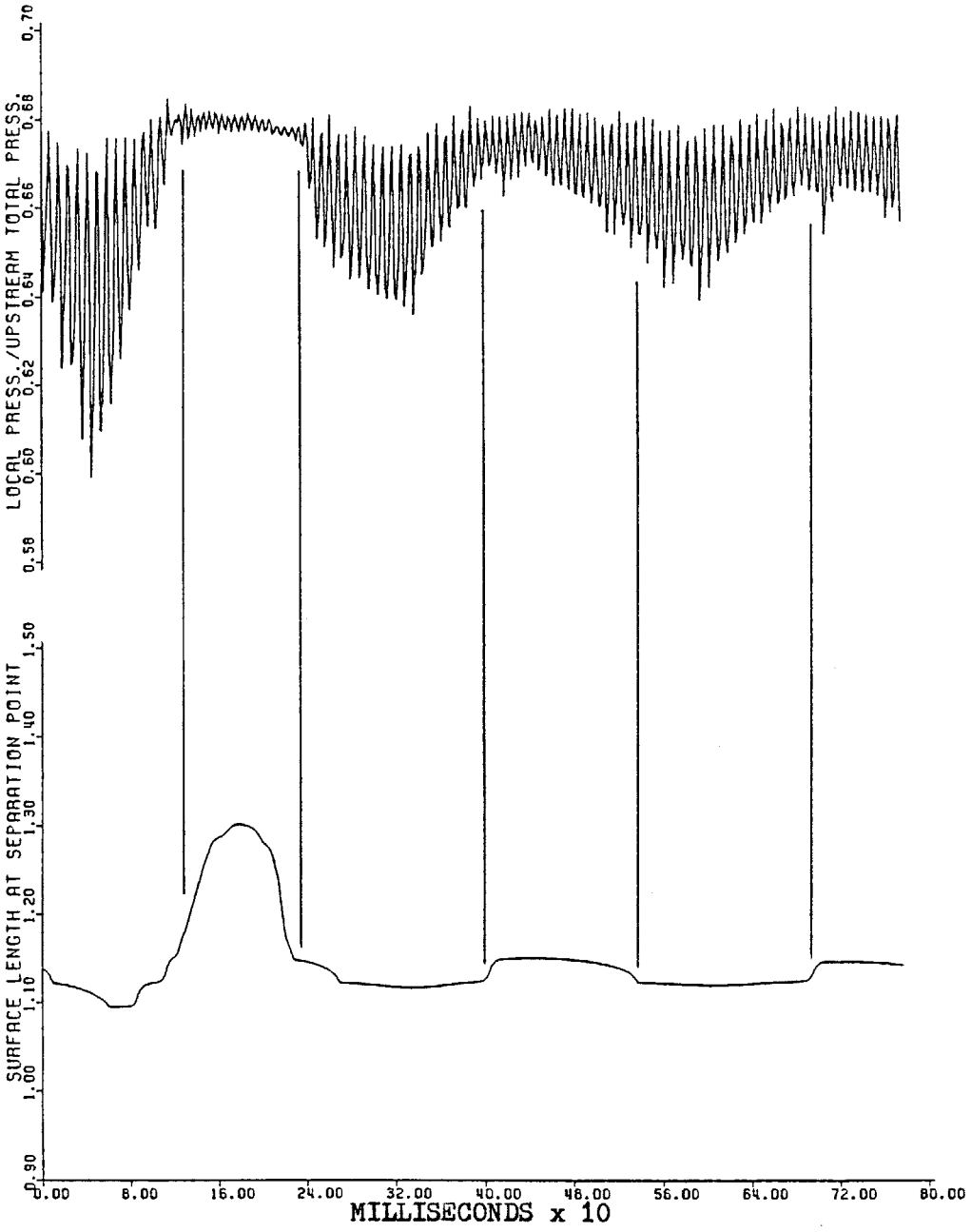

Figure 6.20 Separation Point Location with Regions of Strong and Weak Vortex Shedding as Shown by Trailing Edge Static Pressure Fluctuations

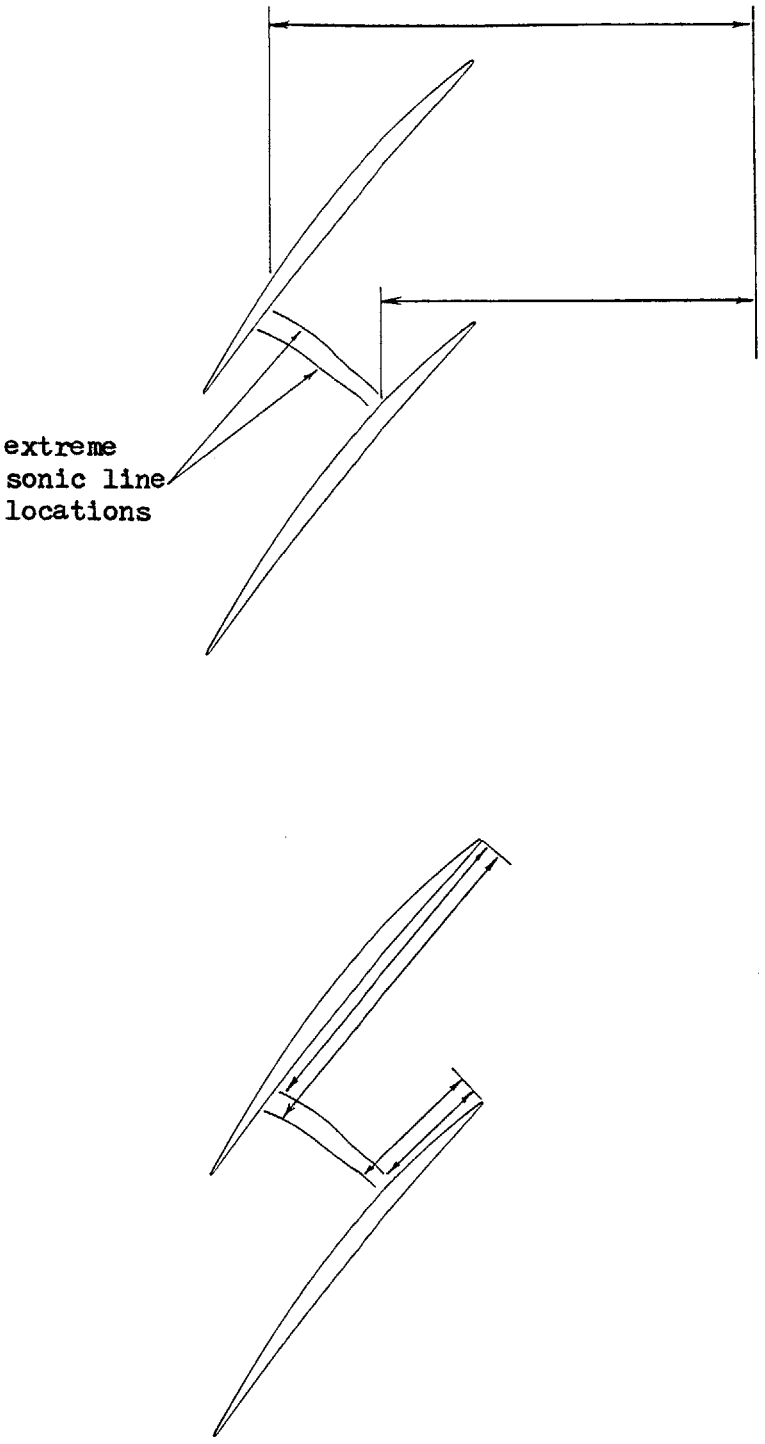

Figure 7.1 Distances Used in Estimating Extreme Frequencies of Oscillation Due to Wave Reflection Off the Downstream Computational Boundary

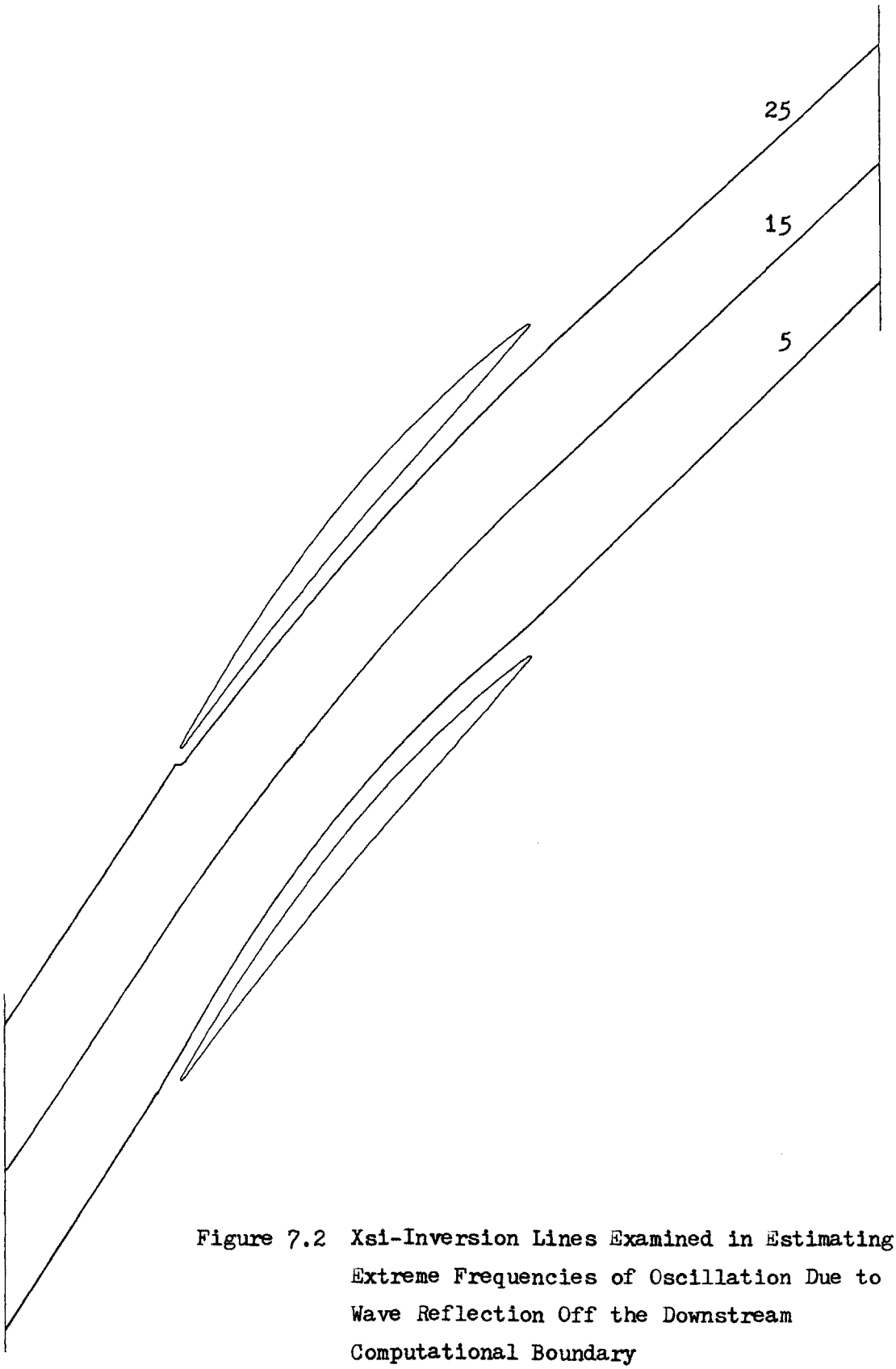

Figure 7.2 Xsi-Inversion Lines Examined in Estimating Extreme Frequencies of Oscillation Due to Wave Reflection Off the Downstream Computational Boundary

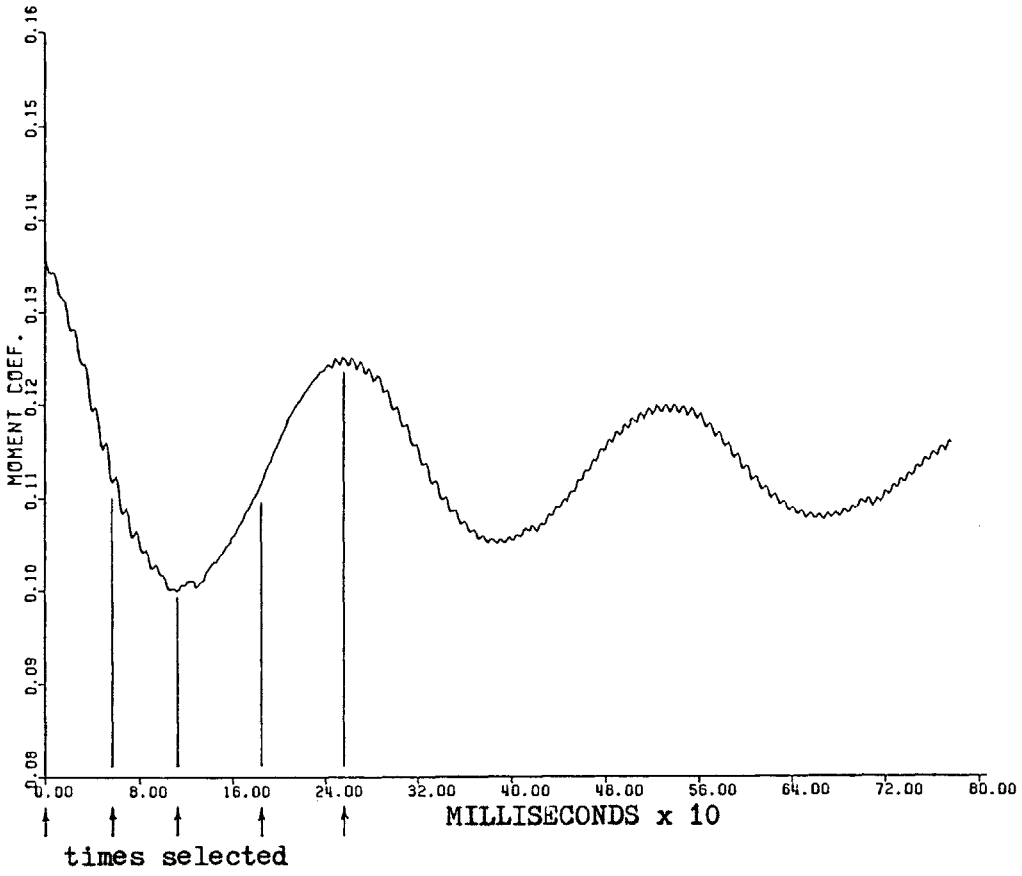

Figure 7.3 Times Selected in Estimating Extreme Frequencies of Oscillation Due to Wave Reflection Off the Downstream Computational Boundary (Relative to Airfoil Moment Variation)

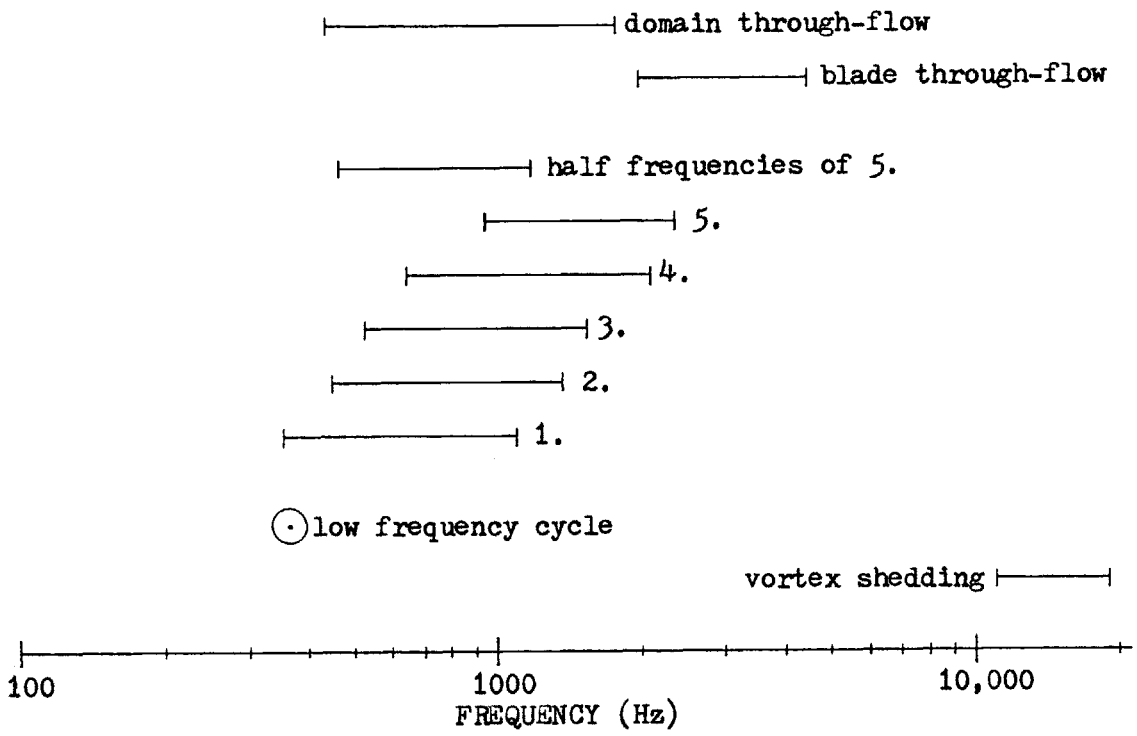

Figure 7.4 Relevant Frequencies in Time-Accurate Simulation of Flow in NASA Rotor 67 at 60 Percent Span

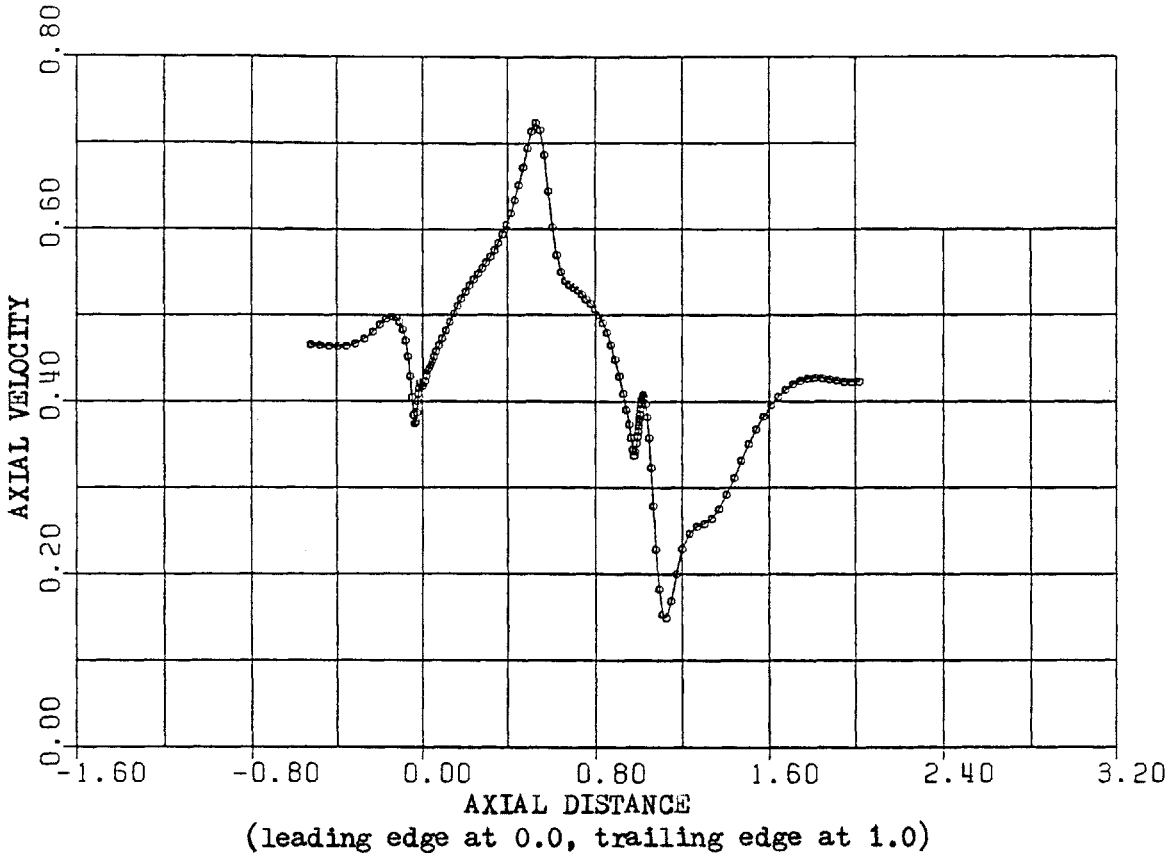

Figure 7.5 Axial Velocity Along Xsi-Inversion 5 at Iteration 42500

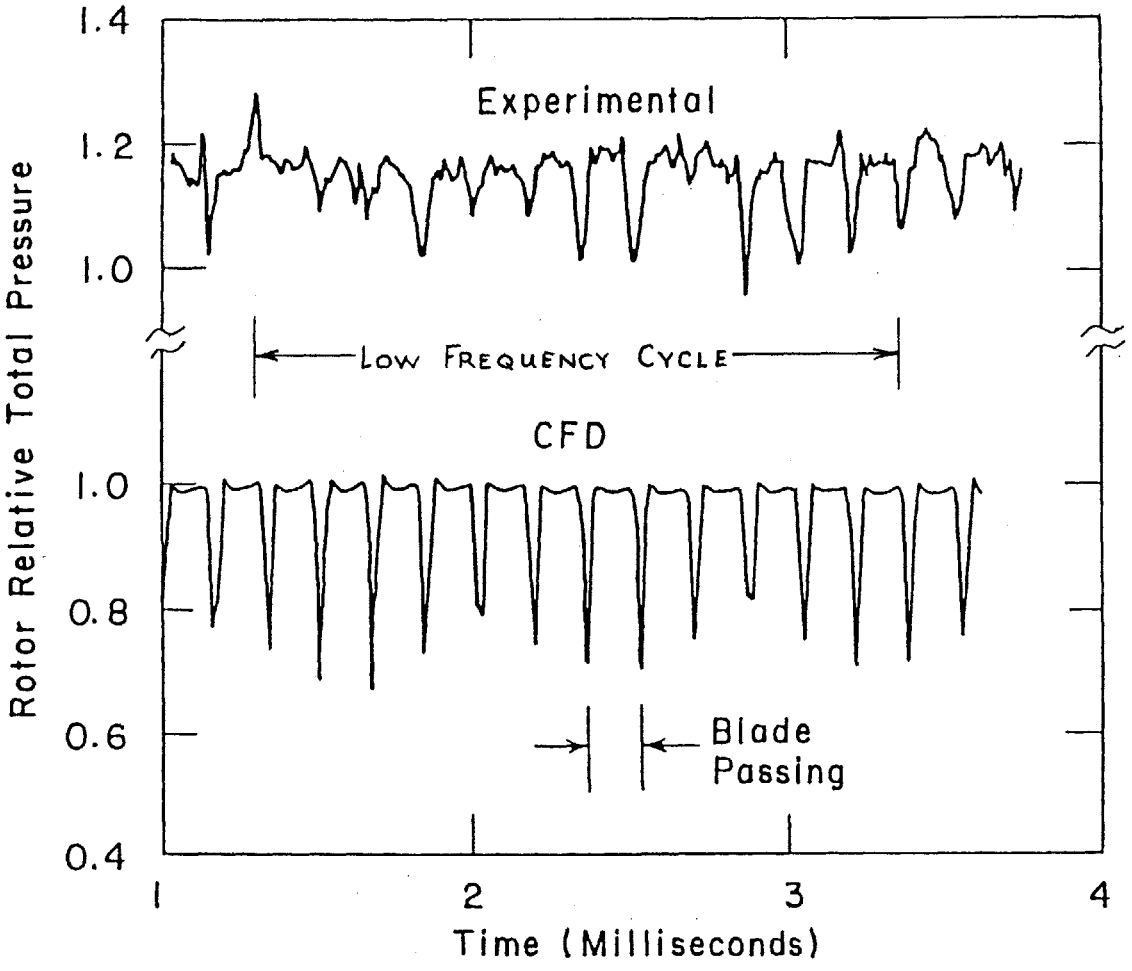

Figure 7.6 Relative Total Pressure Observed by a Stationary Observer Downstream of NASA Rotor 67 at Approximately 60% Span. Comparison of Experimental and Computational Results

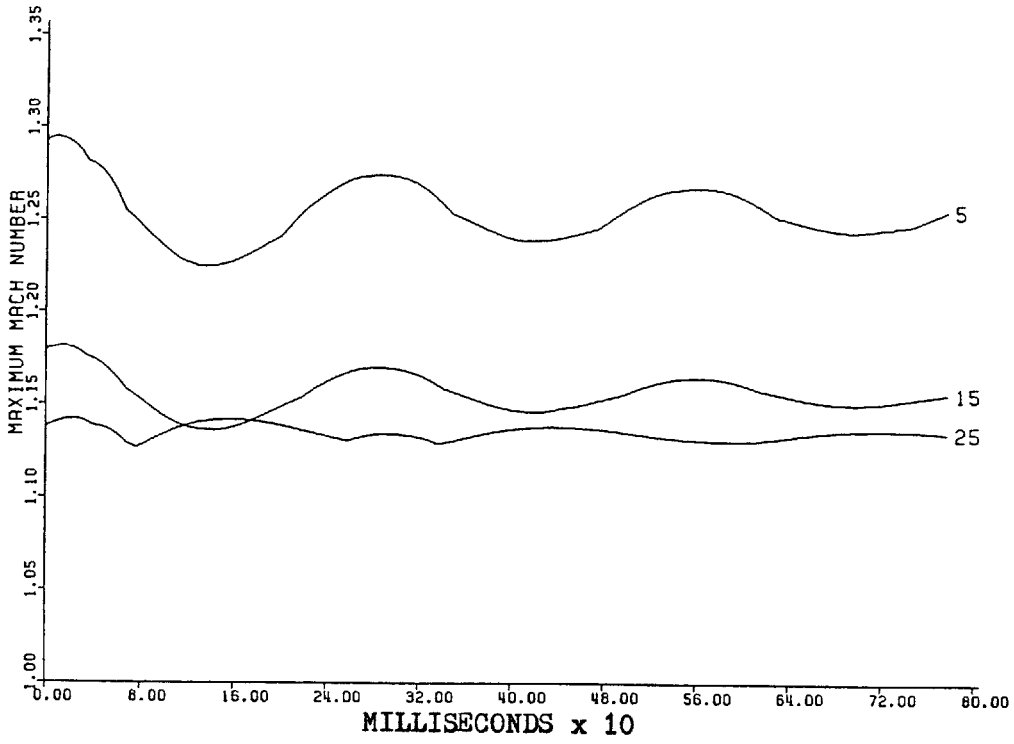

Figure 7.7 Maximum Mach Numbers Along Xsi-Inversion Lines 5, 15, and 25

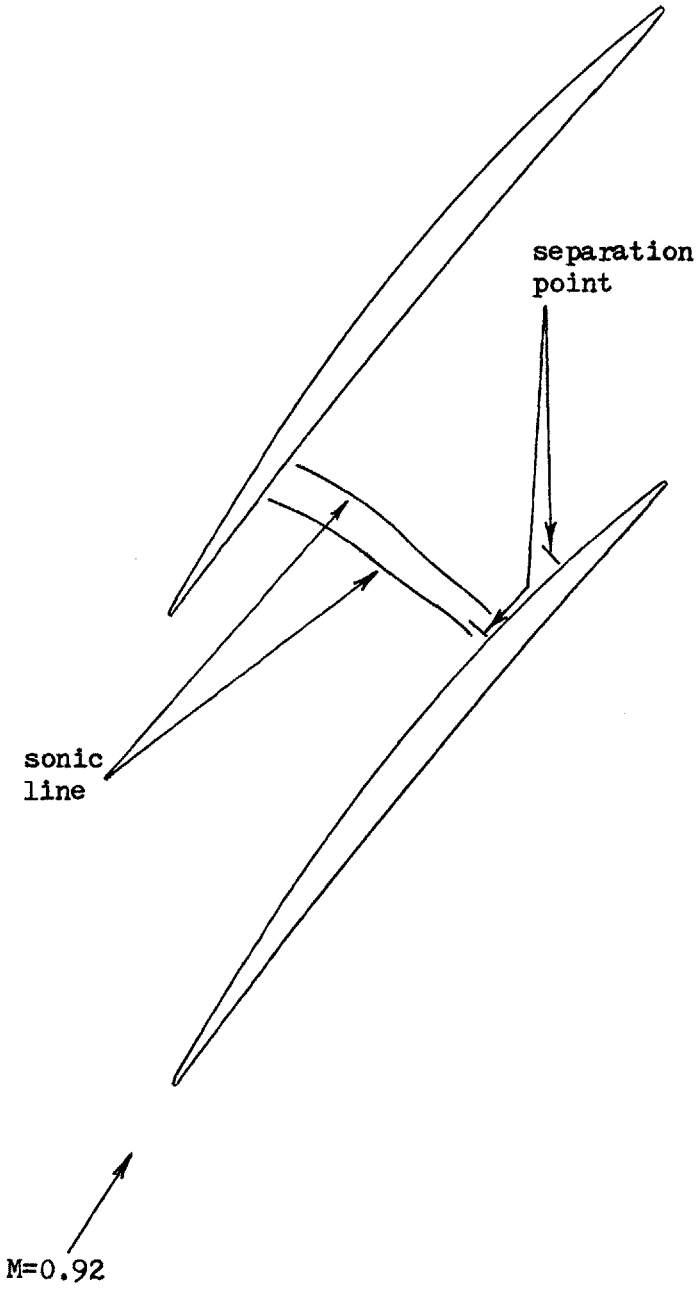

Figure 7.8 Extreme Locations of Sonic Line and Separation Point

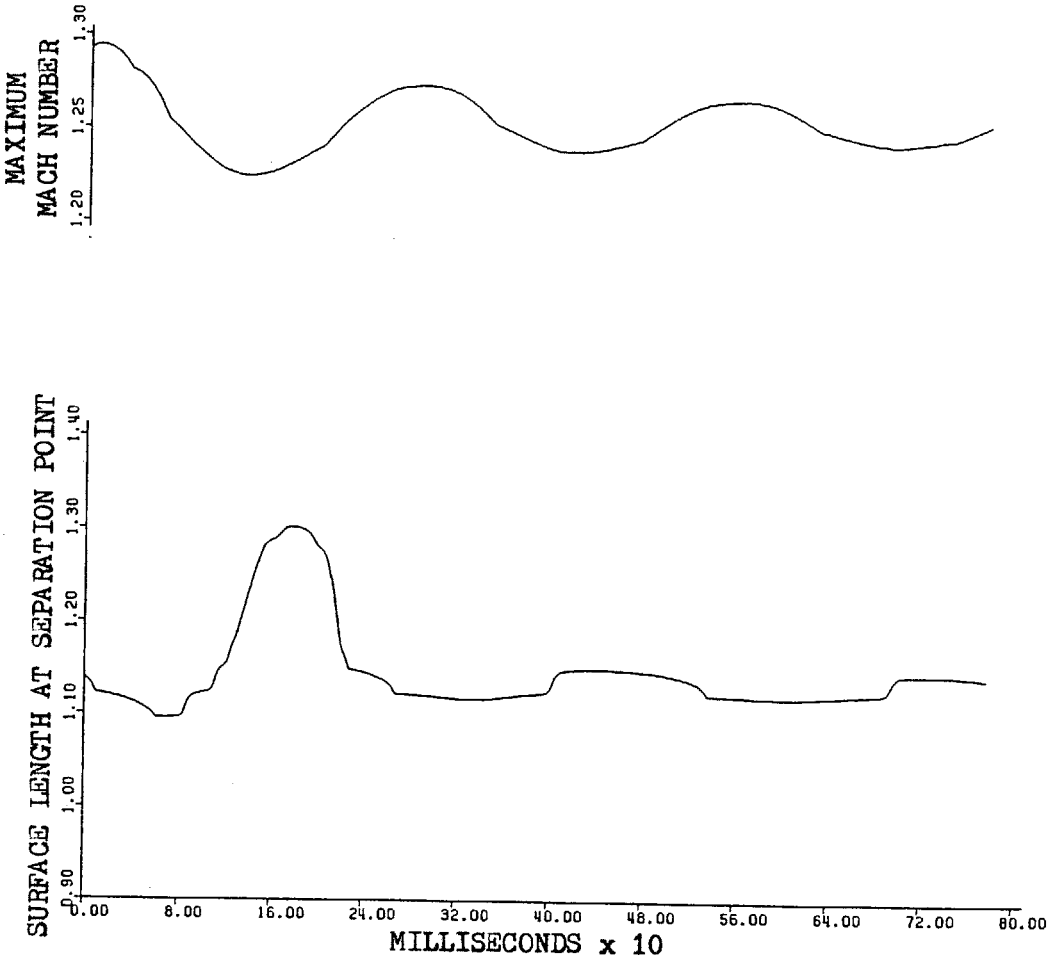

Figure 7.9 Separation Point and Maximum Mach Number for Xsi-Inversion 5

$$\Gamma = \int \zeta \, dA$$

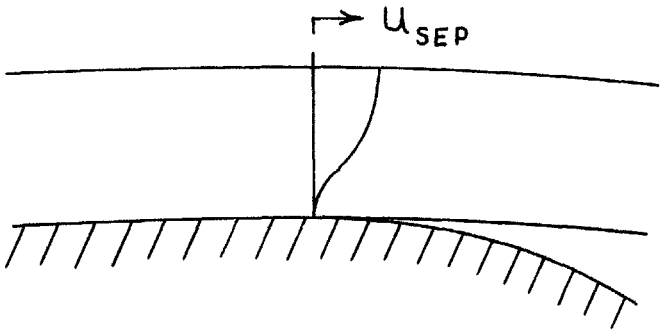

$$\frac{d\Gamma}{dt} = \int_0^{\delta} (u - u_{SEP}) \zeta \, dy$$

$$\text{BUT} \quad \zeta \doteq \frac{\partial u}{\partial y}$$

$$u(0) = 0$$

$$u(\delta) = u_e$$

$$\therefore \quad \frac{d\Gamma}{dt} = \frac{1}{2} u_e^2 - u_{SEP} u_e$$

Figure 7.10 Calculation of Boundary Layer Vorticity Flux in Unsteady Flow

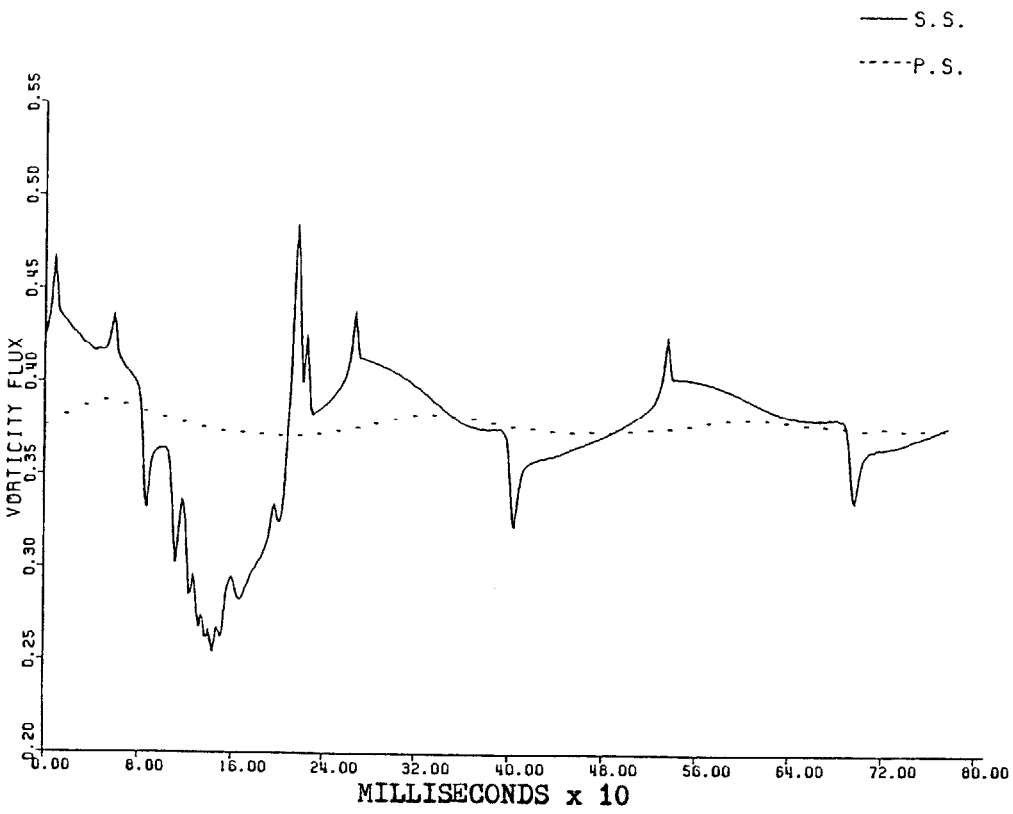

Figure 7.11 Vorticity Flux From Suction and Pressure Surfaces

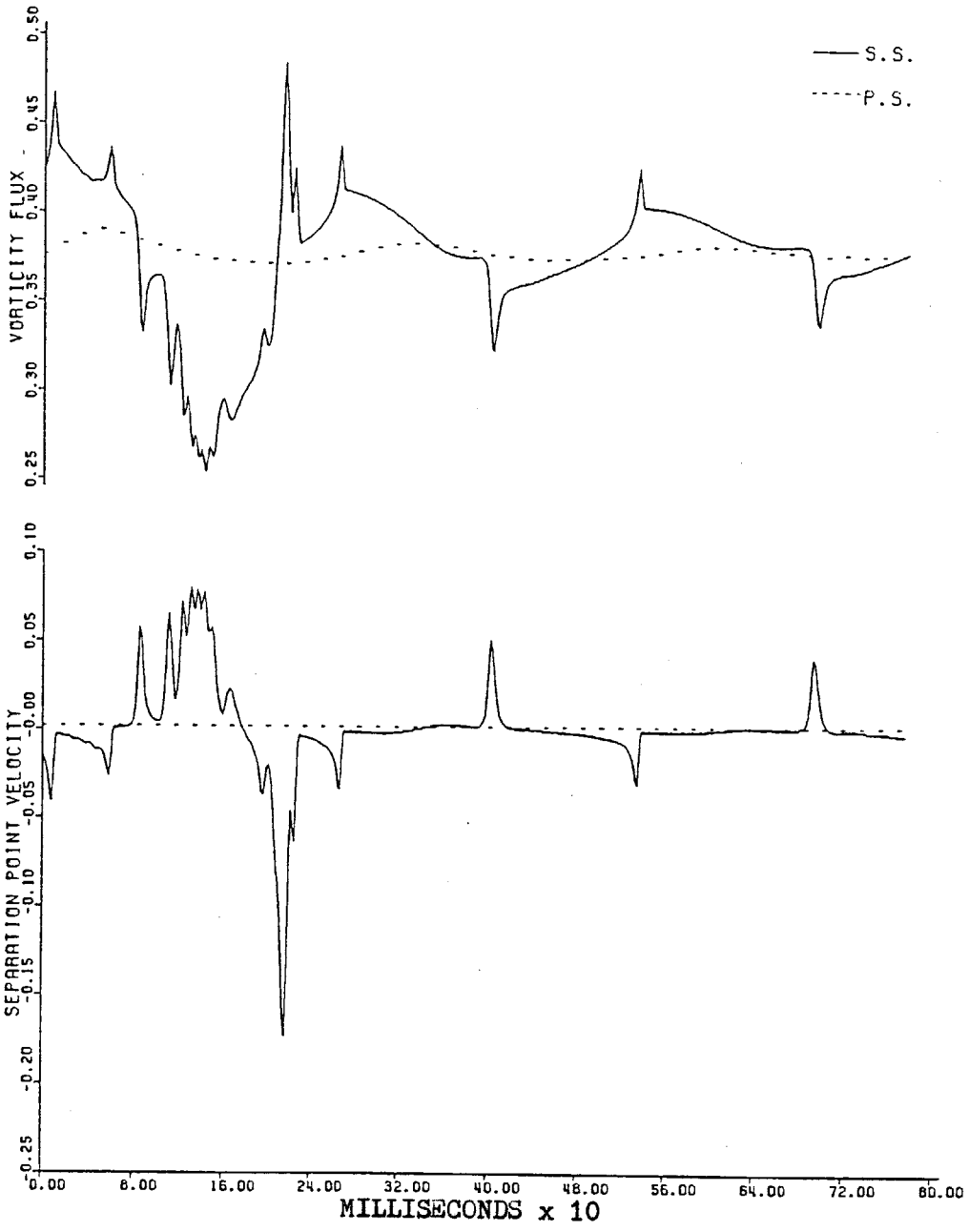

Figure 7.12 Separation Point Velocity and Suction Surface Vorticity Flux

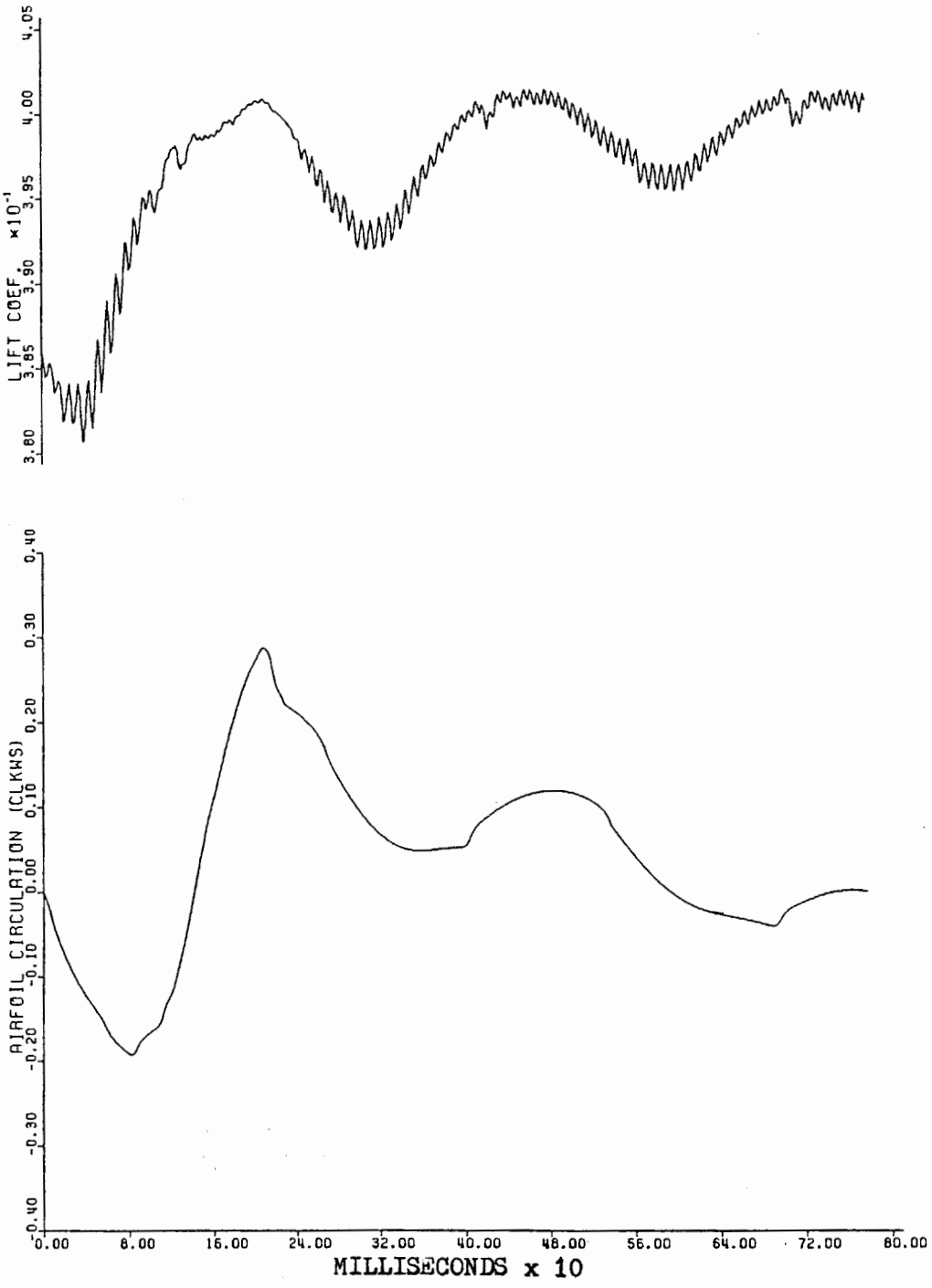

Figure 7.13 Airfoil Circulation and Lift